Theoretical Studies of Ultrafast Correlated Electron Dynamics in Single and Double Photoionization

by

Hongcheng Ni

B.S., Nanjing University, 2008

M.S., University of Colorado Boulder, 2013

A thesis submitted to the

Faculty of the Graduate School of the

University of Colorado in partial fulfillment

of the requirements for the degree of

Doctor of Philosophy

Department of Physics

2014

This thesis entitled:
Theoretical Studies of Ultrafast Correlated Electron Dynamics in Single and Double Photoionization
written by Hongcheng Ni
has been approved for the Department of Physics

_____

Prof. Andreas Becker

_____

Prof. Margaret Murnane

Date _____

The final copy of this thesis has been examined by the signatories, and we find that both the content and the form meet acceptable presentation standards of scholarly work in the above mentioned discipline.

Ni, Hongcheng (Ph.D., Physics)

Theoretical Studies of Ultrafast Correlated Electron Dynamics in Single and Double Photoionization

Thesis directed by Prof. Andreas Becker

Recent advances in laser technology have led to the generation of attosecond laser pulses, whose duration is in the range of the natural time scale of electron dynamics, and thus make the observation and even control of electron dynamics in atoms and molecules possible. While the single-electron dynamics is more thoroughly studied, the correlated dynamics of two electrons is less understood, especially in the context of resolving the ultrafast temporal information in double photoionization.

In this thesis, we first study the energy exchange via electron correlation upon photon absorption over large distances in the two-site double photoionization of the helium dimer, which is found to be a two-step process. In the first step, one electron in one atom absorbs the photon and gets ionized. In the second step, this electron propagates towards the neighboring atom and knocks out the other electron. We then introduce the Hamiltonian reduction method to further study the effects of different interactions in the single and double photoionization of the helium dimer.

Next, we analyze the selection rules for the emission of two electrons from the helium atom, the helium dimer, and general molecules following the absorption of a few photons in an intense laser field. In particular, the back-to-back emission of the two electrons with equal energy sharing is either suppressed or not depending on the number of photons absorbed from the field.

Finally, we study the time delay between the single and double photoionization processes. We first propose a self-consistent-time method to account for the Coulomb-laser coupling effect and obtain the intrinsic photoabsorption time delay measured by the attosecond streak camera. We then proceed to time resolve the correlated emission of two electrons in the knockout process of the helium dimer with respect to the first step of single ionization.

Dedication

To my love.

Acknowledgements

Working at JILA and the University of Colorado Boulder has been a great pleasure, especially because of the knowledgeable and friendly people here, without whom my journey through the graduate school would not have been possible. Here, I would like to thank every one who has lent me kind help, support, and encouragement.

First of all, I am in heavy debt to my advisor, Prof. Andreas Becker. Doing research is like sailing on the vast ocean, which would not be possible if there is not a beacon. Andreas is just like such a beacon for me. He has been a borderless source of creative ideas and physical intuitions that has always been inspiring me. I remember all the times when I come up with some messy (to me) figures, from which Andreas is able to disentangle the disordered parts and discern the relevant physics. Watching him drawing figures and doing all the analyses in front of me have be a gracious treat, from which I learn a lot. What also impresses me a lot is his logic flow in presentations and I can never learn enough from him on these skills. That said, Andreas is a very nice and easygoing person in life on the other hand. I would especially thank his warm support for me when I was trying to look for a postdoctoral position. He had been kindly helping me contacting people he know and giving me suggestions.

Next, I would like to gratefully thank Dr. Agnieszka Jaroń-Becker, my coadvisor. Agnieszka has a very broad knowledge in both physics and chemistry, from whom I have gained a lot. Whenever we encounter some unfamiliar phenomena, she would always been able to connect that to a physical process. Her insights have been helping me to digest and build a more comprehensive view of the physical world. Besides that, she is extremely warm-hearted and is ready to help at any

time. When I was looking for the postdoctoral position, she had been looking for every possibility for me and have talked to me about the research and life in different places for hours and hours. I could never thank her enough.

I would also give my gratitude to my previous colleagues, Dr. Shaohao Chen, Dr. Antonio Picón, and Dr. Norio Takemoto, with whom I had enjoyed great benefit when I started my research in the group. It would not have been possible for me to dig into all the computer codes, numerical methods, and physical concepts without their help. I would especially thank Shaohao, who had been disturbed by me for afternoons and afternoons. He had been always patient and led me through the problems step by step. Antonio had be particularly helpful in sharing cutting papers and explaining new physical concepts to me. He had also been constantly helping me when I was looking for the postdoctoral position. In addition, I would gratefully thank all my current colleagues, Jing Su, Dr. Carlos Hernández-García, Yuqing Xia, Daniel Weflen, Andrew Spott, Michelle Miller, and Cory Goldsmith, for creating such an active and pleasant atmosphere. Working in the Becker group has helped me shaping my early career that would lighten my future and benefit me for life.

I would further express my appreciation to my collaborators, Dr. Shaohao Chen, Dr. Camilo Ruiz, and Prof. Reinhard Dörner, without whom most of my work would not have been possible. It has also been a delight to work with them. I would especially thank Prof. Dörner, who lent me warm help in writing a very positive recommendation letter, without which it would not have been possible for me to get a postdoctoral position.

Moreover, I would like to thank Prof. Margaret Murnane, Prof. Steven Cundiff, Prof. John Bohn, and Prof. David Jonas for agreeing to be in my dissertation committee. Their insightful feedback has helped me to shape my work and thesis better. I would especially thank Prof. Murnane and Prof. Bohn to proof read my thesis.

The JILA computing center and the Janus supercomputing center have also been continuously supporting me. It would not have been possible to carry out numerical experiments without their support.

Finally and most importantly, I would like to thank my family and all friends that have been

continuously supporting me and encouraging me for years. I have been always on the go and away from home, chasing my dream since high school, which makes me feel guilty. However, the support, encouragement, and love I get from my family have never ceased or receded. The life in a foreign country has also been difficult. Fortunately, I met a lot of friends here that make me feel unlonely. Especially luckily, I met my lovely wife, Jin Wen, here. She has been the sunshine in my life and has been backing me up with her endless love to help me go through the rough and bumpy roads and fight against all the frustrations.

Thank you all, sincerely.

Contents

Chapter

Tables

Table

Figures

Figure

Chapter 1

Introduction

The last 30 years have been a prosperous period of time in ultrafast science thanks to the availability of femtosecond (1 fs = 10^{-15} s) laser technology, most notably the Ti:sapphire lasers [1], which are capable of producing intense femtosecond laser pulses tunable in the red to near-infrared (NIR) range with intensities exceeding 10^{15} W/cm^2 in the focal spot. The real-time observation and control of atom motions, as well as energy exchange between atoms in molecules and condensed matter systems have been achieved (refer to Ref. [2] for a review of femtochemistry). Recent advances in laser technology have led to the generation of attosecond (1 as = 10^{-18} s) extreme ultraviolet (XUV) laser pulses. The duration of these pulses is in the range of the natural time scale of electron dynamics, and thus make the observation and even control of electron dynamics in atoms and molecules possible (refer to Ref. [3] for a recent review of attosecond physics). In this chapter, we give a brief introduction to the background and some basic concepts of attosecond and strong-field physics and outline the overall structure of this thesis.

1.1 Strong-field single ionization and the Keldysh parameter

The strong-field single ionization of atoms and molecules can generally be divided into three categories, i.e., multiphoton ionization, tunneling ionization, and above-barrier ionization, with the help of the Keldysh parameter γ [4]. The strong-field ionization consists of a subtle relation between photon energy and photon number (or field intensity). For a high photon energy and relatively low field intensity, the ionization proceeds in a way that the electron absorbs one or a few

energetic photons and the interaction with the laser field can be considered as perturbative. For a low photon energy and high field intensity, in contrast, the ionization occurs in a manner that the electron absorbs many photons and the interaction is nonperturbative. In the limiting case of a large number of absorbed photons, the latter process can be considered as tunneling ionization, which is illustrated in Fig. 1.1. The strong laser field suppresses the Coulomb field of the nucleus at one side and results in a barrier, through which the bound electron may tunnel out, leading to ionization.

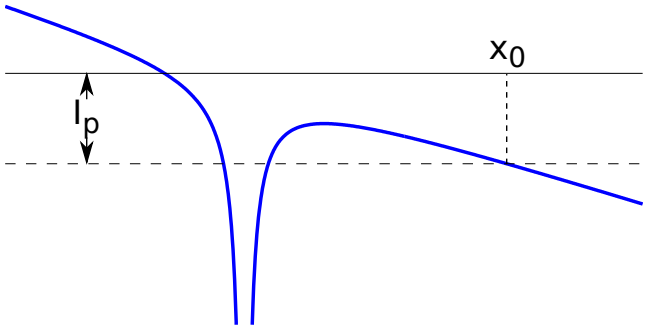

Figure 1.1. Illustration of the Keldysh theory [4].

To clearly understand the relation between the multiphoton and tunneling ionization, we examine the time scale of the quasi-static tunneling ionization [4]. As shown in Fig. 1.1, the strong laser field produces a tunneling exit x_0 for the electron with bound energy I_p, thus (Hartree atomic units, $e = m = \hbar = 1$, are used throughout the thesis, unless stated otherwise)

$$-I_\mathrm{p} = -\frac{Z}{x_0} - Ex_0 \approx -Ex_0, \tag{1.1}$$

where Z is the nucleus charge and E is the field amplitude. Thus

$$x_0 \approx \frac{I_\mathrm{p}}{E}. \tag{1.2}$$

The velocity of the electron before tunneling can be estimated by

$$v_\mathrm{e} = \sqrt{2E_\mathrm{e}} = \sqrt{2I_\mathrm{p}}, \tag{1.3}$$

where the kinetic energy of the electron $E_\mathrm{e} = I_\mathrm{p}$ is a result of the virial theorem. Therefore, the

tunneling time can be estimated as

$$\tau = \frac{x_0}{v_e} \approx \frac{I_p}{E}\sqrt{\frac{1}{2I_p}} = \frac{1}{2\omega}\sqrt{\frac{I_p}{2U_p}}, \tag{1.4}$$

where

$$U_p = \left(\frac{E}{2\omega}\right)^2 \tag{1.5}$$

is the ponderomotive energy of the electron (cycle-averaged quiver energy of the electron in a laser field) and ω is the angular frequency of the laser field. On the other hand, one half period of the oscillating field is $\frac{T}{2} \approx \frac{1}{2\omega}$. If $\tau > \frac{T}{2}$, or $\sqrt{\frac{I_p}{2U_p}} > 1$, the field oscillation has already reversed its direction before the electron can tunnel; while if $\tau < \frac{T}{2}$, or $\sqrt{\frac{I_p}{2U_p}} < 1$, the electron may tunnel out through the barrier. Thus, we can define the Keldysh parameter [4]

$$\gamma = \sqrt{\frac{I_p}{2U_p}} \tag{1.6}$$

as a criteria to categorize the strong-field ionization into multiphoton ionization when $\gamma \gg 1$ and tunneling ionization when $\gamma \ll 1$. In cases when $\gamma \approx 1$, the two mechanisms coexist. The above-barrier ionization, on the other hand, is just an extreme case of the tunneling ionization, where the laser field is so strong and suppresses the Coulomb potential so much that the energy level of the initially bound electron is already above the tunneling barrier.

1.2 Strong-field double ionization

Single ionization in strong fields, as discussed above, can be categorized into multiphoton ionization ($\gamma \gg 1$) and tunneling ionization ($\gamma \ll 1$). In this section, we introduce the different mechanisms in strong-field double ionization, which can generally be divided into three categories [5, 6], i.e., sequential double ionization (SDI), nonsequential double ionization (NSDI), and recollision excitation with subsequent field ionization (RESI). These mechanisms distinguish themselves, in particular, in the role of the electron correlation.

In SDI, as the name implies, the two electrons are emitted one after the other via interaction with the field, without much influence on the emission of each other. Thus, it can be simply

regarded as two sequential single ionization processes. SDI can occur in both multiphoton and tunneling regimes.

NSDI, on the other hand, is more complex, since the emission of the two electrons is correlated. In the multiphoton regime, the photon energy can be regarded as being deposited to one of the electrons initially, which interacts and exchanges energy with the other electron via their Coulomb correlation and both electrons are emitted in the end. Two different mechanisms are possible here, i.e., knockout [7, 8] and shakeoff [9]. The knockout mechanism applies to the case when the photon has a relatively low energy and the first electron (primary electron) has a low kinetic energy after ionization. On its path of emission from the system, however, this electron may knock out the other electron from the system through their mutual interaction. The shakeoff mechanism, on the other hand, applies to the cases when the photon has a high energy and the first electron is striped from the system rapidly before the rest of the system, including the other electron, can adjust to this change. Now this system needs to relax to the eigenstates of the new Hamiltonian with one electron removed. Projecting the wave function onto the eigenstates of the new system, with some probability the electron will be found in the continuum, leading to double ionization. The electron correlation in the shakeoff process is reflected in the initial two-electron state, which prepares the system in a highly correlated fashion. It is also the correlation in the initial state that keeps the energy conserved for the emission of the second electron. The separation of these two mechanisms for double photoionization of the helium atom is around an excess electron kinetic energy of 350 eV [10].

NSDI in the tunneling regime is equally interesting. After the first electron tunnels out and gets accelerated first away from the parent ion, it may be driven back by the same laser field when the field reverses its direction. During the so-called rescattering [11, 12], the electron may collide with the parent ion and knock another electron out, resulting in double ionization.

RESI, at last, is similar to NSDI in the tunneling regime, but when the rescattered electron collides with the parent ion, it does not knock another electron out, but promotes it to an excited state, from which it can easily tunnel out in the laser field. RESI is considered as belonging to the

third category since the electron correlation is necessary for the excitation of the second electron, while the subsequent ionization of the second electron may not directly relate to the first electron.

We can summarize all these mechanisms as a diagram below, using the double ionization of the helium atom as an example:

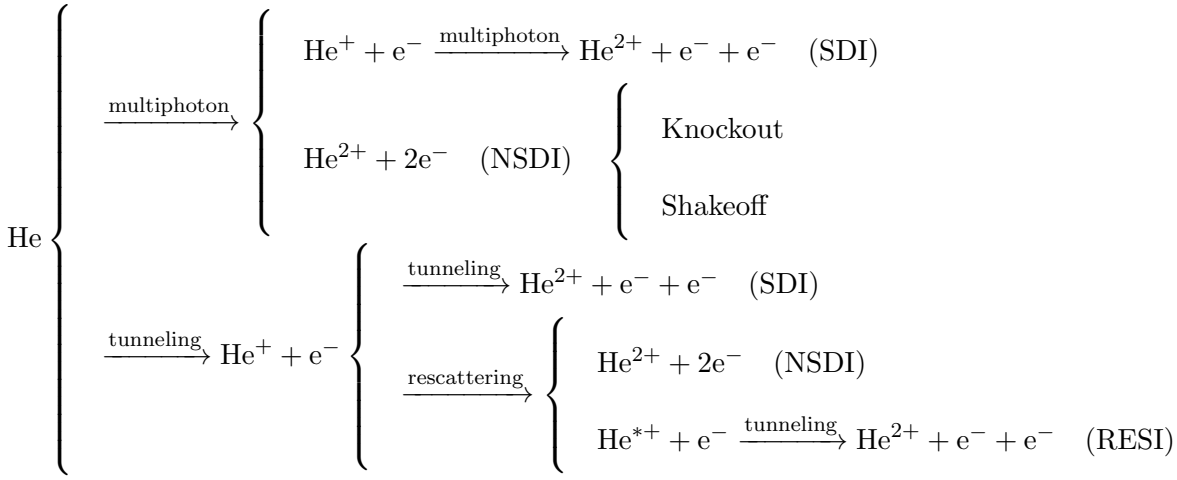

1.3 High-order harmonic generation

In NSDI in the tunneling regime, the rescattered electron collides with the parent ion and knocks out another electron. However, instead of knocking out a second electron, the returning electron may instead recombine to the ground state and emit a photon. This process is called the high-order harmonic generation (HHG) [13–15] since one single energetic photon is emitted in this recombination process after the electron absorbs many photons and gains a lot of energy from the oscillating laser field.

The HHG process can be described by a three-step model (see Fig. 1.2) [12]: 1. Tunneling: tunneling ionization of electron through the potential barrier suppressed by the intense laser field. 2. Acceleration: electron driven away from and then back to the ion core by the oscillating laser field. 3. Recombination: returning electron collides with the ion core with some energy and emits a photon. Or, in the language of wave mechanics, the returning wave packet, together with the parent wave packet, form a rapidly changing dipole moment, and thus emit light radiation.

The tunneling probability of an electron through the suppressed potential barrier is exponen-

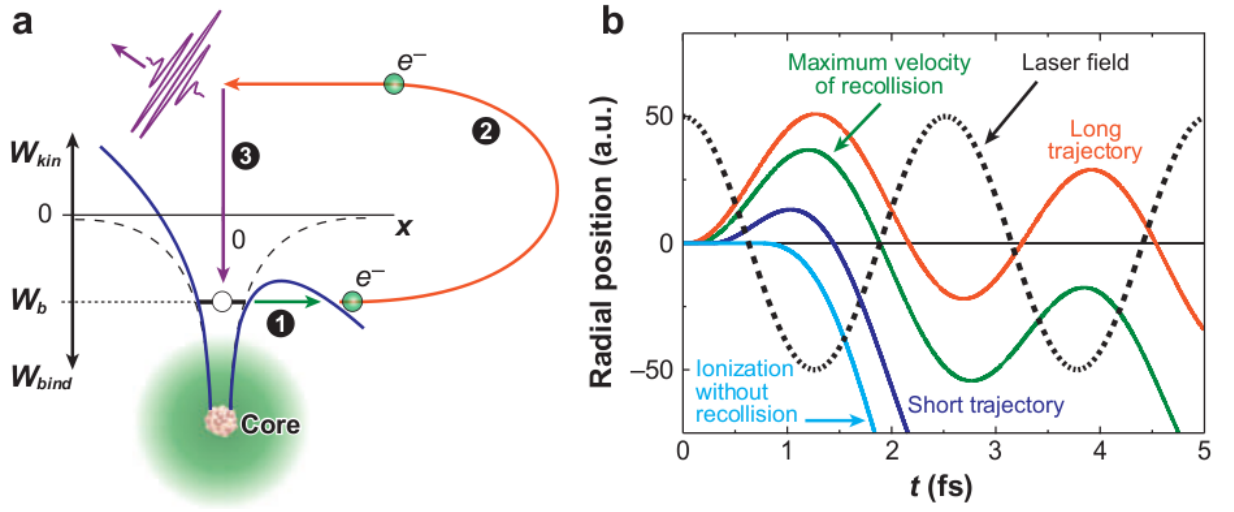

Figure 1.2. The three step model of the HHG process and electron trajectories (image credit Ref. [16]).

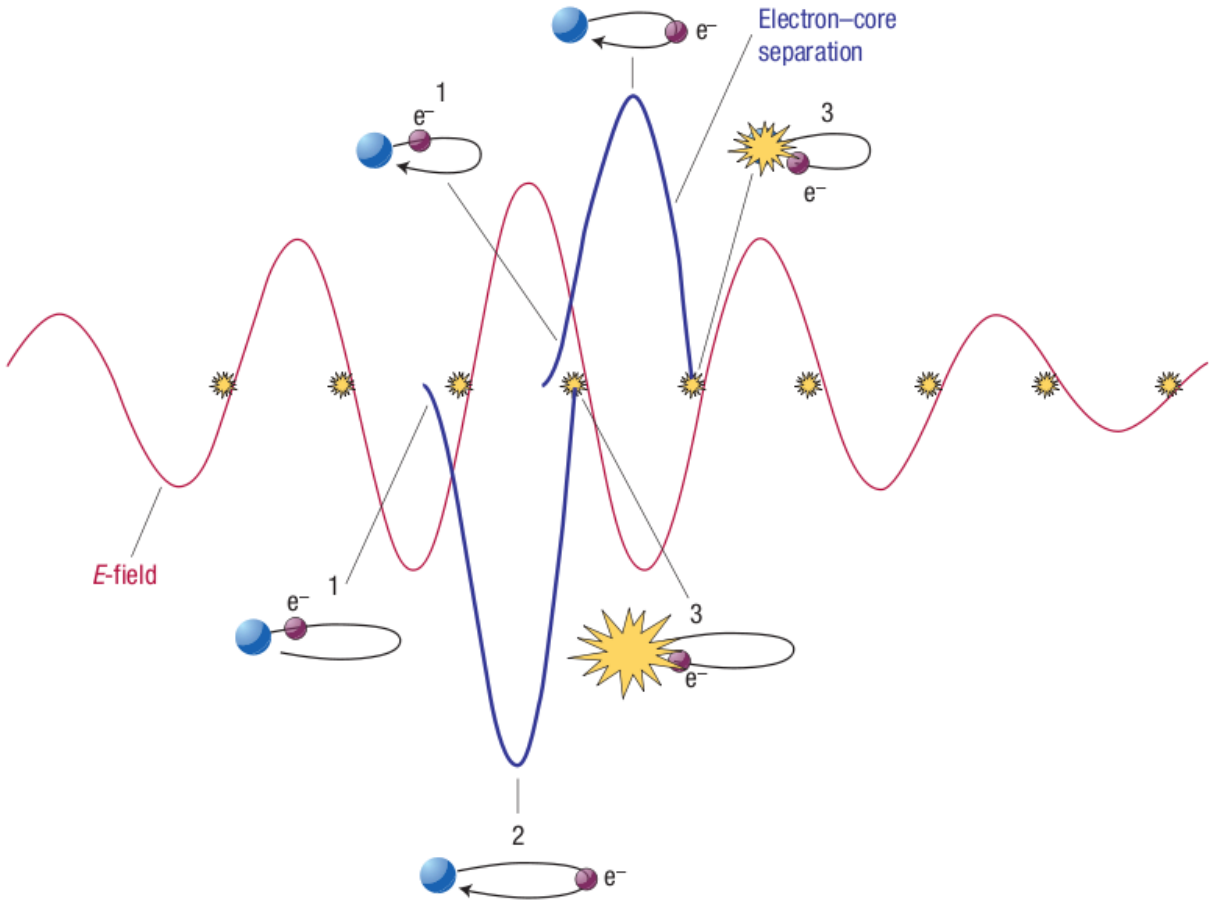

Figure 1.3. Generation of an attosecond pulse train (image credit Ref. [17]).

tially proportional to the laser field magnitude. However, if an electron is released at exactly a local maximum of the laser field, it returns to the ion core with zero energy, a temporally uniform field granted. If it is released before the maxima, it will drift away, not being able to return at all. When an electron is however released after the maxima, it will then return with some energy, collide with the ion core, and free the energy in the form of a photon. If it is released at approximately 18° after the field extrema, the return energy reaches its maximum, at $3.17U_{\mathrm{p}}$. Therefore, the cut-off energy of the photon emitted is $E_{\mathrm{max}} = I_{\mathrm{p}} + 3.17U_{\mathrm{p}}$ [12, 18].

For each photon energy lower than the cut-off energy, there must be two contributions to the HHG spectrum, one for the electron release before 18° which results in the so-called long trajectory, and another for the electron release after 18° which leads to the shorter trajectory, as illustrated in Fig. 1.2. Since the photon energy spans broadly, from 0 to the cut-off energy, the pulses generated by the superposition of a broad range of harmonics are very short, indeed of attosecond duration.

However, the three-step process can occur every half-cycle of the laser field, since the field reaches a maximum every half-cycle (see Fig. 1.3). Therefore, for each half-cycle of the laser field, there will be an attosecond pulse generated. That is why in a long driving pulse an attosecond pulse train is generated much more easily than an isolated attosecond pulse. This half-cycle periodicity also ensures that there is only odd-order harmonics in the HHG spectrum (if it is generated from rare-gas atoms). Moreover, since the driving laser field changes in magnitude over time, the cut-off energy for each half-cycle also changes, i.e., there are different cut-off energies for each half-cycle of the laser field.

1.4 Generation of single isolated attosecond pulse

The attosecond pulse train, while suitable for a number of experiments, is not ideal for time-resolved experiments since there is an ambiguity in time due to the interaction with multiple pulses in the pulse train.

Proposed by Christov, Murnane, and Kapteyn in 1997 [19, 20] and experimentally implemented by Krausz and coworkers in 2001 [21–24], the cut-off harmonics method is a straightforward

way to retrieve a single isolated attosecond pulse. Although there are different cut-off energies for each half-cycle of the laser field, the overall cut-off energy occurs only near the envelope peak of the laser pulse, as is also shown in Fig. 1.3.

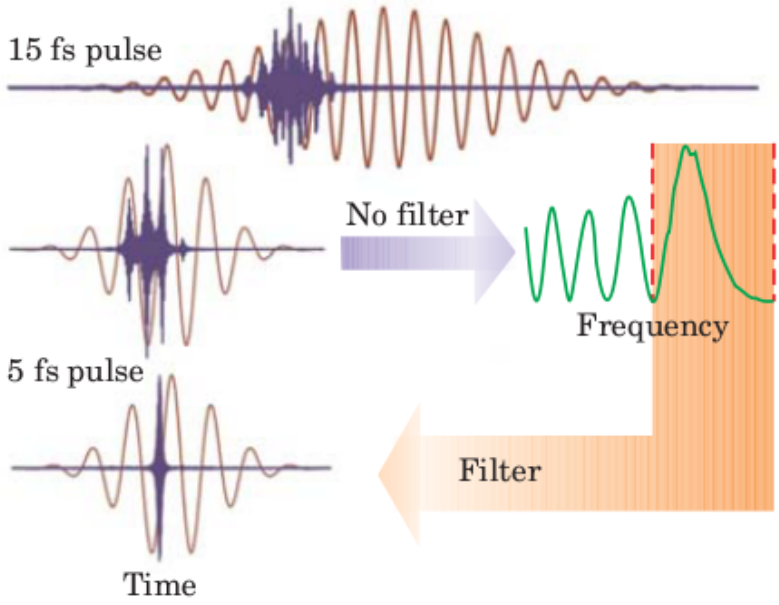

Figure 1.4. The cut-off harmonics method to retrieve a single isolated attosecond pulse (image credit Ref. [25]).

As illustrated in Fig. 1.4, the idea is to reduce the femtosecond driving laser pulse width to only about 5 cycles which results in the generation of only 3 attosecond bursts at significant energy. There is however only one burst, which contributes to the overall cut-off energy. Using a high pass filter (a thin metal film) to filter out the lower harmonics, one is left with the most energetic attosecond burst.

The electric field of a pulse can be expressed as $E(t) = E_0(t)\cos(\omega t + \varphi)$, where $E_0(t)$ is the pulse envelope and φ is the carrier-envelope phase (CEP). To generate stable single attosecond pulses, it is necessary that the waveform of the driving laser field is stable from pulse to pulse, i.e., the CEP should be stable.

In fact, this method not only requires a stable CEP, but works optimally only for $\varphi = 0$ and fails for $\varphi = \pm\pi/2$. As shown in Fig. 1.5, two attosecond pulses almost identical in energy

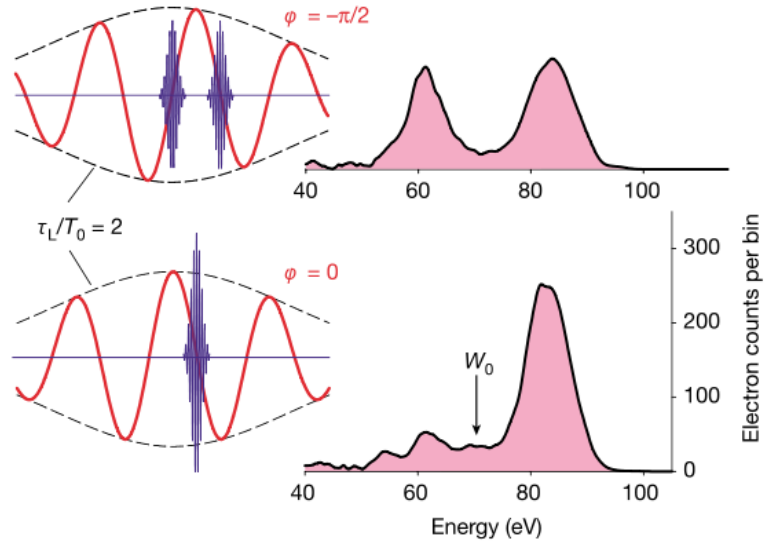

Figure 1.5. The cut-off harmonics method fails for CEP=$\pm\pi/2$ (image credit Ref. [24]).

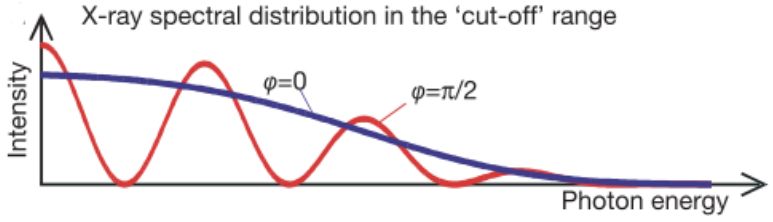

Figure 1.6. Fourier transform of cut-off pulses above cut-off energy (image credit Ref. [23]).

are generated at $\varphi = -\pi/2$, while only one is generated at $\varphi = 0$. Filtering out components with energy lower than the overall cut-off energy still retains two pulses at $\varphi = \pm\pi/2$. This can also be seen from the Fourier transform of the cut-off pulses in these two cases, as shown in Fig. 1.6. No matter how the high pass filter is set, the spectrum left is still oscillating, which is still two attosecond pulses when transformed back.

As outlined, the technique requires the generation of few-cycle laser pulses, which is technologically still challenging. Another disadvantage of this method is that it has a low efficiency. The energy remained after the filter is applied is only about 10^{-5} of the original energy [26].

Over the years, a number of methods have been proposed and implemented to generate single isolated attosecond pulses, including the polarization gating method [27–31], the two-color laser method [27, 32], the surface harmonic generation method [33–35], the spatial filtering method [36, 37], and the phase-matching gating method [38–40].

1.5 Attosecond streak camera

With the attosecond XUV laser pulse available, the first question to ask is how to make use of it to resolve attosecond electron dynamics. In the traditional femtosecond spectroscopy, the pump-probe scheme is usually applied, where the pump femtosecond laser pulse initiates the ultrafast dynamics and the probe femtosecond laser pulse measures the change in a physical variable induced by the pump pulse. By varying the relative delay between the pump and probe pulses in a controlled manner, the ultrafast femtosecond dynamics of processes in atoms, molecules, or solid-state systems can be observed or even manipulated. Although attosecond XUV laser pulses are currently available, the pump-probe experiments with these pulses are still difficult up to now due to the low interaction cross section of matter with XUV laser pulses and the low repetition rate of the attosecond XUV laser pulse at nanojoule pulse energies [41]. However, alternative techniques like the attosecond streak camera [42] and the attoclock [43] have been used in observing and controlling electronic motion with a temporal resolution of less than 100 as, e.g., the real-time observation of tunneling ionization in atoms [43, 44], photoelectron emission from solids [45], and

the tracing of electron dynamics in atoms and molecules [46, 47].

To understand how the attosecond streak camera technique works, we first introduce the conventional streak camera [49, 50], as shown in Fig. 1.7(a). The conventional streak camera is traditionally used to characterize the temporal profile of a short light pulse. Its basic principle is first to convert the light signal into an electron signal, which temporal profile is mapped onto a measurable spatial profile as follows. As shown in the figure, a metal (gray plate) is illuminated by the short light pulse (cyan curve) with an unknown temporal profile, and electrons (purple dots) get emitted from the metal surface due to the photoelectric effect. The stronger the light pulse is at a certain moment the more electrons will be emitted. As a result, the light signal is converted into an electron signal. Next, the electron signal passes through an external electric field linearly varying in time, which deflects earlier arriving electrons differently from later arriving electrons. In this way, the temporal profile of the electron signal is converted into the spatial profile when it is collected on the fluorescent screen, leading to the characterization of the temporal profile of the incident light pulse. The conventional streak camera can reach a temporal resolution of a few hundred femtoseconds. For even faster phenomena, like electronic dynamics in atoms and molecules, the conventional streak camera falls short, since increasing the gradient of the linear varying laser field to improve the temporal resolution becomes increasingly difficult.

The attosecond streak camera [42], as shown in Fig. 1.7(b), shares similar ideas. Its basic principle is first to convert the light signal into an electron signal, which is then converted into the measurable momentum profile instead of a spatial profile. As shown in the figure, a gas jet (not shown) of atoms (yellow dots) is illuminated by the ultrashort XUV light pulse (cyan curve), which ionizes the atoms and produces free electrons. In this way, the temporal profile of the ultrashort light pulse is converted into an electron signal. In contrast to the conventional streak camera in which a linear varying electric field is applied, here an additional few-cycle NIR streaking laser pulse (red curve), synchronized with the ionizing XUV laser pulse, is applied, which modulates the asymptotic momentum of the ionized electrons according to its instant of transition into continuum. By measuring the final momentum profile of the electrons collected at the detector, the electron

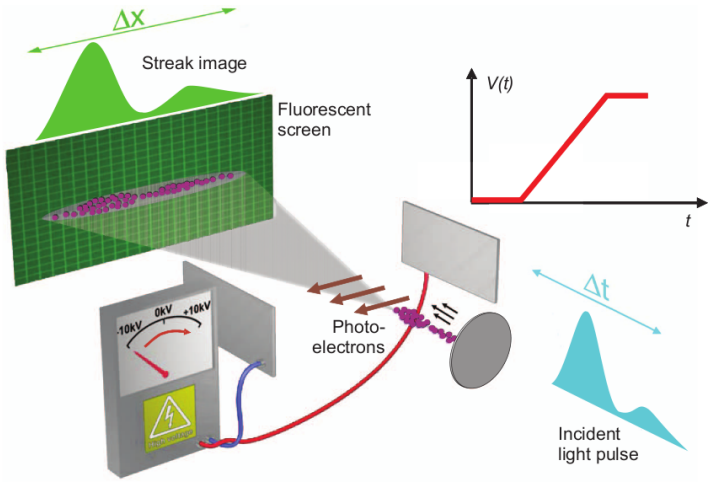

(a) Scheme of the conventional streak camera

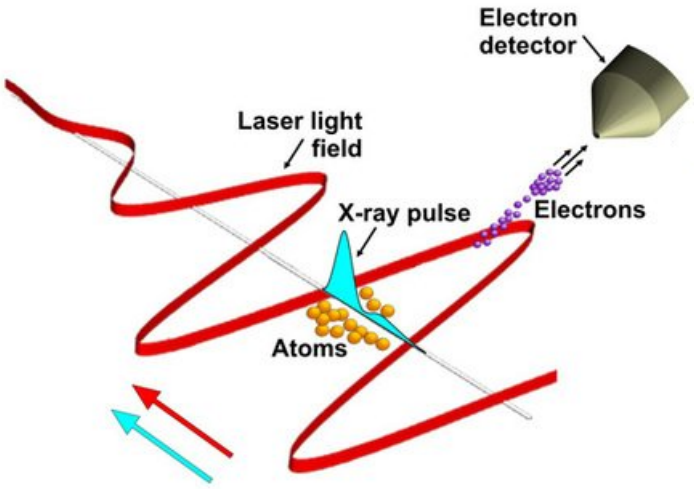

(b) Scheme of the attosecond streak camera

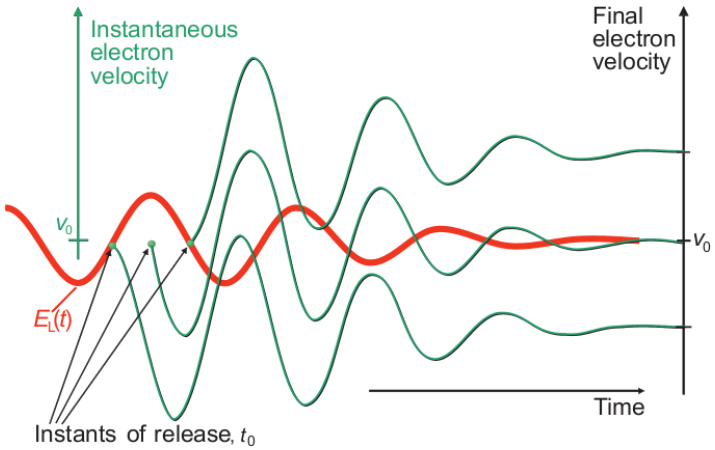

(c) Principle of the attosecond streak camera

Figure 1.7. (a) Scheme of the conventional streak camera (image credit Ref. [3]), (b) scheme of the attosecond streak camera (image credit Ref. [48]), and (c) principle of the attosecond streak camera (image credit Ref. [3]).

signal, and in turn the temporal profile of the ultrashort XUV light pulse, can be characterized. In this case, however, the "deflection" occurs within half a period of the streaking pulse, which provides the possibility for measurements in the attosecond regime.

Although the attosecond streak camera was originally introduced for the characterization of ultrashort light pulses, it can also be used to time resolve ultrafast electron dynamics. As shown in Fig. 1.7(c), electrons released at different instants t_0 drift differently in the streaking laser field and have a different shift in the final momentum according to their instant of release t_0

$$\boldsymbol{p}_{\mathrm{f}} \approx \boldsymbol{p}_0 - \boldsymbol{A}(t_0)/c, \tag{1.7}$$

where $\boldsymbol{p}_0$ is the asymptotic momentum of the electron in the absence of the streaking field, $\boldsymbol{A}(t_0)$ is the vector potential of the streaking field at the instant of release t_0 of the electron, and c is the vacuum speed of light. By scanning the relative delay τ between the ionizing XUV laser pulse and the streaking NIR laser pulse, a streaking trace can be obtained which consists of the momentum distributions of the electron as a function of the time delay τ. Fitting the streaking trace to the vector potential of the streaking field, we can obtain the time information regarding the electron release. Eqn. (1.7) is accurate as long as the dipole approximation is valid and there is no other potential present. However, in the ionization of an atom, the Coulomb potential of the residual ion is present, and the electron motion in the coupled fields of the Coulomb potential and the streaking laser field induces an error to Eqn. (1.7). In Sec. 5.2, we will study this Coulomb-laser coupling effect and account for the additional time delay induced to obtain the intrinsic time delay in the photoionization process of atoms and molecules.

1.6 Outline of this thesis

Recent advances in a variety of light sources such as the ultrashort intense lasers [3, 15], synchrotron radiations [51], and free-electron lasers [52–54], novel measurement techniques like the cold-target recoil-ion momentum spectroscopy [55, 56], and theoretical approaches [57, 58] have led to a profound understanding of the correlated emission of two electrons in light-induced double

ionization of atoms and molecules [51, 59–73]. The role of electron correlation in double ionization, as compared to the single-electron emission where only electron-nucleus interaction plays a role, is however still less understood, especially regarding the recently observed energy exchange between electrons over distances of several Angstroms [74]. This thesis is thus devoted to the theoretical studies and numerical simulations of ultrafast correlated electron dynamics in single and double photoionization of atoms and molecules, in an effort to better understand the highly correlated few-body dynamics.

In Chapter 2, we introduce the numerical methods used in this thesis for an *ab-initio* solution of the time-dependent Schrödinger equation (TDSE) in the grid representation with the finite-difference method. The numerical methods to obtain the ground state of a system and to propagate the initial state in a time-dependent potential, the absorbing boundaries, and the space-partitioning method to obtain single and double ionization contributions are presented. Parallel computation, which uses multiple concurrent threads for a speedup of the calculations, is also briefly discussed.

In Chapter 3, we first study the energy exchange via electron correlation upon photon absorption over large distances in the two-site double photoionization of the helium dimer, which is found to be a two-step process in our time-dependent numerical simulations. The double ionization probability is shown to be closely related to that of the photoemission of an electron from one of the helium atoms along the internuclear axis. Together with an analysis of the temporal evolution of the two-electron probability distribution, this provides direct evidence for the two-step knockout mechanism by which the photon energy is shared between the electrons over distances of several Angstroms in the dimer. In the first step, as shown, one electron (the primary electron) in one of the atoms absorbs the photon and gets ionized. In the second step, this electron propagates towards the neighboring atom and knocks out the other electron (the secondary electron). We then introduce the Hamiltonian reduction method, which selectively removes certain interactions from the full Hamiltonian, in order to further study the effects of different interactions in the single and double photoionization of the helium dimer.

In Chapter 4, we first analyze the selection rules for the emission of two electrons from the

helium atom following the absorption of a few photons in an intense laser field. The rules arise due to the symmetries of the accessible final states in the two-electron continuum. In particular, the back-to-back emission of the two electrons with equal energy sharing is either suppressed or not depending on the number of photons absorbed from the field. We then further generalize the selection rules to the helium dimer and general molecules and conclude that the rules apply as long as the system, excluding the two active electrons, has the central symmetry respect to its center of mass.

In Chapter 5, we study the time delay between the single and double photoionization processes, namely the correlation time delay. To this end, we first propose a self-consistent-time method to account for the Coulomb-laser coupling effect and obtain the intrinsic photoabsorption time delay measured by the attosecond streak camera. We then proceed to time resolve the correlated emission of two electrons in the knockout process of the helium dimer with respect to the first step of single ionization using the variable space-partitioning method as well as the attosecond streaking technique, which is extended to many-electron systems. The streaked variable for the single ionization is the momentum of the first electron, while the streaked variable for the double ionization is the center-of-mass momentum of both electrons. The correlation time delays obtained for different laser parameters are compared with classical estimates.

At last, a summary is given in Chapter 6.

Chapter 2

Numerical methods

Central to the analysis of time resolving the laser-matter interaction is solving the TDSE of the system. For complex systems containing many charged particles, solving TDSE directly can be extremely difficult. In this case, one can use standard chemical methods such as the time-dependent Hartree–Fock method and the time-dependent density-functional theory. For simpler systems where one or two electrons are involved in the interaction, we can solve the associated TDSE using *ab-initio* methods, which are more accurate than the chemical methods and are capable of resolving more details of the physics of a certain phenomenon.

In this chapter, we discuss the numerical methods to solve the TDSE in grid representations, i.e., using the finite-difference method. The basic parameters to characterize a specific simulation are the spatial step Δx (and Δy, Δz, etc.), number of grid points N_x (and N_y, N_z, etc.), and the time step Δt.

2.1 The split-operator method

In this section, we describe the split-operator method, which reduces the time propagation of the multidimensional electron wave function to different directions. To make the scheme transparent, we illustrate the method with a system containing only one electron, the TDSE of which reads

$$i\frac{\partial}{\partial t}\psi(\boldsymbol{r},t) = H(\boldsymbol{r},t)\psi(\boldsymbol{r},t), \tag{2.1}$$

where the Hamiltonian of the system is

$$H(\boldsymbol{r},t) = \frac{[\boldsymbol{p} - \boldsymbol{A}(t)]^2}{2} + V(\boldsymbol{r}), \tag{2.2}$$

in which $\boldsymbol{A}(t)$ is the vector potential of the laser pulse and $V(\boldsymbol{r})$ is the Coulomb potential of the residual ion. For small time steps Δt, the evolution of the wave function can be approximated as

$$\psi(\boldsymbol{r}, t + \Delta t) \approx e^{-iH(\boldsymbol{r},t)\Delta t}\psi(\boldsymbol{r}, t). \tag{2.3}$$

In Cartesian coordinates, the Hamiltonian, by convenience, can be decomposed to different directions as

$$H(\boldsymbol{r},t) = H_x(\boldsymbol{r},t) + H_y(\boldsymbol{r},t) + H_z(\boldsymbol{r},t), \tag{2.4}$$

in which

$$H_x(\boldsymbol{r},t) = \frac{[p_x - A_x(t)]^2}{2} + \frac{1}{3}V(\boldsymbol{r}), \tag{2.5}$$

$$H_y(\boldsymbol{r},t) = \frac{[p_y - A_y(t)]^2}{2} + \frac{1}{3}V(\boldsymbol{r}), \tag{2.6}$$

$$H_z(\boldsymbol{r},t) = \frac{[p_z - A_z(t)]^2}{2} + \frac{1}{3}V(\boldsymbol{r}), \tag{2.7}$$

where H_x, H_y, and H_z can be regarded as the Hamiltonian in the x, y, and z directions, respectively.

The time-propagation operator can now be approximated as

$$e^{-iH(\boldsymbol{r},t)\Delta t} \approx e^{-iH_x(\boldsymbol{r},t)\Delta t/2}e^{-iH_y(\boldsymbol{r},t)\Delta t/2}e^{-iH_z(\boldsymbol{r},t)\Delta t}e^{-iH_y(\boldsymbol{r},t)\Delta t/2}e^{-iH_x(\boldsymbol{r},t)\Delta t/2}, \tag{2.8}$$

which is accurate to the second order in time. This follows straightforward from

$$e^{\hat{x}+\hat{y}} = e^{\hat{y}/2}e^{\hat{x}}e^{\hat{y}/2} + O^3, \tag{2.9}$$

which can be proven using the Baker–Campbell–Hausdorff formula

$$\log(e^{\hat{x}}e^{\hat{y}}) = \hat{x} + \hat{y} + \frac{1}{2}[\hat{x},\hat{y}] + \frac{1}{12}[\hat{x},[\hat{x},\hat{y}]] - \frac{1}{12}[\hat{y},[\hat{x},\hat{y}]] + \cdots . \tag{2.10}$$

Using the split-operator method, the propagation in arbitrary dimensions can be reduced to the propagations in one direction at a time, which greatly improves the speed of numerical computations. Thus, for clarity, we restrict our discussions of the numerical methods below to one dimension.

2.2 The Crank–Nicolson method

The Crank–Nicolson method [75] is a unitary, energy conservative, and unconditionally stable method to solve the TDSE with an accuracy of second order in time and space. Here, the time evolution operator can be written in the Cayley form as

$$e^{-iH(t)\Delta t} \approx \frac{1 - iH(t)\frac{\Delta t}{2}}{1 + iH(t)\frac{\Delta t}{2}}, \tag{2.11}$$

which is an unitary transformation accurate to the second order in time. From this it follows

$$\left(1 + i\frac{\Delta t}{2}H\right)\psi(t + \Delta t) = \left(1 - i\frac{\Delta t}{2}H\right)\psi(t). \tag{2.12}$$

With the split-operator method, the Hamiltonian in the x direction has the form

$$H_x = A(x, y)\frac{\partial^2}{\partial x^2} + B(x, y)\frac{\partial}{\partial x} + V(x, y), \tag{2.13}$$

where y stands for all other coordinates.

The Crank–Nicolson method for the coordinate x reads

$$\begin{aligned}
&\psi_n(t + \Delta t) + i\frac{\Delta t}{2}\left[A_n(y)\frac{\psi_{n+1}(t + \Delta t) - 2\psi_n(t + \Delta t) + \psi_{n-1}(t + \Delta t)}{(\Delta x)^2}\right. \\
&\left. + B_n(y)\frac{\psi_{n+1}(t + \Delta t) - \psi_{n-1}(t + \Delta t)}{2\Delta x} + V_n(y)\psi_n(t + \Delta t)\right] \\
=&\psi_n(t) - i\frac{\Delta t}{2}\left[A_n(y)\frac{\psi_{n+1}(t) - 2\psi_n(t) + \psi_{n-1}(t)}{(\Delta x)^2} + B_n(y)\frac{\psi_{n+1}(t) - \psi_{n-1}(t)}{2\Delta x} + V_n(y)\psi_n(t)\right],
\end{aligned} \tag{2.14}$$

where n represents the index of the respective grid point in the x direction. This leads to a system

of linear equations with tridiagonal matrices

$$\begin{pmatrix} {}_2X_1 & {}_3X_1 & 0 & 0 & \cdots & 0 & 0 & 0 \\ {}_1X_2 & {}_2X_2 & {}_3X_2 & 0 & \cdots & 0 & 0 & 0 \\ 0 & {}_1X_3 & {}_2X_3 & {}_3X_3 & \cdots & 0 & 0 & 0 \\ \vdots & \vdots & \vdots & \vdots & \ddots & \vdots & \vdots & \vdots \\ 0 & 0 & 0 & 0 & \cdots & {}_1X_{N-1} & {}_2X_{N-1} & {}_3X_{N-1} \\ 0 & 0 & 0 & 0 & \cdots & 0 & {}_1X_N & {}_2X_N \end{pmatrix} \begin{pmatrix} \psi_1(t+\Delta t) \\ \psi_2(t+\Delta t) \\ \psi_3(t+\Delta t) \\ \vdots \\ \psi_{N-1}(t+\Delta t) \\ \psi_N(t+\Delta t) \end{pmatrix}$$
$$= \begin{pmatrix} {}_2Y_1 & {}_3Y_1 & 0 & 0 & \cdots & 0 & 0 & 0 \\ {}_1Y_2 & {}_2Y_2 & {}_3Y_2 & 0 & \cdots & 0 & 0 & 0 \\ 0 & {}_1Y_3 & {}_2Y_3 & {}_3Y_3 & \cdots & 0 & 0 & 0 \\ \vdots & \vdots & \vdots & \vdots & \ddots & \vdots & \vdots & \vdots \\ 0 & 0 & 0 & 0 & \cdots & {}_1Y_{N-1} & {}_2Y_{N-1} & {}_3Y_{N-1} \\ 0 & 0 & 0 & 0 & \cdots & 0 & {}_1Y_N & {}_2Y_N \end{pmatrix} \begin{pmatrix} \psi_1(t) \\ \psi_2(t) \\ \psi_3(t) \\ \vdots \\ \psi_{N-1}(t) \\ \psi_N(t) \end{pmatrix}, \tag{2.15}$$

where N is the total number of grid points in the x direction and

$${}_1X_n = \frac{i\Delta t}{2(\Delta x)^2}A_n(y) - \frac{i\Delta t}{4\Delta x}B_n(y), \tag{2.16}$$

$${}_2X_n = 1 - \frac{i\Delta t}{(\Delta x)^2}A_n(y) + \frac{i\Delta t}{2}V_n(y), \tag{2.17}$$

$${}_3X_n = \frac{i\Delta t}{2(\Delta x)^2}A_n(y) + \frac{i\Delta t}{4\Delta x}B_n(y), \tag{2.18}$$

$${}_1Y_n = -\frac{i\Delta t}{2(\Delta x)^2}A_n(y) + \frac{i\Delta t}{4\Delta x}B_n(y), \tag{2.19}$$

$${}_2Y_n = 1 + \frac{i\Delta t}{(\Delta x)^2}A_n(y) - \frac{i\Delta t}{2}V_n(y), \tag{2.20}$$

$${}_3Y_n = -\frac{i\Delta t}{2(\Delta x)^2}A_n(y) - \frac{i\Delta t}{4\Delta x}B_n(y). \tag{2.21}$$

There are a number of algorithms to solve this system of equations, such as the forward and backward substitution [76]. The matrix multiplication of the right-hand side can be carried out straightforward. For the left-hand side, one gets that $\psi_1(t+\Delta t)$ depends on $\psi_2(t+\Delta t)$ from the first line. After substitution to the second line, one gets that $\psi_2(t+\Delta t)$ depends on $\psi_3(t+\Delta t)$ and

so on. Finally, in the last line, one obtains the value of $\psi_N(t+\Delta t)$. Now one just inserts this value into the $(N-1)$th line and gets $\psi_{N-1}(t+\Delta t)$. One can continue this procedure until the whole wave function is determined.

2.3 Boundary conditions

We must pay special attentions to the borders of the grid, especially when using symmetric or antisymmetric wave functions (half of the grid in use), cylindrical coordinates, and spherical coordinates.

If we use a symmetric wave function in x, which has the grid points defined in the positive x direction from $\frac{\Delta x}{2}$ through $(N-\frac{1}{2})\Delta x$, the other side in the negative x direction is just a symmetric mirror of the positive side. Further considering $\psi\left(-\frac{\Delta x}{2}\right) = \psi\left(+\frac{\Delta x}{2}\right)$ (or $\psi_0 = \psi_1$), we have

$$\frac{\partial}{\partial x}\psi_1 = \frac{\psi_2 - \psi_0}{2\Delta x} = \frac{\psi_2 - \psi_1}{2\Delta x}, \tag{2.22}$$

$$\frac{\partial^2}{\partial x^2}\psi_1 = \frac{\psi_0 - 2\psi_1 + \psi_2}{(\Delta x)^2} = \frac{\psi_2 - \psi_1}{(\Delta x)^2}. \tag{2.23}$$

This leads to coefficients in Eqn. (2.21) as

$${}_2X_1 = 1 - \frac{i\Delta t}{2(\Delta x)^2}A_1(y) - \frac{i\Delta t}{4\Delta x}B_1(y) + \frac{i\Delta t}{2}V_1(y), \tag{2.24}$$

$${}_2Y_1 = 1 + \frac{i\Delta t}{2(\Delta x)^2}A_1(y) + \frac{i\Delta t}{4\Delta x}B_1(y) - \frac{i\Delta t}{2}V_1(y). \tag{2.25}$$

For an antisymmetric wave function ($\psi_0 = -\psi_1$), the respective equations are

$$\frac{\partial}{\partial x}\psi_1 = \frac{\psi_2 - \psi_0}{2\Delta x} = \frac{\psi_2 + \psi_1}{2\Delta x}, \tag{2.26}$$

$$\frac{\partial^2}{\partial x^2}\psi_1 = \frac{\psi_0 - 2\psi_1 + \psi_2}{(\Delta x)^2} = \frac{\psi_2 - 3\psi_1}{(\Delta x)^2}, \tag{2.27}$$

$${}_2X_1 = 1 - \frac{3i\Delta t}{2(\Delta x)^2}A_1(y) + \frac{i\Delta t}{4\Delta x}B_1(y) + \frac{i\Delta t}{2}V_1(y), \tag{2.28}$$

$${}_2Y_1 = 1 + \frac{3i\Delta t}{2(\Delta x)^2}A_1(y) - \frac{i\Delta t}{4\Delta x}B_1(y) - \frac{i\Delta t}{2}V_1(y). \tag{2.29}$$

For the radial coordinate in cylindrical and spherical coordinates one assumes $\psi\left(-\frac{\Delta x}{2}\right) = \psi\left(+\frac{\Delta x}{2}\right)$ and the above equations for the symmetric wave functions can be used.

The angular coordinate in cylindrical coordinates leads to the boundary condition $\psi_N = \psi_1$, which can be achieved by padding the grid points with this periodic boundary condition in mind. Similar treatment can be used for spherical coordinates.

2.4 The imaginary-time-propagation method

The imaginary-time-propagation method [77] is a way to obtain the eigenstates of the system studied. Within the imaginary-time-propagation method, the eigenstates are calculated in the order of their energies. That is to say, the ground state needs to be obtained first, then the first excited state, and next the second excited state and so on. First, we start from an arbitrarily chosen initial guess for the ground-state wave function of the system ψ, which can be expanded in terms of the still-unknown eigenstates of the system

$$\psi(0) = \sum_n c_n \psi_n(0), \tag{2.30}$$

the time-evolved version of which is

$$\psi(\Delta t) = \sum_n c_n \psi_n(\Delta t) = \sum_n c_n \psi_n(0) e^{-iE_n \Delta t}, \tag{2.31}$$

where c_n is the expansion coefficient and E_n is the eigenenergy of the n-th eigenstate.

Instead of using the real time Δt for the time propagation, we use an imaginary Δt. Thus, let us substitute $\Delta t = -i\Delta\tau$, where $\Delta\tau$ is now a real time, we then have

$$\psi(\Delta t) = \sum_n c_n \psi_n(0) e^{-E_n \Delta\tau}. \tag{2.32}$$

Since the ground state has the lowest energy E_0, the weight of the ground state in the full wave function grows with time as compared to excited states.

By carrying out the imaginary time propagation multiple times and normalizing the full wave function after each time step, one will finally obtain the ground state of the system when convergence is reached. The criteria for convergence can be the energy of the state, i.e., when the calculated energy of the previous time step is approximately equal to the energy of the current step. In this thesis, we use an absolute error of 10^{-16} a.u. in all results presented.

The first excited state can be obtained in the same way, but one needs to project out the ground state from the full wave function (using Gram–Schmidt orthogonalization) at each time step. Similarly, higher excited states can be obtained by projecting out all lower states.

2.5 The spectral method

The eigenenergies can be obtained very accurately using the imaginary-time-propagation method since the convergence criteria based on the eigenenergy can be chosen very strict, and the eigenstates are also reasonably accurate. However, if we propagate the eigenstates without external field, we can often still see a very small portion of the probability coming out from the bound eigenstates. This indicates that the eigenstates obtained using the imaginary-time-propagation method are not extremely accurate. This may not be a problem when we study strong ionization, in which the ionization signal overwhelms the error, it may however pose a risk to the cases of weak ionization.

To solve this problem, we can propagate the eigenstates in the free field for a long time until the fake ionization signals have gone out of the grid and normalize the eigenstates again. Alternatively, we can use the spectral method [78] to improve the eigenstates, whose accuracy depends on that of the eigenenergies here.

The spectral method is based on the spectral properties of the Hamiltonian. Using this method, both eigenenergies and eigenstates can be obtained. Following is a brief review of the spectral method [78] that we only present for the nondegenerate case here. To this end, we write the solution to the TDSE as a superposition of eigenstates

$$\psi(\boldsymbol{r},t)=\sum_n A_n u_n(\boldsymbol{r})\exp(-iE_nt), \tag{2.33}$$

where A_n is the coefficient, $u_n(\boldsymbol{r})$ is the eigenstate, and E_n is the corresponding eigenenergy. Let us define the correlation function $J(t)$ as

$$J(t)=\langle\psi(\boldsymbol{r},0)|\psi(\boldsymbol{r},t)\rangle=\sum_n |A_n|^2\exp(-iE_nt), \tag{2.34}$$

and its Fourier transform is

$$J(E) = \sum_n |A_n|^2 \delta(E - E_n). \tag{2.35}$$

As it is obvious from the equation above, we can get the spectrum of the correlation function with infinitely sharp peaks corresponding to the eigenenergies of the system if we record the correlation function $J(t)$ for an infinitely long time. However, in reality this is of course impossible. Instead, we can only record $J(t)$ up to a certain time T, and the resonances have the form $\sin[(E - E_n)T/2]/(E - E_n)$, whose sidelobes might confuse the overall spectrum. To overcome this problem, we can add a normalized Hanning window function $w(t)/T$ to the correlation function

$$J(t) = \sum_n |A_n|^2 \frac{w(t)}{T} \exp(-iE_n t), \tag{2.36}$$

where

$$w(t) = \begin{cases} 1 - \cos(2\pi t/T), & (0 \leqslant t \leqslant T) \\ 0, & (t > T) \end{cases} \tag{2.37}$$

and thus

$$J(E) = \sum_n |A_n|^2 L(E - E_n), \tag{2.38}$$

where $L(E - E_n)$ is a lineshape function corresponding to the Fourier transform of the window function. Therefore, the eigenenergies of the system can be obtained all at once, from the spectrum properties of the Hamiltonian corresponding to the system. Shown in Fig. 2.1 is the spectrum of the hydrogen atom obtained with a cylindrical 2D model.

After the eigenenergies are known, the eigenstates corresponding to the eigenenergies can be obtained. To this end, we multiply both sides of Eqn. (2.33) by $w(t)\exp(iEt)/T$ and integrate from 0 to T, which yields

$$\psi(\boldsymbol{r}, E) = \int_0^T \psi(\boldsymbol{r}, t) \frac{w(t)}{T} \exp(iEt) dt = \sum_n A_n u_n(\boldsymbol{r}) L(E - E_n). \tag{2.39}$$

The eigenstate $u_m(\boldsymbol{r})$ corresponding to the eigenenergy E_m can be obtained by substituting E_m to the equation above, i.e.,

$$\psi(\boldsymbol{r}, E_m) = A_m u_m(\boldsymbol{r}) L(0) + \sum_{n \neq m} A_n u_n(\boldsymbol{r}) L(E_m - E_n) \approx A_m u_m(\boldsymbol{r}) L(0). \tag{2.40}$$

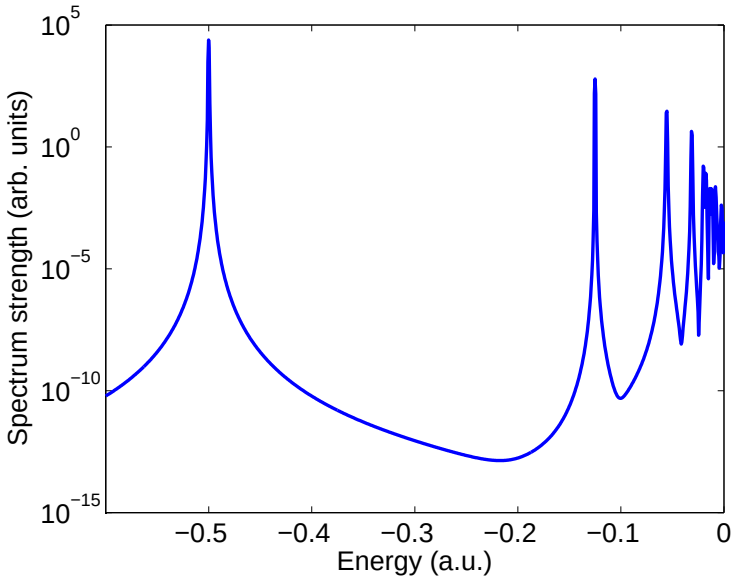

Figure 2.1. The spectrum of the Cylindrical 2D hydrogen atom. The peaks correspond to the eigenenergies of the atom. Parameters are $\Delta\rho = \Delta z = 0.1$, $N_\rho = N_z = 1000$, $\Delta t = 0.01$, recording time $T = 10000$.

The advantage of the spectral method, as mentioned above, is that all the eigenenergies of the system can be obtained at once, as long as the correlation function is recorded long enough so that its Fourier transform shows sharp peaks corresponding to the eigenenergies. However, to get an eigenenergy as accurate as the results from the imaginary-time-propagation method is very time consuming. Thus, if we only need to obtain the ground state and a few excited states, we can use the imaginary-time-propagation method, which yields very accurate eigenenergies and reasonably accurate eigenstates, which can then be improved using the spectral method based on the accurate eigenenergies corresponding to the eigenstates obtained. Otherwise, if we need to obtain highly excited states, we can use the spectral method to obtain both eigenenergies and eigenstates.

2.6 Absorbing boundaries

The essence of the grid-based numerical method is to initially keep the entire wave function on the grid. However, when ionization happens, the wave packet may reach the border of the grid. In order to hold the outgoing parts of the wave function on the grid, the grid space needs to be large, which is time and memory consuming for a numerical simulation.

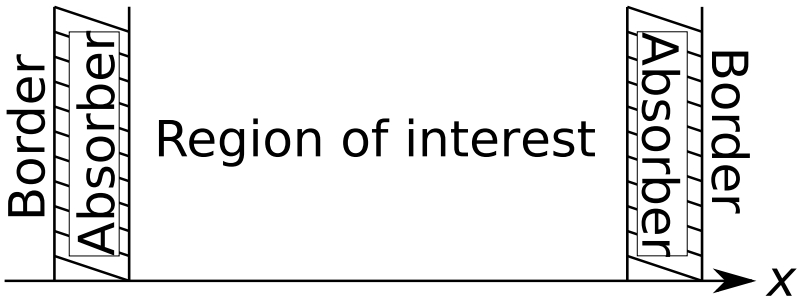

Figure 2.2. The scheme of the absorbing-boundary method.

To overcome this difficulty, grids with absorbing boundaries are used. Without absorbing boundaries, using a border would be equivalent to having an infinitely high wall, which would induce strong reflections of the wave packet that easily obscure the relevant physics. On the other hand, with absorbing boundaries, which introduces a smooth transition between the region of interest and the border, minimal reflections occur. The scheme of the absorbing-boundary method

is illustrated in Fig. 2.2.

There are two major types of absorbing boundaries used in the grid-based numerical simulations, i.e., the mask-function method [79] and the exterior-complex-scaling method [80, 81].

2.6.1 The mask-function method

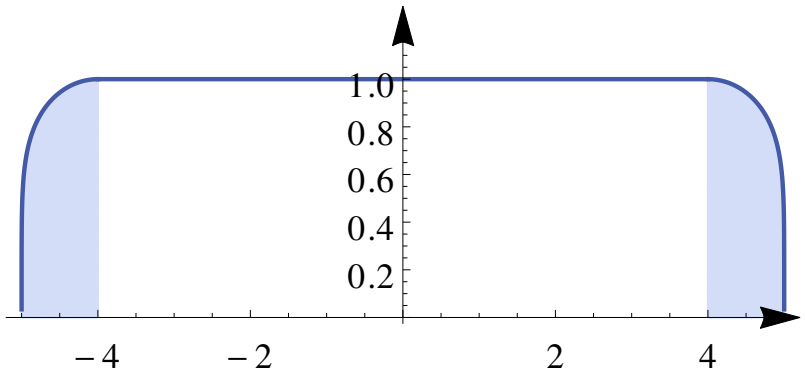

Figure 2.3. The typical shape of the mask function. The index γ is chosen to be 1/6 and the absorber (shaded area) spans 10% of the grid size in each direction.

In the mask function method [79], the probability is multiplied by a function in each time step, which introduces a smooth and gradual change of the probability to 0 at the border of the grid. Usually, the form of the mask function is

$$f(x) = \begin{cases} \cos^{\gamma}\left(\frac{\pi}{2}\frac{|x-x_0|}{L}\right), & (|x| > |x_0|) \\ 1, & (|x| \leqslant |x_0|) \end{cases} \tag{2.41}$$

where x_0 denotes the border of the absorber region and L is its width. The absorber is usually chosen to span 10% of the grid size in each direction and common choices of the index γ are 1/6, 1/8, etc. Shown in Fig. 2.3 is the typical shape of the mask function.

The mask-function method is usually good enough to suppress the reflection of the probability from the border. However, in case of a strong ionization (with an ionization yield larger than 10^{-2}), the reflections may become remarkable. In this case, we need to use alternative methods such as the exterior-complex-scaling method.

2.6.2 The exterior-complex-scaling method

The idea of the exterior-complex-scaling method [80, 81] is to rotate the coordinate of the particle by an angle η ($0 < \eta < \pi/2$) into the complex plane when it is larger than a certain value x_0 (border of the absorber), $x \to xe^{i\eta}$, or

$$x \to \begin{cases} x, & (|x| \leqslant |x_0|) \\ |x_0| + (x - |x_0|)e^{i\eta}, & (x > |x_0|) \\ -|x_0| + (x + |x_0|)e^{i\eta}. & (x < -|x_0|) \end{cases} \tag{2.42}$$

By means of this transformation, the wave function is kept unchanged when $|x| \leqslant |x_0|$ and falls off exponentially when $|x| > |x_0|$ due to the decaying factor in the propagation operator present in this transformation. A similar method with the same goal is the complex-absorbing-potential method [82–84], in which an additional complex potential is added to the Coulomb potential for $|x| > |x_0|$

$$V(x) \to \begin{cases} V(x), & (|x| \leqslant |x_0|) \\ V(x) + i\eta W(x). & (|x| > |x_0|) \end{cases} \tag{2.43}$$

The advantage of the exterior-complex-scaling method, in most cases, is that it leads to a better absorption than the mask-function method. The advantage of the mask-function method, on the other hand, is that different ionization yields, such as single and double-ionization yields, can be obtained separately, when used together with the space-partitioning method presented below.

2.7 The space-partitioning method

The space-partitioning method [85] is a numerical method to separate single and double-ionization contributions from the whole wave function. The essence of this method lies in the fact that the bound state, the single-ionization wave packet, and the double-ionization wave packet are separated in the two-particle space. Considering an atomic system for example, both electrons are located near the nucleus in the bound states, one of the electrons remains located near the nucleus

while the other is far from the nucleus in the event of single ionization, and both electrons are far from the nucleus in the double ionization process. This observation enables us to spatially separate the different contributions in the full wave function.

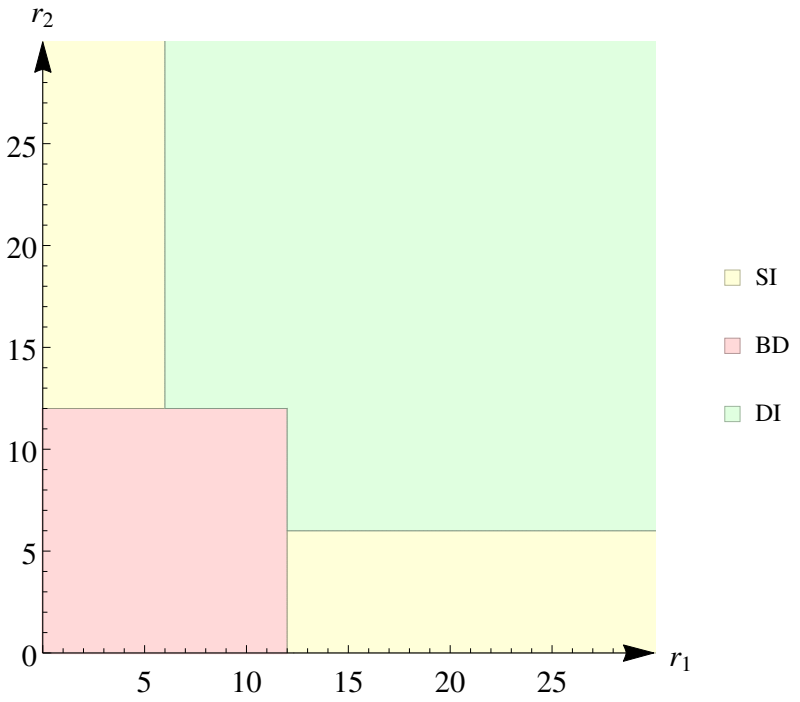

Figure 2.4. The space partitioning for an atom with $d_{\text{small}} = 6$ and $d_{\text{big}} = 12$.

Specifically, for an atomic system, the different contributions, i.e., the bound state (BD), the single-ionization part (SI), and the double-ionization part (DI), can be identified as

(1) BD: $r_1 \leqslant d_{\text{big}} \cap r_2 \leqslant d_{\text{big}}$;

(2) SI: $(r_1 \leqslant d_{\text{small}} \cap r_2 > d_{\text{big}}) \cup (r_2 \leqslant d_{\text{small}} \cap r_1 > d_{\text{big}})$;

(3) DI: $(r_1 > d_{\text{small}} \cap r_2 > d_{\text{big}}) \cup (r_2 > d_{\text{small}} \cap r_1 > d_{\text{big}})$,

where $r_1 = |x_1|$ is the distance of the first electron to the nucleus, $r_2 = |x_2|$ is that of the second electron to the nucleus, and d_{small} and d_{big} are the two bounds to distinguish different contributions in the full wave function. Such an atomic partitioning for $d_{\text{small}} = 6$ and $d_{\text{big}} = 12$ is illustrated in Fig. 2.4.

For a diatomic system (two-center system), the partitioning becomes complex, although the basic principle remains simple, i.e., the two electrons are located near either nuclei but not near the same nuclei for the bound state, one of the electrons is located near one of the nuclei while the other is far from the other nucleus for the single ionization event, and both electrons are far from the nuclei for double ionization.

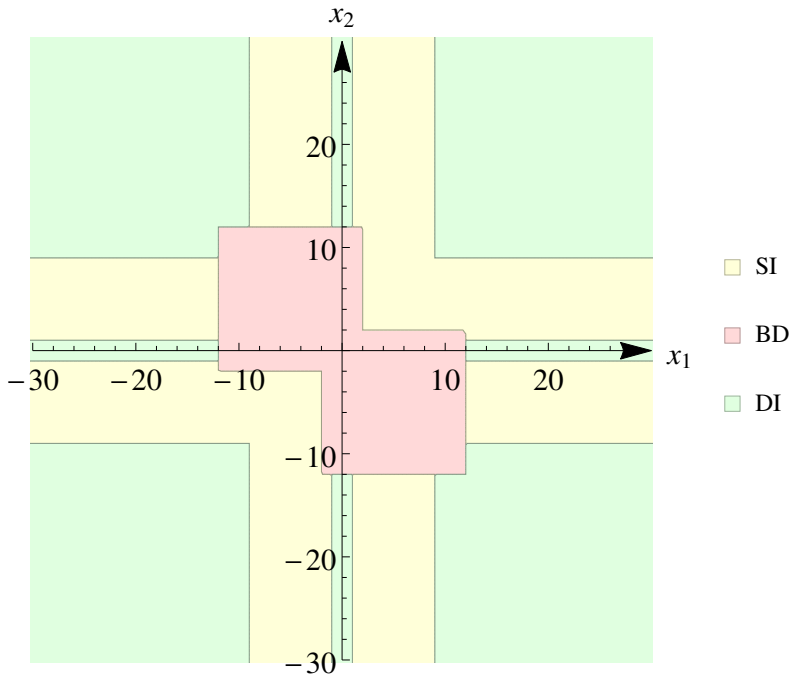

Figure 2.5. The space partitioning for a diatomic system (atomic nature) in the direction of the molecular axis with $R = 10$, $d_{\text{small}} = 4$ and $d_{\text{big}} = 7$.

Specifically, for such a diatomic system (of atomic nature), the different contributions, i.e., BD, SI, and DI, after assuming the middle of the two nuclei as the origin and defining $r_{11} = |x_1 - R/2|$, $r_{12} = |x_1 + R/2|$, $r_{21} = |x_2 - R/2|$, and $r_{22} = |x_2 + R/2|$ with R standing for the internuclear distance, can be identified as

(1) BD: $(r_{11} \leqslant d_{\text{big}} \cap r_{22} \leqslant d_{\text{big}}) \cup (r_{12} \leqslant d_{\text{big}} \cap r_{21} \leqslant d_{\text{big}})$;

(2) SI: $((r_{11} \leqslant d_{\text{small}} \cap r_{22} > d_{\text{big}}) \cup (r_{22} \leqslant d_{\text{small}} \cap r_{11} > d_{\text{big}}) \cup (r_{12} \leqslant d_{\text{small}} \cap r_{21} > d_{\text{big}}) \cup (r_{21} \leqslant d_{\text{small}} \cap r_{12} > d_{\text{big}})) \cap (r_{11} > d_{\text{big}} \cup r_{22} > d_{\text{big}}) \cap (r_{12} > d_{\text{big}} \cup r_{21} > d_{\text{big}})$;

(3) DI: $((r_{11} > d_{\text{small}} \cap r_{22} > d_{\text{big}}) \cup (r_{22} > d_{\text{small}} \cap r_{11} > d_{\text{big}})) \cap ((r_{12} > d_{\text{small}} \cap r_{21} > d_{\text{big}}) \cup (r_{21} > d_{\text{small}} \cap r_{12} > d_{\text{big}}))$,

and shown in Fig. 2.5 with $R = 10$, $d_{\text{small}} = 4$ and $d_{\text{big}} = 7$.

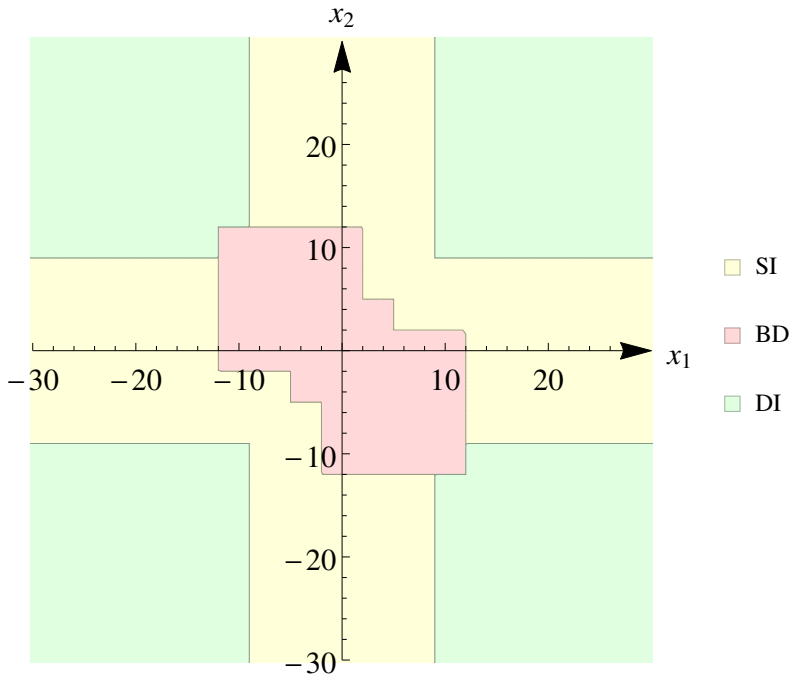

Figure 2.6. The space partitioning for a diatomic system (molecular nature) in the direction of the molecular axis with $R = 10$, $d_{\text{small}} = 4$ and $d_{\text{big}} = 7$.

If, however, we further identify the wave packet between the two nuclei as bound and one of the electrons between the nuclei and the other far from the nuclei as single ionization, we can instead identify the different contributions for such a diatomic system (of molecular nature) as

(1) BD: $(r_{11} \leqslant d_{\text{big}} \cap r_{22} \leqslant d_{\text{big}}) \cup (r_{12} \leqslant d_{\text{big}} \cap r_{21} \leqslant d_{\text{big}}) \cup (r_1 \leqslant R/2 \cap r_2 \leqslant R/2)$;

(2) SI: $((((r_{11} \leqslant d_{\text{small}} \cap r_{22} > d_{\text{big}}) \cup (r_{22} \leqslant d_{\text{small}} \cap r_{11} > d_{\text{big}}) \cup (r_{12} \leqslant d_{\text{small}} \cap r_{21} > d_{\text{big}}) \cup (r_{21} \leqslant d_{\text{small}} \cap r_{12} > d_{\text{big}})) \cap (r_{11} > d_{\text{big}} \cup r_{22} > d_{\text{big}}) \cap (r_{12} > d_{\text{big}} \cup r_{21} > d_{\text{big}})) \cup ((r_{11} > d_{\text{big}} \cup r_{22} > d_{\text{big}}) \cap (r_{12} > d_{\text{big}} \cup r_{21} > d_{\text{big}}) \cap (r_1 \leqslant R/2 \cup r_2 \leqslant R/2))) \cap (r_1 > R/2 \cup r_2 > R/2)$;

(3) DI: $((r_{11} > d_{\text{small}} \cap r_{22} > d_{\text{big}}) \cup (r_{22} > d_{\text{small}} \cap r_{11} > d_{\text{big}})) \cap ((r_{12} > d_{\text{small}} \cap r_{21} > d_{\text{big}}) \cup (r_{21} > d_{\text{small}} \cap r_{12} > d_{\text{big}})) \cap (r_1 > R/2 \cap r_2 > R/2)$,

which is exemplified in Fig. 2.6 with $R = 10$, $d_{\text{small}} = 4$ and $d_{\text{big}} = 7$.

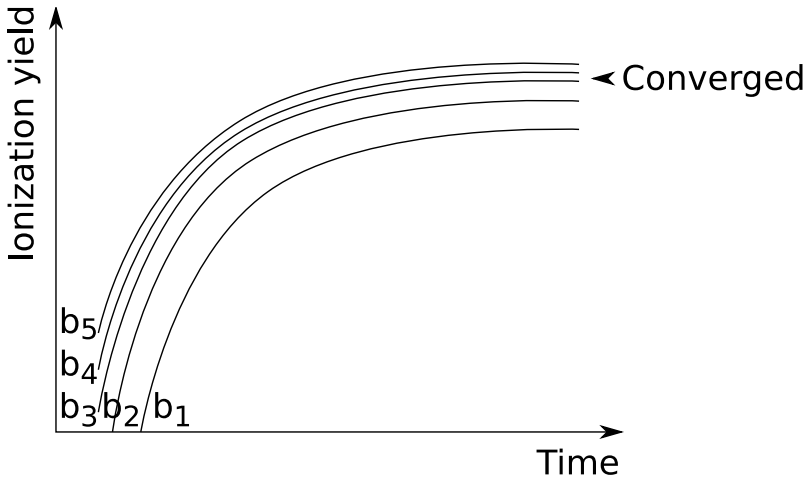

Figure 2.7. The schematic illustration of the way to choose the bounds in the space-partitioning method.

The bounds d_{small} and d_{big} are chosen such that the final single and double ionization yields do not change significantly upon variation about their values. To this end, we first increase d_{big} gradually starting from a small value, and for each d_{big} we propagate the initial state in the laser field long after the end of the pulse until the single ionization yield converges. From the change in the final single ionization yield as a function of d_{big}, we choose the smallest value of d_{big} such that the yield does not change significantly for larger values. After choosing a value for d_{big}, we then increase d_{small} gradually starting from a small value, and for each d_{small} we propagate the initial state in the laser field until the double ionization yield converges. From the double ionization yield as a function of d_{small}, we choose a value for d_{small} beyond which the yields does not change significantly. After these procedures, both values of d_{small} and d_{big} are fixed. Shown in Fig. 2.7 is a schematic illustration of this method, in which $b_1 < b_2 < b_3 < b_4 < b_5$, and the final ionization yield is essentially converged at b_3.

2.8 Calculating single and double-ionization yields

The space-partitioning method, when used together with the mask-function method, provides a way to calculate single and double-ionization yields by accumulating the probability absorbed by the boundary. The single and double-ionization rate at a certain time t can be written as

$$R_{\mathrm{SI}}(t) = \frac{1}{\Delta t}\int_{\mathrm{SI}} |\psi(x,t)|^2 dx - \frac{1}{\Delta t}\int_{\mathrm{SI}} M(x)|\psi(x,t)|^2 dx, \tag{2.44}$$

$$R_{\mathrm{DI}}(t) = \frac{1}{\Delta t}\int_{\mathrm{DI}} |\psi(x,t)|^2 dx - \frac{1}{\Delta t}\int_{\mathrm{DI}} M(x)|\psi(x,t)|^2 dx, \tag{2.45}$$

where $M(x)$ is the mask function, and the integrations are carried over the respective ionization regions identified by the space-partitioning method. The corresponding ionization yields are

$$P_{\mathrm{SI}}(T) = \int_0^T R_{\mathrm{SI}}(t)dt, \tag{2.46}$$

$$P_{\mathrm{DI}}(T) = \int_0^T R_{\mathrm{DI}}(t)dt, \tag{2.47}$$

where the integration time T needs to be large enough so that all the ionized wave packet reaches the boundary.

When ionization time matters, i.e., when we need to find out when the ionized wave packet comes out from the system, the wave packet can be considered as single ionization immediately after it enters the single-ionization region, and the wave packet can be regarded as double ionization immediately after it enters the double-ionization region, as opposed to the previous case where it is considered as ionization only when the probability gets absorbed by the boundary. In this case, the ionization yields can be written as

$$P'_{\mathrm{SI}}(T) = \int_0^{T-\Delta t} R_{\mathrm{SI}}(t)dt + \int_{\mathrm{SI}} |\psi(x,T)|^2 dx, \tag{2.48}$$

$$P'_{\mathrm{DI}}(T) = \int_0^{T-\Delta t} R_{\mathrm{DI}}(t)dt + \int_{\mathrm{DI}} |\psi(x,T)|^2 dx. \tag{2.49}$$

The first method, i.e., collecting the electrons at the boundary, is used to calculate the single and double-ionization yields in this thesis, unless stated otherwise. The second method is only used when we need to obtain the ionization time directly from the spatial distribution of the wave function (refer to Sec. 5.3.2.2).

2.9 Parallel computation

Studies of correlated electron dynamics, where two or more electrons are involved, require higher dimensional calculations and parallelization of the code. There are two methods for code parallelization, namely shared-memory parallelization and distributed-memory parallelization.

Shared-memory parallelization means that all working threads share the same common memory that resides in the same (physical or virtual) compute node. OpenMP is typically used to implement shared-memory parallelization. The advantage of this method is that the memory is shared between different working threads and thus minimum communication between different threads is needed, which makes this method fast and effective. The disadvantage, on the other hand, is that the maximum number of threads in a single compute node where the common memory resides is limited and thus the parallelization is restricted to a few threads, typically 12 or 16 currently, depending on how many cores or threads the compute node has.

Distributed-memory parallelization means that all working threads carry their own private memories that do not necessarily locate in the same compute node. MPI is typically used to implement distributed-memory parallelization. The advantage of this method is that the number of available working threads is not limited to the number of cores or threads in a single compute node, and its number can reach the maximum available threads within a whole cluster. The disadvantage, on the other hand, is that the memory is distributed between different working threads, and if the different threads work together to calculate the same physical quantity, heavy communications between threads can be induced. While the communication within the same compute node is fast, that between different nodes can be very slow depending on the speed of ethernet and the amount of messages to be passed across compute nodes.

In our case, where we study correlated electron dynamics, different parts of the full wave function are highly correlated. If we use distributed-memory parallelization, heavy communications are needed which would become a bottleneck in scaling up the performance. So we choose the shared-memory parallelization for our code. We have also estimated that using distributed-

memory parallelization, a minimum performance boost, if any, would be achieved as compared to using shared-memory parallelization, even if we use a lot more compute nodes. Cost-effectively, we thus stick to the shared-memory parallelization, i.e., using OpenMP, for the purpose of code parallelization.

Using OpenMP is very easy, straightforward, and induces minimum changes to the single-threaded code. The minimum working example below shows the comparison between the single-threaded code (left column) and OpenMP parallelized multiple-threaded code (right column), where the number of threads to use can be determined by the environmental variable `OMP_NUM_THREADS`.

```
1 int i;
2
3 for(i=0; i<N; i++)
4 {
5   // code here
6 }
```

```
1 int i;
2 #pragma omp parallel for private(i)
3 for(i=0; i<N; i++)
4 {
5   // code here
6 }
```

As we can see, only one line starting with the `#pragma` compiler directive is added which tells the compiler to compile with OpenMP (if, say, the argument `-fopenmp` is passed to the `g++` compiler). The variables inside the parenthesis of the `private` keyword are the private variables of each working thread that are not to be shared between different threads. If operators like accumulation are used, the `reduction` method is necessary to avoid the case when different threads add to the same variable simultaneously and the variable loses track of some additions. A minimum example is given as follows. In this case, each thread keeps a private copy of the variable `sum` and performs the addition of `sum` from each thread at the end.

```
1 int i;
2 int sum=0;
3 #pragma omp parallel for private(i) reduction(+:sum)
4 for(i=0; i<N; i++)
5 {
6   // code here
7   sum += i;
8 }
```

If, by any means, we have to disable parallelization, we only need to set the environmental

variable `OMP_NUM_THREADS` to 1, or, at compile time, omit the argument `-fopenmp` of the `g++` compiler. Hence, adding such compiler directive as `#pragma` does not add much to the working load and does not induce any harm to the computation since we can turn it off at any time. Therefore, we strongly suggest to always parallelize the code using OpenMP even if we do not use it later on.

To reach the maximum performance, we need to use parallelization whenever possible. If we parallelize the code everywhere else but leave one segment single-threaded, then this segment may become the bottleneck. Furthermore, to reduce the parallelization initialization and collection overhead, we usually parallelize the outermost loop if there are more than one loops. At the same time, the sequence of the loops needs to be arranged in such a way that the rule of strided memory access is obeyed, i.e., the memory needs to be accessed in a continuous flow, in order to maximize the performance.

Chapter 3

Single and double photoionization of the helium dimer[1]

In this chapter, we study the energy exchange via electron correlation upon photon absorption over large distances in double photoionization of the helium dimer. Results of numerical simulations of the interaction of a planar 4D helium dimer model with a short light pulse are found to be in good agreement with recent experimental data for the angular distribution of the emitted electron. The double ionization probability is closely related to that of the photoemission of an electron from one of the helium atoms along the internuclear axis. Together with an analysis of the temporal evolution of the two-electron probability distribution, this provides direct evidence for the knockout mechanism by which the photon energy is shared between the electrons over distances of several Angstroms in the dimer.

Based on the results of numerical simulations, we further study the scattering effects in single and double photoionization of the helium dimer. To this end, we use abridged Hamiltonians in which different interactions between the electrons and the laser field and/or between the charged particles are removed from the full Hamiltonian. By comparing photoelectron angular distributions obtained in respective numerical simulations, we are able to identify the role of the Coulomb interactions between the electrons and between the electrons and the nuclei for the primary as well as the knockout electron in the processes.

[1] The results of this chapter are in part based on "H. Ni, C. Ruiz, R. Dörner, and A. Becker, Phys. Rev. A **88**, 013407 (2013)" [86] and "H. Ni and A. Becker, Phys. Rev. A **89**, 033402 (2014)" [87].

3.1 Introduction

Despite recent studies on correlated electron dynamics [51, 59–74], the role of electron correlation in double photoionization of a molecule, in particular, regarding the recently observed energy exchange between electrons over distances of several Angstroms [74], is still less understood than in the atomic case. In this respect rare gas dimers, which are formed via the attractive van der Waals interaction by two atoms at larger equilibrium distances than those in a typical diatomic molecule, are interesting targets. Among them, the helium dimer is by far the most extended. Here, interatomic Coulombic decay (ICD) [88], as well as double photoionization [89], which are both mediated by electron-correlation effects, have been observed recently.

In double photoionization, the energy of a single photon absorbed from the light field is shared between two electrons, leading to the correlated emission of both electrons from the target. In a rare gas dimer, the two emitted electrons can either originate from the same atom or from different atoms. Due to the strong localization of electrons in the dimer, the minimum energy required for the emission of two electrons from different atoms in the dimer is about twice the energy for single ionization of the rare gas atom. For He_2, this minimum energy is about 49.2 eV, which is considerably smaller than the energy of about 79 eV needed for emission of both electrons from the same helium atom in the dimer. The threshold for ionization plus excitation (to the $n = 2$ state) in He is 65.4 eV. Below this threshold ICD as a double ionization channel is closed. By selecting a photon energy of 49.2 eV $< \hbar\omega <$ 65.4 eV, one can therefore study electron correlation effects in double photoionization of the helium dimers over a bond length of more than 5 a.u., which are not ICD related.

Recent experimental data suggest that the emission of the two electrons in this case proceeds as follows [89]: A primary electron localized at one atom in the helium dimer absorbs the photon energy from the field, then propagates along the internuclear axis and transfers its energy to a second electron in the neighboring helium atom. This process is called knockout in view of the close analogy to a similar mechanism known in double photoionization of atoms [7]. Since the atoms

in the helium dimer are well separated it was further argued [89] that in this case the knockout process can be considered as the photoionization of a helium atom followed by a subsequent electron-impact ionization at the other helium atom in the dimer. This interpretation was supported by a comparison of the experimental data with theoretical results for electron-impact ionization of the helium atom. In this chapter, we analyze the experimental data and the underlying mechanism for double photoionization of the helium dimer via time-dependent *ab-initio* numerical simulations.

However, the role of the interaction between each pair of charged particles during the single and double photoionization processes is still difficult to analyze. In a numerical simulation, in principle, it is possible to remove interactions between certain pairs of particles in the Hamiltonian and compare the results to those obtained with the full Hamiltonian. However, using this technique in an atomic or typical molecular system, the initial state inevitably changes as compared to the full simulation. Consequently, it is difficult to distinguish between the influence of the initial state and dynamic effects when analyzing the role of the removed interactions. In contrast, this method is applicable to rare gas dimers, since they have much larger equilibrium distances than those of typical diatomic molecules. Due to the large internuclear separation and almost negligible overlap between the orbitals of the two atoms, changes in the initial state are small when certain interactions are removed.

As we will further show in this chapter, in the helium dimer it is possible to study the role of individual Coulomb interactions during the single and double photoionization in *ab-initio* numerical simulations. To this end, we consider abridged Hamiltonians, in which certain Coulomb interactions are removed without noticeable change in the initial state. We then compare the angular distributions obtained using the abridged Hamiltonian to those obtained with the full Hamiltonian. In this way we are able to identify the role of each Coulomb interaction during the process. Moreover, we are also able to distinguish and compare the angular distributions of the primary electron and the knockout electron by removing the coupling between one electron and the laser field from the full Hamiltonian.

The remainder of the chapter is organized as follows. We first briefly outline the planar two-

active-electron model of the helium dimer used in the simulations. Then, we analyze the projection to different final states in the calculations to obtain the photoelectron angular distributions and present comparisons with recent experimental data [89]. Based on the good agreement between experimental and theoretical data we proceed to provide evidences towards the knockout mechanism, based on predictions for the dependence of the ionization signals on the orientation of the dimer axis and the separation of the atoms in the dimer, and a real-time visualization of the knockout mechanism behind the long-range electron correlation. Afterwards, we introduce and discuss different abridged Hamiltonians in which certain interactions are removed from the full Hamiltonian. A comparison between the ground states of the full and the abridged Hamiltonians will be given and discussed. We then apply the different Hamiltonians in numerical simulations to study the effects of different interactions in single and double photoionization.

3.2 Numerical simulations

In this section we present the numerical model for the helium dimer used in the simulations, in which one electron at each atom in the dimer is considered as active. We further outline the methods used in the numerical simulations and then present the predictions for the lowest energy eigenstates based on this numerical model.

3.2.1 The planar 4D model of the helium dimer

A solution of the TDSE including the dynamics of all six charged particles and the interaction of all four electrons with the external light field is currently not conceivable. We therefore propose a planar two-active electron model of the helium dimer, in which the electrons are located at different atoms in the dimer and their dynamics is constrained to the same plane, as shown schematically in Fig. 3.1. Such a model excludes ICD but it is well suited to treat the knockout mechanism. The orientation of the dimer axis is chosen to be at an angle θ to the axis of linear polarization of the light field (here, the z-axis). It is further assumed that the correlated emission of the two electrons proceeds fast enough (a few tens of attoseconds, 1 as = 10^{-18} s) to hold the internuclear distance

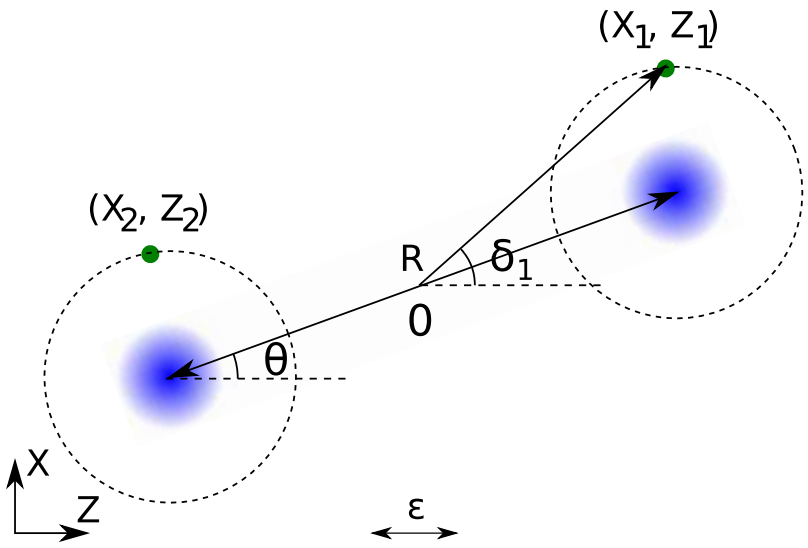

Figure 3.1. Scheme of the numerical model for the helium dimer. One electron at each atom is considered active and restricted to the same plane, with coordinates (x_1, z_1) and (x_2, z_2), respectively. The internuclear distance R and dimer orientation θ with respect to the laser polarization direction ε (z-axis) are fixed during the simulations.

between the atoms as well as the orientation of the dimer axis fixed in space during the simulation. The corresponding four-dimensional (two spatial dimensions for each electron) model Hamiltonian is then given by

$$\begin{aligned} H =& \frac{p_{x_1}^2 + p_{z_1}^2}{2} + \frac{p_{x_2}^2 + p_{z_2}^2}{2} + E(t)\,(z_1 + z_2) \\ &+ V_{\mathrm{SAE}}(r_{11}) + V_{\mathrm{SAE}}(r_{12}) + V_{\mathrm{SAE}}(r_{21}) + V_{\mathrm{SAE}}(r_{22}) \\ &+ \frac{1}{\sqrt{(x_1 - x_2)^2 + (z_1 - z_2)^2 + b^2}} + \frac{1}{R}, \end{aligned} \tag{3.1}$$

where $\boldsymbol{p}_i = (p_{x_i}, p_{z_i})$ and $\boldsymbol{r}_i = (x_i, z_i)$ (with $i = 1, 2$) are the momentum operators and spatial coordinates of the two active electrons and $E(t)$ is the laser field, which is assumed to be linearly polarized in z-direction. R is the internuclear distance that can have different orientations θ with respect to the polarization direction and

$$r_{ij} = \sqrt{\left[x_i + (-1)^j \frac{R}{2}\sin\theta\right]^2 + \left[z_i + (-1)^j \frac{R}{2}\cos\theta\right]^2 + a^2} \tag{3.2}$$

corresponds to the distance between ith electron and jth nucleus ($i, j = 1, 2$) with $a^2 = 0.201$ and $b^2 = 0.01$ denoting soft-core parameters to smooth the Coulomb singularity in the practical computations. The linearly polarized laser field is given in the form of

$$E(t) = \cos^2\left(\frac{\omega t}{2N}\right)\cos\left(\omega t + \phi\right), \tag{3.3}$$

where ω is the central frequency, N is the number of cycles, and ϕ is the carrier-envelope phase of the laser pulse, which is set to $-\pi/2$ in the present simulations.

$$V_{\mathrm{SAE}}(r) = -\frac{Z_{\mathrm{c}} + a_1 \mathrm{e}^{-a_2 r} + a_3 r \mathrm{e}^{-a_4 r} + a_5 \mathrm{e}^{-a_6 r}}{r} \tag{3.4}$$

is a single active electron (SAE) potential for the helium atom with $Z_{\mathrm{c}} = 1.0$, $a_1 = 1.231$, $a_2 = 0.662$, $a_3 = -1.325$, $a_4 = 1.236$, $a_5 = -0.231$, and $a_6 = 0.480$ [90], which we adopt here for the planar case. The TDSE of this 4D model is solved numerically using the Crank–Nicolson method on a grid with $N_{x_1} = N_{x_2} = 200$ and $N_{z_1} = N_{z_2} = 300$ grid points, a grid step of $\Delta x_1 = \Delta x_2 = \Delta z_1 = \Delta z_2 = 0.3$, and a time step of $\Delta t = 0.05$.

In our simulations we considered double photoionization due to the interaction of the model helium dimer with a 4-cycle XUV light pulse at a central wavelength of 20 nm (corresponding to a photon energy of 62 eV and a bandwidth of ±15.5 eV) and a peak intensity of 1×10^{14} W/cm^2. At this bandwidth in a real four-electron system, the ICD channel would be open for the high-energy tail of the pulse. In our two-electron calculations, ICD is however excluded and hence does not obscure our findings. We employed absorbing boundaries of the form $\cos^{1/6}\left(\frac{\pi}{2}\frac{|x-x_0|}{L}\right)$ with $|x| \geqslant |x_0|$, where x_0 denotes the border of the boundary region and L its width. The boundary was chosen to span 10% of the grid size in each direction. In order to calculate the total probabilities and electron angular distributions, we stopped the simulation before the respective part of the wave function reached the boundaries.

In order to analyze the correlated electron emission from the helium dimer and to compare with the experimental data on the photoelectron angular distributions, the contributions to single and double photoionization of the helium dimer were obtained by partitioning the spatial four-dimensional grid as illustrated in Sec. 2.7 for a diatomic system of molecular nature with $d_{\text{small}} = 4$ a.u. and $d_{\text{big}} = 7$ a.u.

3.2.2 Initial states

The lowest energy eigenstates of the model, which we used as initial states for our numerical simulations, are obtained via imaginary time propagation. The initial guess state for the imaginary time propagation was chosen to be a 4D Gaussian wave function. For an internuclear separation of 5.6 a.u., which corresponds to the minimum of the helium dimer potential [91], and orientation of the dimer along the z-axis, spatial distributions of the two lowest energy eigenstates are shown in Fig. 3.2 as functions of z_1 and z_2 (upper row) and $z = z_1 - z_2$ (lower row), respectively. The distributions are integrated over the other coordinates. Due to the large internuclear distance the states are, as expected, very close in energy (−1.80740 a.u. and −1.80726 a.u., respectively), with values close to other theoretical calculations [92]. Note that the emergence of these two separate states is due to our two-active electron model that selects two electrons out of a total of four. The

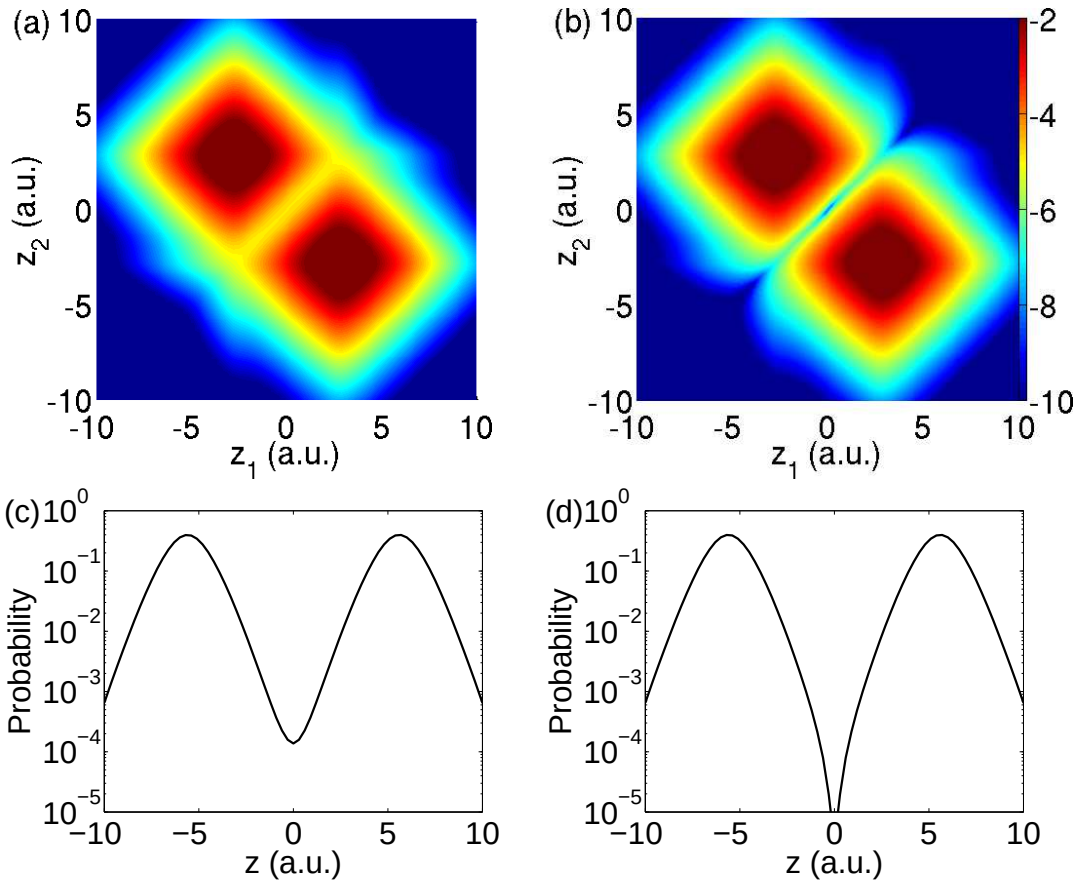

Figure 3.2. Spatial distributions (on a logarithmic scale) of the ground state [panels (a) and (c)] and first excited state [panels (b) and (d)] of the planar model helium dimer. The distributions in the upper row are integrated over x_1 and x_2 and shown as a function of z_1 and z_2. The distributions in the lower row are integrated over x_1, x_2, and $Z = \frac{z_1+z_2}{2}$ and shown as a function of $z = z_1 - z_2$. Note the node (minimum) at $z_1 = z_2$ or $z = 0$ in the distributions of the first excited state.

ground state is a spin-singlet state which has a multiplicity of 1 while the first excited state is a spin-triplet state with a multiplicity of 3. We performed separate simulations for both states as the initial state and present below, if not mentioned differently, the sum of the contributions by taking account of the multiplicity of each state.

3.3 Photoelectron angular distributions

The final state of double photoionization of the dimer represents a state with two electrons in the continuum of a doubly charged two-center potential. In order to obtain photoelectron angular distributions, we intend to project the respective spatial part of the wave function at the end of the simulation onto an approximate final-state wave function. Since an analytical solution of this four-body problem is not known in Cartesian coordinates, we have tested several two-electron wave functions, in which different parts of the full Coulomb interactions between the charged particles have been taken into account. To this end, we express the Coulomb potential between the electrons and the residual ions as well as between the two electrons in the center-of-mass (COM, $X = (x_1 + x_2)/2$ and $Z = (z_1 + z_2)/2$) and relative coordinates ($x = x_1 - x_2$ and $z = z_1 - z_2$) of the two electrons as

$$\begin{aligned} V(x,z;X,Z) &= \frac{1}{\sqrt{x^2+z^2}} \\ &+ \sum_{i,j=1}^{2} V_{\mathrm{SAE}}\left(\sqrt{\left[X-(-1)^i\frac{x}{2}+(-1)^j\frac{R}{2}\sin\theta\right]^2+\left[Z-(-1)^i\frac{z}{2}+(-1)^j\frac{R}{2}\cos\theta\right]^2}\right). \end{aligned} \tag{3.5}$$

For $|X|, |Z|, R \gg |x|, |z|$, V reduces to

$$V(x,z;X,Z) \approx V_{\mathrm{ee}}(x,z) = \frac{1}{\sqrt{x^2+z^2}}, \tag{3.6}$$

which suggests to approximate the final state as a product of a Coulomb wave in the relative and a plane wave in the COM coordinates, which we denote as ψ_{ee}. Thus, in this approximation the Coulomb interaction between the two electrons is retained while the Coulomb interactions between the electrons and the nuclei are neglected. In order to approximately test the relative importance of the Coulomb interactions in the final state, we have further considered the case in which the

interaction between the electrons is neglected. As a further approximation we then assumed that the total charge of the nuclei is concentrated at the center of the coordinate system. In this approximation the full potential reduces to

$$V(x,z;X,Z) \approx V_{\mathrm{eN}}(X,Z) = -\frac{4}{\sqrt{X^2+Z^2}}, \tag{3.7}$$

and the final state ψ_{eN} is approximated by a product of a plane wave in the relative and a Coulomb wave in the COM coordinates of the electrons for a monomer with twice the residual charge. As a third option, we also considered a simple product of two plane wave functions to describe the final state wave function of the two electrons, which we denote as ψ_{plane}.

Since our model is planar, we used a two-dimensional scattering wave function [93, 94] for the Coulomb wave,

$$\begin{aligned}\psi(\boldsymbol{k},\boldsymbol{r}) = \sum_{l=-\infty}^{\infty} \frac{e^{-\pi\eta/2}}{\sqrt{\pi}} \left|\Gamma\left(|l|+\frac{1}{2}+i\eta\right)\right| \frac{(-2i\rho)^{|l|}}{(2|l|)!} e^{i\rho} e^{i\sigma_{|l|}} \\ \times {}_1F_1\left(|l|+\frac{1}{2}+i\eta, 2|l|+1, -2i\rho\right) \frac{e^{il(\phi_r-\phi_k)}}{2\pi},\end{aligned} \tag{3.8}$$

where ${}_1F_1$ is the confluent hypergeometric function. Here, $\boldsymbol{k}$ and $\boldsymbol{r}$ represent either the relative or COM momentum and displacement of two charged particles in two dimensions with k, r, ϕ_k, and ϕ_r being their magnitudes and phases, respectively. $\eta = \mu Z_1 Z_2/k$, where μ is the reduced mass of the two particles (1/2 in the case of V_{ee} and 2 in the case of V_{eN}) and Z_1 and Z_2 are their charges (-1 and -1 in the case of V_{ee} and -2 and 2 in the case of V_{eN}), $\rho = kr$, and $\sigma_{|l|} = \arg\Gamma(|l|+\frac{1}{2}+i\eta)$ is the two-dimensional Coulomb phase. Alternatively, we also expressed the two-dimensional scattering wave function in terms of the three-dimensional Coulomb wave function F_l,

$$\psi(\boldsymbol{k},\boldsymbol{r}) = \sum_{l=-\infty}^{\infty} \sqrt{\frac{2}{\pi\rho}} (-i)^{|l|} e^{i\sigma_{|l|}} F_{|l|-\frac{1}{2}}(\eta,\rho) \frac{e^{il(\phi_r-\phi_k)}}{2\pi}, \tag{3.9}$$

which enables us to use available packages like GNU Scientific Library (GSL) for the calculation. In the practical computations we truncated the sum over l to $l_{\max} = 12$ for ψ_{ee} and $l_{\max} = 16$ for ψ_{eN}. While we found that the results for the angular momentum distributions presented below are converged for projection to ψ_{ee}, the momentum-space wave function for projection onto ψ_{eN}

Table 3.1. Double ionization probabilities for the different momentum-space wave functions

R	5.6	10
ψ_{plane}	3.5520×10^{-5}	1.9182×10^{-5}
ψ_{ee}	3.4636×10^{-5}	1.7428×10^{-5}
ψ_{eN}	1.0908×10^{-5}	6.8121×10^{-6}

was not fully converged. However, we checked that our qualitative conclusions below are correct. We attribute the difficulty in the convergence to the fact that we used a monomer Coulomb wave function for a two-center problem in ψ_{eN} and that the residual potential is not purely $1/r$. The degree of convergence can indeed be estimated by comparing the double ionization probabilities obtained for the corresponding momentum-space wave function in each case, given in Tab. 3.1. Evidently, the probabilities of the momentum-space wave functions obtained by projection onto ψ_{plane} and onto ψ_{ee} agree rather well with each other, while the result for the projection onto ψ_{eN} indicates the lack of convergence with respect to $l_{\max}$.

In Fig. 3.3 we compare results for the molecular-frame angular distributions of one of the two electrons in the double photoionization after projections onto ψ_{plane} [panels (a) and (b)], onto ψ_{ee} [panels (c) and (d)], and onto ψ_{eN} [panels (e) and (f)]. The distributions are integrated over the emission angle of the other electron and the energies of the electrons. The theoretical data are shown in each set as a function of the emission angle of the electron. In order to compare with recently obtained experimental data [89], the theoretical results are averaged over the orientation of the dimer axis and weighted with respect to singlet and triplet state contributions according to the multiplicities of the states. Furthermore, due to the short duration of the pulse used in the simulations, the calculated distributions show a slight left-right asymmetry along the polarization direction. We have removed this asymmetry by taking the mean of the original result and its mirror image with respect the plane perpendicular to the polarization axis through the center of mass of the two nuclei. Finally, the theoretical results are matched to coincide with the experimental data at the maximum of the distributions. Note that the experimental results are integrated over $R = 5.1 \sim 6.8$ a.u. in panels (a), (c), and (e), and $R = 9.4 \sim 10.9$ a.u. in panels (b), (d),

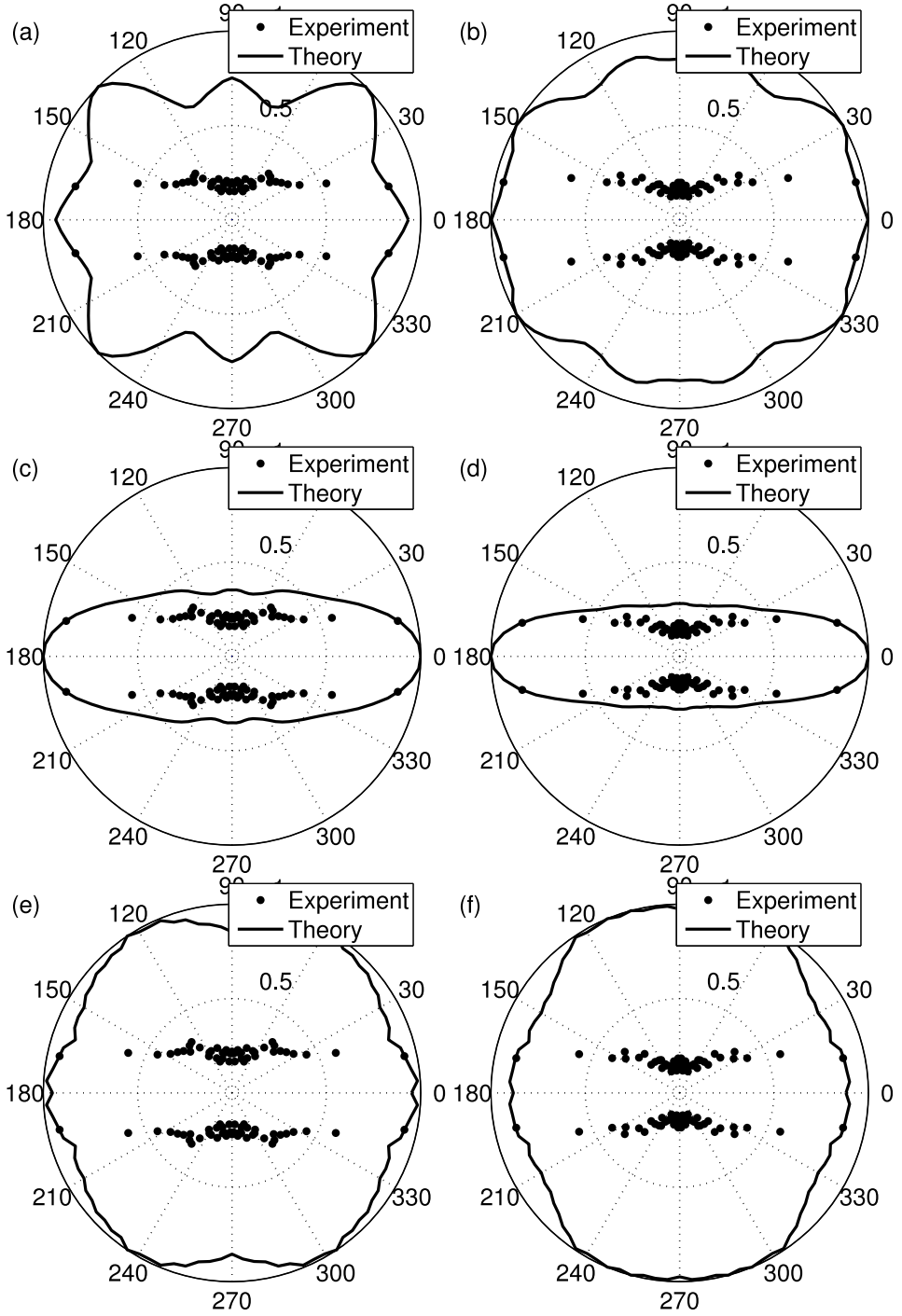

Figure 3.3. Molecular-frame angular distributions of one of the two electrons following double photoionization of the helium dimer, obtained by projection of the respective part of the wave function onto different approximate final two-electron states at $R = 5.6$ a.u. (left column) and $R = 10$ a.u. (right column). Shown is a comparison between the theoretical results (solid lines) and the experimental data (solid circles). For the theoretical results in panels (a) and (b), ψ_{plane} is used as the approximate final two-electron state, while for the results in panels (c) and (d), ψ_{ee}, and for those in panels (e) and (f), ψ_{eN} is used.

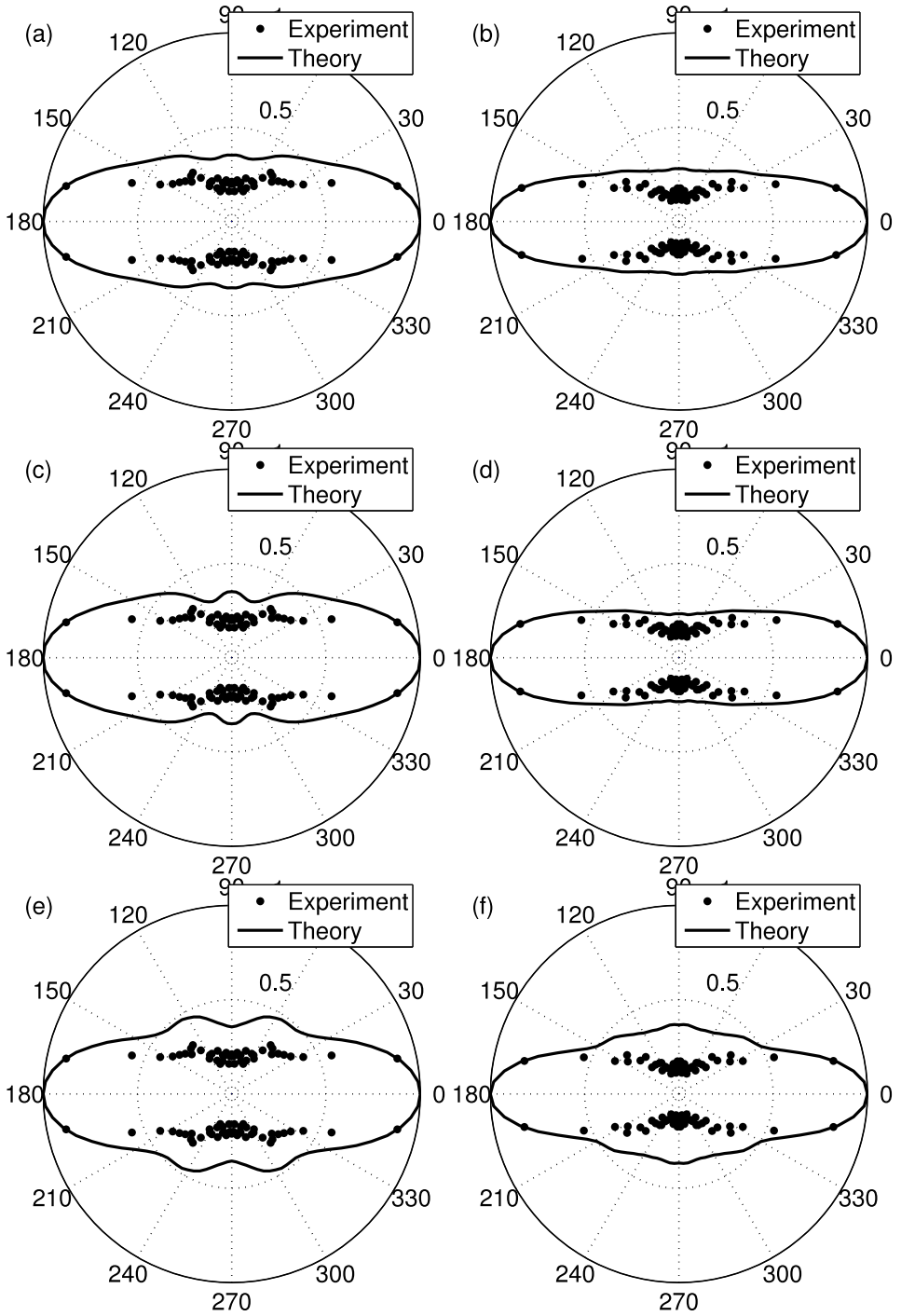

Figure 3.4. Molecular-frame angular distributions of one of the two electrons following double photoionization of the helium dimer, obtained by projection of the respective part of the wave function onto ψ_{ee} at $R = 5.6$ a.u. (left column) and $R = 10$ a.u. (right column). Shown is a comparison between the theoretical results (solid lines) and the experimental data (solid circles). For the theoretical results in panels (a) and (b), full results are shown, while for the results in panels (c) and (d), singlet contributions, and for those in panels (e) and (f), triplet contributions are shown.

and (f) (subset of data shown in Fig. 3(b) of Ref. [89]). The comparison shows that within the present model the approximation of the final-state wave function as product of a plane wave in the COM coordinates and a Coulomb wave in the relative coordinates qualitatively appears to be the most appropriate one of the three considered options. We therefore use $\psi_{\rm ee}$ to obtain angular distributions for the remainder of our studies. In order to show the individual contributions from singlet and triplet initial states, we further show in Fig. 3.4 the same angular distributions obtained by projection onto $\psi_{\rm ee}$ but from singlet and triplet states separately.

3.4 The knockout mechanism

On the basis of the comparison presented in Figs. 3.3 and 3.4, we proceed to obtain insights into the mechanism of the correlated electron emission from the helium dimer. As mentioned above, it was argued based on the experimental data and a comparison with theoretical results from electron-impact ionization that the double photoionization proceeds via a knockout-type mechanism. According to this mechanism the double ionization probability should be closely related to the probability that the primary photoelectron, launched at one helium atom, "hits" the second electron which is localized at the neighboring atom. The results in Figs. 3.5 and 3.6 confirm this close relation based on our theoretical data, which provides strong evidences for the knockout mechanism.

First, we compare in Fig. 3.5(b) the probability of double photoionization as a function of the orientation of the dimer axis with respect to the polarization direction of the field (solid line) with the experimental data (solid circles [89]) and a $\cos^2\delta$-distribution (dash-dotted line). The comparison shows not only an excellent agreement between theoretical predictions and experimental data but moreover indicates a close relation between the double ionization probability and the direction of the primary photoelectron momentum. The latter is close to the expected p-wave (or $\cos^2$-) distribution as can be seen from the theoretical results in panel (a) for orientation of dimer axis parallel (red solid line) as well as perpendicular (blue dashed line) to the polarization direction of the field. The small deviation from the $\cos^2$-distribution in the case of parallel orientation

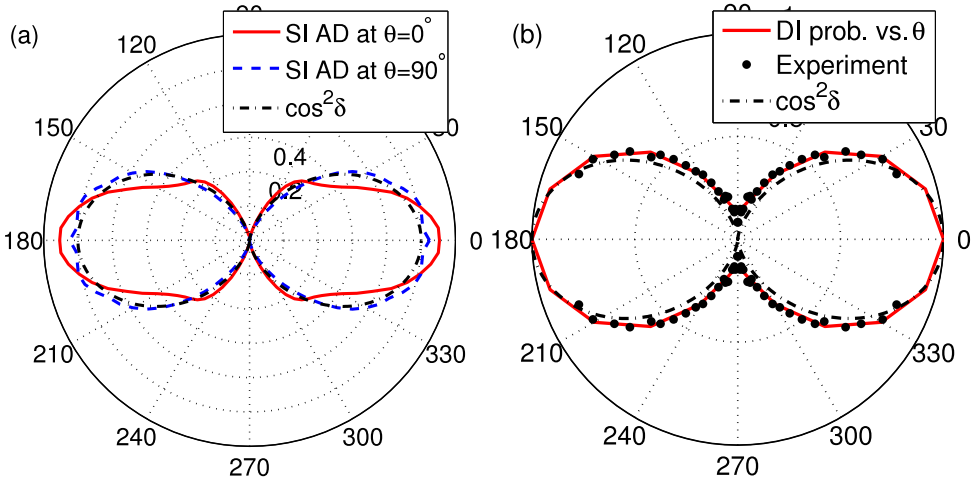

Figure 3.5. Comparison of the lab-frame dipole-transition angular distribution $\cos^2\delta$ (dashed-dotted line) with (a) the theoretical photoelectron angular distributions (AD) for single ionization (SI) of the dimer oriented either parallel (red solid line) or perpendicular (blue dashed line) to the polarization axis and (b) the probability of double photoionization (DI) as a function of the orientation of the dimer axis (theoretical prediction: red solid line, experimental data: solid circles, integrated over $R = 4.5 \sim 6.8$ a.u. (subset of data shown in Fig. 3(a) of Ref. [89])). The polarization direction of the field is along the horizontal axis in both panels. The internuclear distance was chosen to be $R = 5.6$ a.u. and the parameters of the XUV field are the same as in Fig. 3.4.

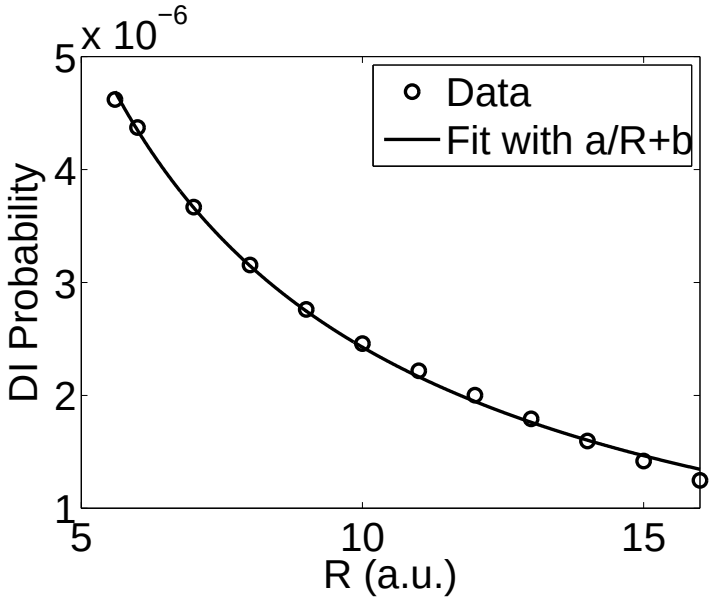

Figure 3.6. Double photoionization probability (open circles) as a function of internuclear distance R for orientation of the dimer axis parallel to the polarization direction of the field. It scales as $1/R$ with the internuclear distance. The fitting parameters are $a = 2.88 \times 10^{-5}$ and $b = -4.56 \times 10^{-7}$. The parameters of the XUV field are the same as in Fig. 3.4.

indicates the effect of elastic scattering of the photoelectron at the second atom in the single ionization data, in agreement with similar observations for the neon dimer [95].

Further evidence for the knockout mechanism is given by the dependence of the double photoionization probability on the internuclear distance R. For the knockout mechanism, the probability of the primary photoelectron "hitting" the second electron that produces double ionization is expected to decrease with an increase of R, since the wavepacket representing the primary photoelectron expands in space. Our theoretical results for the double photoionization probability, shown in Fig. 3.6, indeed follow closely the expected $1/R$ trend for the case of parallel orientation of the dimer axis in our planar model. We may emphasize that in the real 3D helium dimer we expect an even stronger $1/R^2$ decrease. We may further note that the double-to-single ionization ratio follows the same trend as the double photoionization probability.

Moreover, our time-dependent simulations provide a "movie" of the scattering process as a function of time. During the knockout process, it is expected that one of the electrons approaches the other after the initial absorption of the photon. This can be visualized via the temporal evolution of the two-electron probability distribution as a function of the relative coordinate $z = z_1 - z_2$ along the polarization direction. The respective results of our numerical simulations for an internuclear distance of 15 a.u. are shown in Fig. 3.7. The initial state probability distribution, localized at the two nuclei, has been subtracted in order to enhance the visibility of the small contributions leading to single and double ionization. The results for the temporal evolution starting from the ground state (singlet, panel (a)), and the first excited state (triplet, panel (b)) confirm our previous conclusions regarding the knockout mechanism. The exchange-asymmetry in the wave function of the triplet state illustrates itself as a minimum at $z = 0$, which is particularly apparent when the two electrons are close to each other. Due to the integration over x_1 and x_2, we observe a minimum in the distributions instead of a node, which would show up at fixed transverse distances.

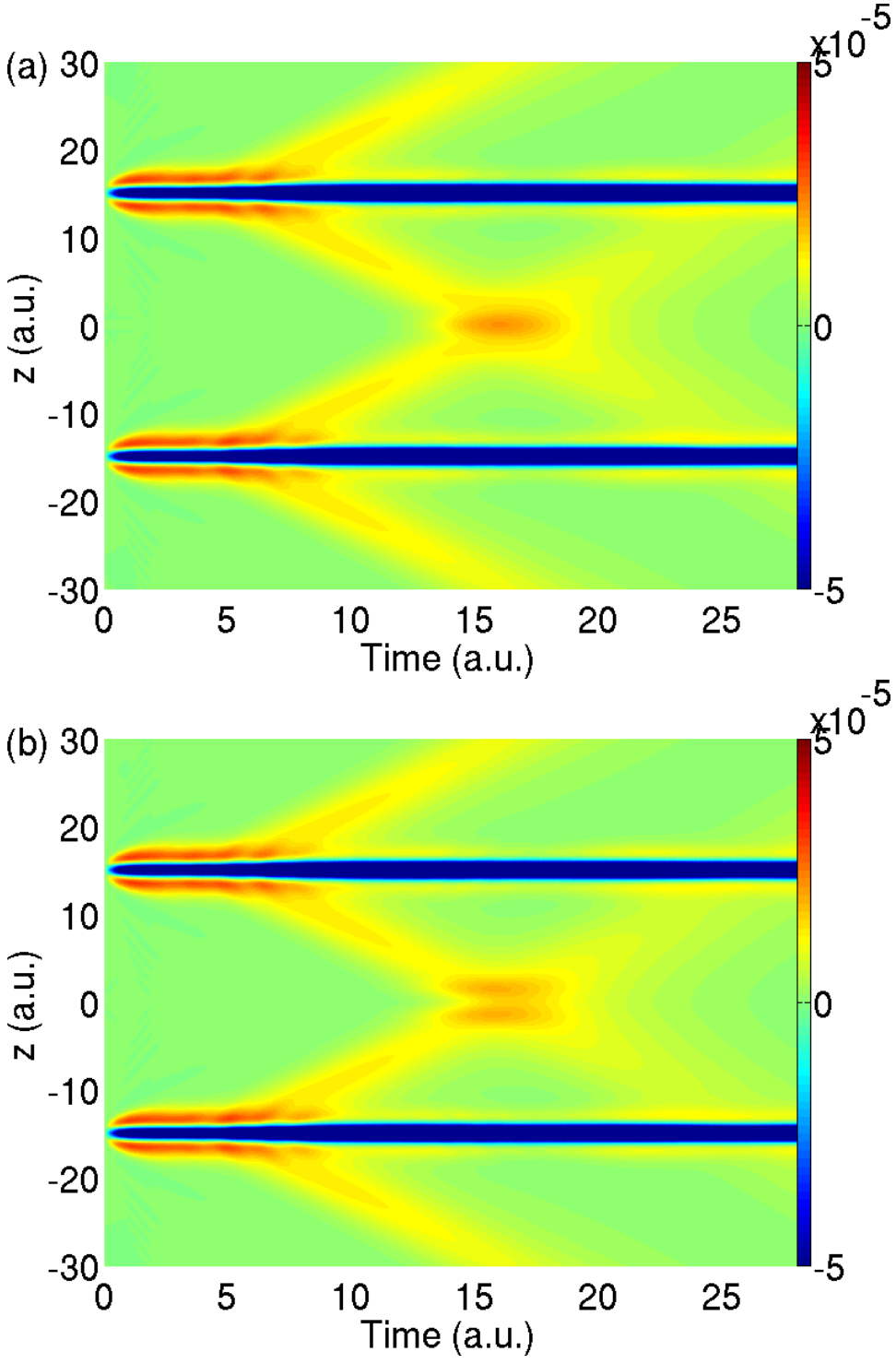

Figure 3.7. Temporal evolution of the two-electron probability distribution of the helium dimer in $z = z_1 - z_2$ starting from the ground state [singlet, panel (a)] and the first excited state [triplet, panel (b)], which exhibit the differences between singlet and triplet scattering. In the simulation, the dimer axis is oriented parallel to the polarization axis.

3.5 The Hamiltonian reduction method

In this section, we consider abridged Hamiltonians and study the Coulomb interactions between the electrons and the nuclei in the helium dimer by comparing the angular distributions obtained using the abridged Hamiltonian to those obtained with the full Hamiltonian. To this end, we first briefly discuss the numerical model used, which just restricts the orientation of the dimer in the planar 4D model in Sec. 3.2 to be parallel to the laser field, since the scattering effects in single and double photoionization are strongest in the parallel orientation case. We then introduce and discuss different abridged Hamiltonians in which certain interactions are removed from the full Hamiltonian. A comparison between the ground states of the full and the abridged Hamiltonians will be given and discussed. Next, we apply the different Hamiltonians in numerical simulations to study scattering effects of the photoelectron in single photoionization. Afterwards, we compare angular distributions of the primary and knockout electron as well as to study the role of Coulomb interactions in the double photoionization process.

3.5.1 Theory

In this section we outline the four-dimensional model Hamiltonian used for the helium dimer in the simulations, which is a restriction of the planar 4D model of the helium dimer in Sec. 3.2 to the z direction. We then present options to restrict the full model Hamiltonian in numerical simulations in order to label the electrons and analyze the effect of certain interactions on the single and double photoionization processes.

As shown in Fig. 3.8, we use the planar 4D model of the helium dimer in Sec. 3.2 but restrict the orientation of the dimer axis to be parallel to the laser polarization direction, or the z direction, unless explicitly stated otherwise. In this scheme, nucleus 1 (N_1) is located at the right side and nucleus 2 (N_2) is located at the left side. Here we restrict the orientation of the dimer axis to be parallel to the laser field since the scattering effects in single and double photoionization are

strongest in this case. The full Hamiltonian of the system is given by

$$\begin{aligned} H =& \frac{p_{x_1}^2 + p_{z_1}^2}{2} + \frac{p_{x_2}^2 + p_{z_2}^2}{2} + E(t)\,(z_1 + z_2) \\ &+ V_{\mathrm{SAE}}(r_{11}) + V_{\mathrm{SAE}}(r_{12}) + V_{\mathrm{SAE}}(r_{21}) + V_{\mathrm{SAE}}(r_{22}) \\ &+ \frac{1}{\sqrt{(x_1 - x_2)^2 + (z_1 - z_2)^2 + b^2}} + \frac{1}{R}, \end{aligned} \tag{3.10}$$

where

$$r_{ij} = \sqrt{x_i^2 + \left[z_i + (-1)^j \frac{R}{2}\right]^2 + a^2}. \tag{3.11}$$

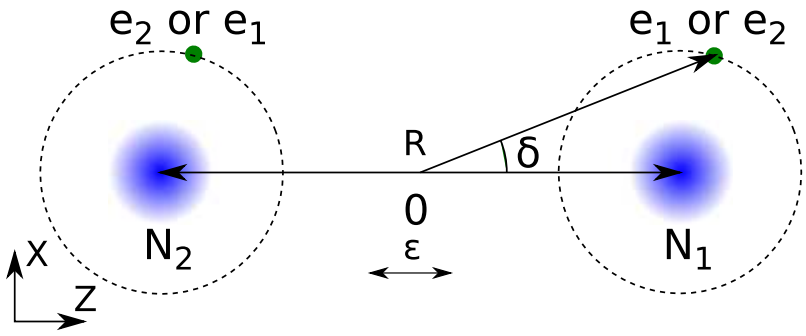

Figure 3.8. Scheme of the numerical model for the helium dimer in the case of parallel orientation. One electron at each atom is considered to be active and restricted to the same plane, with coordinates (x_1, z_1) and (x_2, z_2), respectively. The internuclear distance R and the dimer axis are fixed in space. The dimer axis is chosen parallel to the laser polarization direction ε during the simulations, unless explicitly stated otherwise.

For further analysis we used abridged Hamiltonians in test simulations, in which certain interaction terms are removed from the full model Hamiltonian, Eqn. (3.10). One goal to use these reductions was to distinguish the primary electron, which first interacts with the light field, from the secondary electron by labeling the two electrons. This can be done by removing the term $E(t)z_2$ from the full Hamiltonian, which gives

$$\begin{aligned} H_{\mathrm{E1}} =& \frac{p_{x_1}^2 + p_{z_1}^2}{2} + \frac{p_{x_2}^2 + p_{z_2}^2}{2} + E(t) z_1 \\ &+ V_{\mathrm{SAE}}(r_{11}) + V_{\mathrm{SAE}}(r_{12}) + V_{\mathrm{SAE}}(r_{21}) + V_{\mathrm{SAE}}(r_{22}) \\ &+ \frac{1}{\sqrt{(x_1 - x_2)^2 + (z_1 - z_2)^2 + b^2}} + \frac{1}{R}. \end{aligned} \tag{3.12}$$

In the corresponding test simulations we can then identify electron 1 as the primary and electron 2 as the secondary or knockout electron in double photoionization and, thus, compare the angular distributions for these electrons.

The present model of the helium dimer further facilitates the analysis of dynamical effects due to the interactions between electrons and nuclei. As mentioned above, the two electrons are initially predominantly located at different atoms in the dimer. This can be also seen from the spatial distributions of the lowest energy eigenstates of the planar helium dimer model, which are shown in Fig. 3.9 for an internuclear separation of $R = 5.6$ a.u. corresponding to the minimum of the helium dimer potential [91]. These energy eigenstates were obtained via imaginary time propagation. The spatial distributions are shown as functions of z_1 and z_2 and are integrated over the other coordinates. The ground state [panel (a)] is a singlet state, while the first excited state [panel (b)] is a triplet state.

Due to the large internuclear distance, the interaction of each electron with the distant nucleus in the initial dimer state is rather small. Hence, in two further abridged Hamiltonians, we neglected first the interaction of electron 2 with nucleus 1, $V_{\mathrm{SAE}}(r_{21})$, to get

$$\begin{aligned} H_{\mathrm{E1,local1}} =& \frac{p_{x_1}^2 + p_{z_1}^2}{2} + \frac{p_{x_2}^2 + p_{z_2}^2}{2} + E(t) z_1 \\ &+ V_{\mathrm{SAE}}(r_{11}) + V_{\mathrm{SAE}}(r_{12}) + V_{\mathrm{SAE}}(r_{22}) \\ &+ \frac{1}{\sqrt{(x_1 - x_2)^2 + (z_1 - z_2)^2 + b^2}} + \frac{1}{R}, \end{aligned} \tag{3.13}$$

and then $V_{\mathrm{SAE}}(r_{21})$ as well as $V_{\mathrm{SAE}}(r_{12})$ to get

$$\begin{aligned} H_{\mathrm{E1,local2}} =& \frac{p_{x_1}^2 + p_{z_1}^2}{2} + \frac{p_{x_2}^2 + p_{z_2}^2}{2} + E(t) z_1 \\ &+ V_{\mathrm{SAE}}(r_{11}) + V_{\mathrm{SAE}}(r_{22}) \\ &+ \frac{1}{\sqrt{(x_1 - x_2)^2 + (z_1 - z_2)^2 + b^2}} + \frac{1}{R}. \end{aligned} \tag{3.14}$$

In the first of the two Hamiltonians, $H_{\mathrm{E1,local1}}$, the symmetry of the electron-nucleus interactions is removed and, therefore, the electrons are localized at one of the two nuclei, i.e., electron 1 at nucleus 1 and electron 2 at nucleus 2, as can be seen from the ground state distribution shown

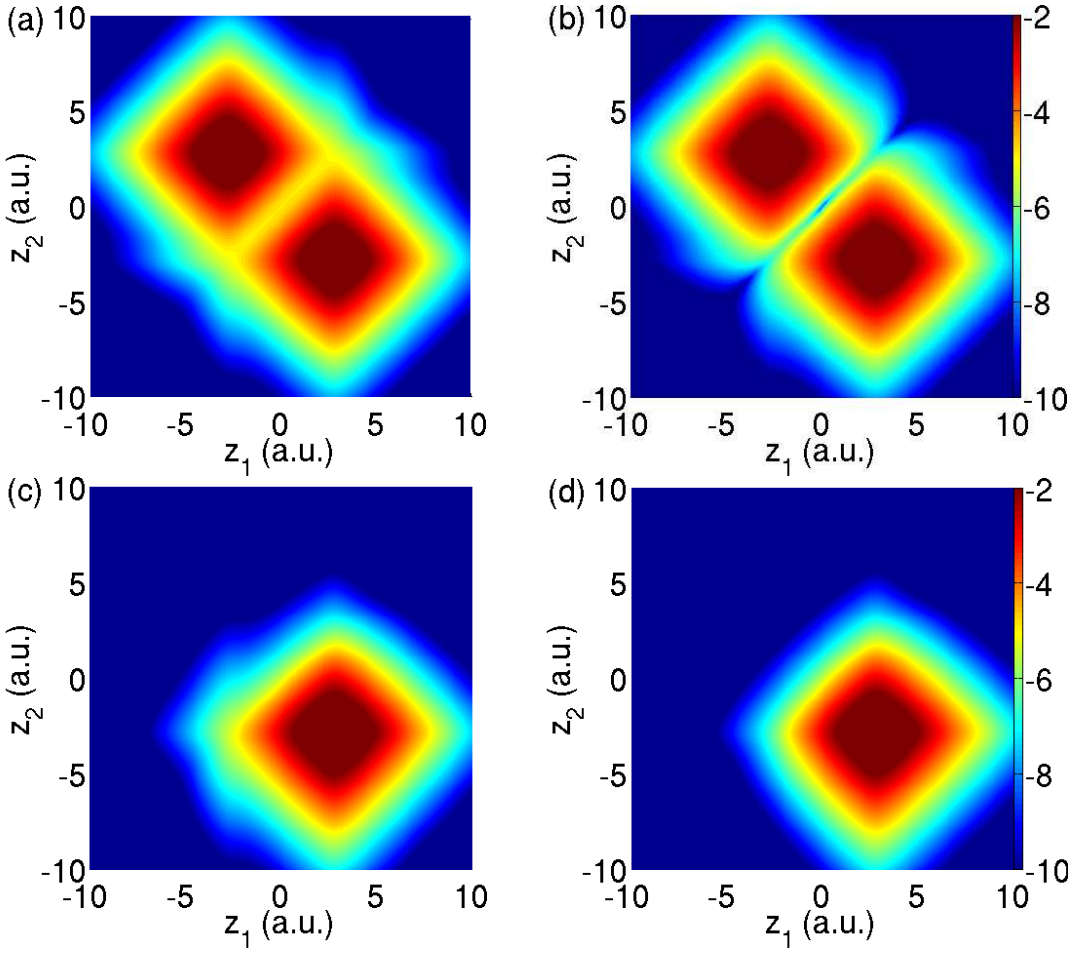

Figure 3.9. Spatial distributions (on a logarithmic scale) of the ground state [panel (a)] and first excited state [panel (b)] of the planar model helium dimer with full model Hamiltonian and that of the ground states of the planar model helium dimer with abridged Hamiltonians, $H_{\mathrm{E1,local1}}$ [Eqn. (3.13), panel (c)] and $H_{\mathrm{E1,local2}}$ [Eqn. (3.14), panel (d)]. The distributions are integrated over x_1 and x_2 and shown as functions of z_1 and z_2.

in Fig. 3.2(c). We note that in this Hamiltonian all the interactions of the primary electron, i.e., electron 1, which interacts with the light field, are retained. On the other hand, in $H_{\mathrm{E1,local2}}$ the interaction of the primary electron with the second nucleus (nucleus 2) is removed as well and the corresponding initial state is represented in Fig. 3.2(d). As we will show below, comparison of the results from the simulations with the different Hamiltonians enables us to study, e.g., the scattering of the primary electron at the second nucleus (nucleus 2) in the photoelectron angular distributions.

We note that due to the localization of the electrons at either one of the nuclei, the corresponding ground states are no longer symmetric regarding to the exchange of electrons and the terminology of singlet and triplet states does not apply to the states of the two abridged Hamiltonians. The difference between the ground states of the full and the two abridged Hamiltonians can be quantified via their overlaps as:

$$|\langle\psi_{\mathrm{E1,local1}}|\psi_{\mathrm{full}}^{\mathrm{singlet}}\rangle|^2 = 0.499562; \tag{3.15}$$

$$|\langle\psi_{\mathrm{E1,local1}}|\psi_{\mathrm{full}}^{\mathrm{triplet}}\rangle|^2 = 0.499251; \tag{3.16}$$

$$|\langle\psi_{\mathrm{E1,local2}}|\psi_{\mathrm{full}}^{\mathrm{singlet}}\rangle|^2 = 0.498898; \tag{3.17}$$

$$|\langle\psi_{\mathrm{E1,local2}}|\psi_{\mathrm{full}}^{\mathrm{triplet}}\rangle|^2 = 0.498805. \tag{3.18}$$

All overlaps are close to 0.5, indicating the small effect of the interaction between an electron, localized at one atom in the dimer, and the distant nucleus in the initial state. The value of 0.5 instead of 1.0 arises due to the localization of each electron at one of the two nuclei in the abridged Hamiltonians.

3.5.2 Single ionization

In this section, we use the model Hamiltonians to study scattering effects in single photoionization of the dimer, or more precisely, the dynamical effects of the photoelectron that is emitted at one of the atoms and then scattered at the other atom in the dimer. To this end, we obtained the photoelectron angular distributions by taking a Fourier transform of the contributions to the wave function that were identified as single ionization in the numerical simulations. From the re-

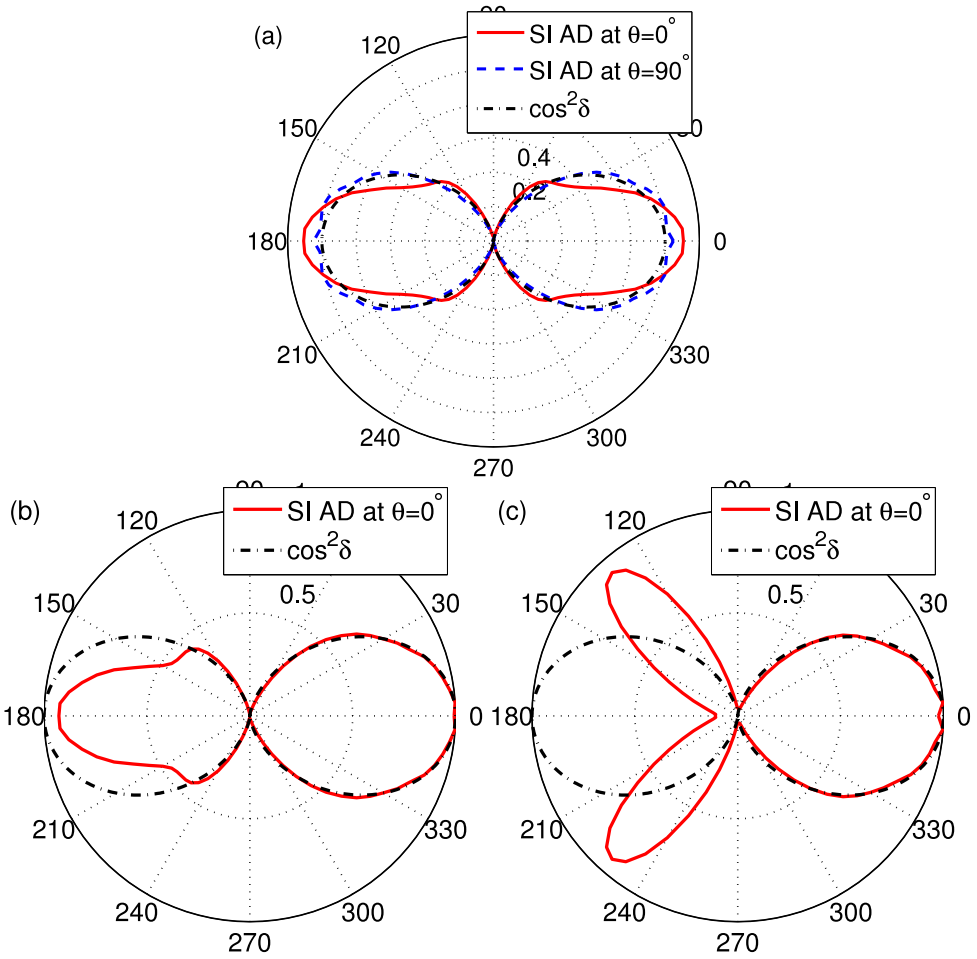

Figure 3.10. Comparison of photoelectron angular distributions in single ionization of the helium dimer using the full [panel (a)] and abridged Hamiltonians, $H_{\mathrm{E1,local1}}$ [Eqn. (3.13), panel (b)] and $H_{\mathrm{E1,local2}}$ [Eqn. (3.14), panel (c)]. Results represented by solid lines are obtained for parallel orientation of the dimer axis with respect to the polarization direction of the field, which is chosen along the horizontal axis. For the full simulations [panel (a)] also shown is the distribution obtained for perpendicular orientation ($\theta = 90°$, blue dashed line) of the dimer axis and for all simulations the distributions are compared to the expected $\cos^2$-distribution (dash-dotted lines). For the sake of comparison, the distributions in panel (a) are scaled such that their areas match, while in panels (b) and (c) the distributions are matched at one point. In all simulations a 4-cycle 20 nm XUV laser pulse with a peak intensity of 1×10^{14} W/cm^2 has been used.

sults for the full model Hamiltonian, shown in Fig. 3.10(a), we see, as pointed out earlier, that the photoelectron angular distributions depend on the orientation of the dimer axis with respect to the polarization direction of the laser. For an orientation perpendicular to the polarization axis, the distribution (dashed line) is close to the expected p-wave distribution ($\cos^2$, dash-dotted line) for single-photon absorption from a s-state. On the other hand, for parallel orientation we observe a deviation from the $\cos^2$-distribution, and the angular distribution appears to be narrower around the polarization direction with two small wings in the region between 30° and 60° with respect to the polarization axis. These deviations in the distributions were previously interpreted as an indication for the scattering of the photoelectron at the other atom in the dimer.

To shed further light on this interpretation, we present in the other panels of Fig. 3.10 results obtained with the abridged Hamiltonians, $H_{\mathrm{E1,local1}}$ [Eqn. (3.13), panel (b)] and $H_{\mathrm{E1,local2}}$ [Eqn. (3.14), panel (c)], for orientation of the dimer parallel to the polarization direction. In both set of simulations only one of the two electrons, namely electron 1, interacted with the field and, moreover, this active electron 1 was located at nucleus 1, which is the nucleus located on the right in the present figures. In this configuration we can compare photoemission with (emission to the left) and without (emission to the right) scattering at the second atom, which is located to the left of the initial position of the active electron. The result in panel (b), in which all Coulomb interactions of the active electron with the other electron and the nuclei are taken into account, confirm that the nonscattered angular distribution is close to the $\cos^2$-distribution (dash-dotted line), while the scattered angular distribution shows the deviation observed in the full simulations. This demonstrates the effect of scattering on the photoelectron angular distribution. We note that the small deviations between the numerical results and the $\cos^2$-distributions in the right part of the lobe, most notably in the kink along the polarization direction in Fig. 3(c), reflect the numerical errors in the present calculations.

We can even further distinguish between the effect of electron-electron and electron-ion scattering. This can be done by comparing the results in panels (b) and (c) of Fig. 3.10. In the latter simulations we deliberately neglected the interaction between the active electron and the second

nucleus, i.e., the nucleus on the left. The comparison shows that the angular distribution for the scattered photoelectron changes. Emission of the electron along the polarization direction is now strongly suppressed, while there are two maxima at an angle of about 40° with respect to the polarization axis. Thus, we can conclude that it is the electron-electron scattering which gives rise to the two wings in the full distribution. On the other hand, the electron-nucleus (or electron-ion) scattering causes, due to the attractive nature of the interaction, a narrowing (or focusing) to the angular distribution along the polarization direction.

3.5.3 Double ionization

In this section we analyze the results of simulations using the full and abridged Hamiltonians to study the correlated electron emission from the model dimer. To this end, we first investigate the projection onto different approximate two-electron wave functions to obtain the photoelectron angular distributions. We then proceed to compare the angular distributions of the primary and the knockout electrons.

In previous studies it has been found [89] that the double photoionization of the helium dimer proceeds via the so-called knockout mechanism for low photon energies. According to this mechanism, first the primary electron gets ionized after interaction with the field and then shares its energy via collisional impact ionization with the second knockout electron. As mentioned above we can distinguish between the two electrons by restricting the electron-field interaction to one of the two electrons and locating the electrons at one of the atoms in the dimer.

In Fig. 3.11 we present results of simulations with the different abridged model Hamiltonians, Eqns. (3.13) and (3.14). In the panels in the left column the angular distributions of the primary electron, i.e., the electron interacting with the field, are presented, while in the right column those of the knockout electron are shown. In all cases the dimer was oriented along the polarization axis, which is the horizontal axis in each of the panels. We have integrated the distributions over the emission angle of the other electron and the energies of the two electrons.

Due to the location of the electrons in our models we can study the emission direction of the

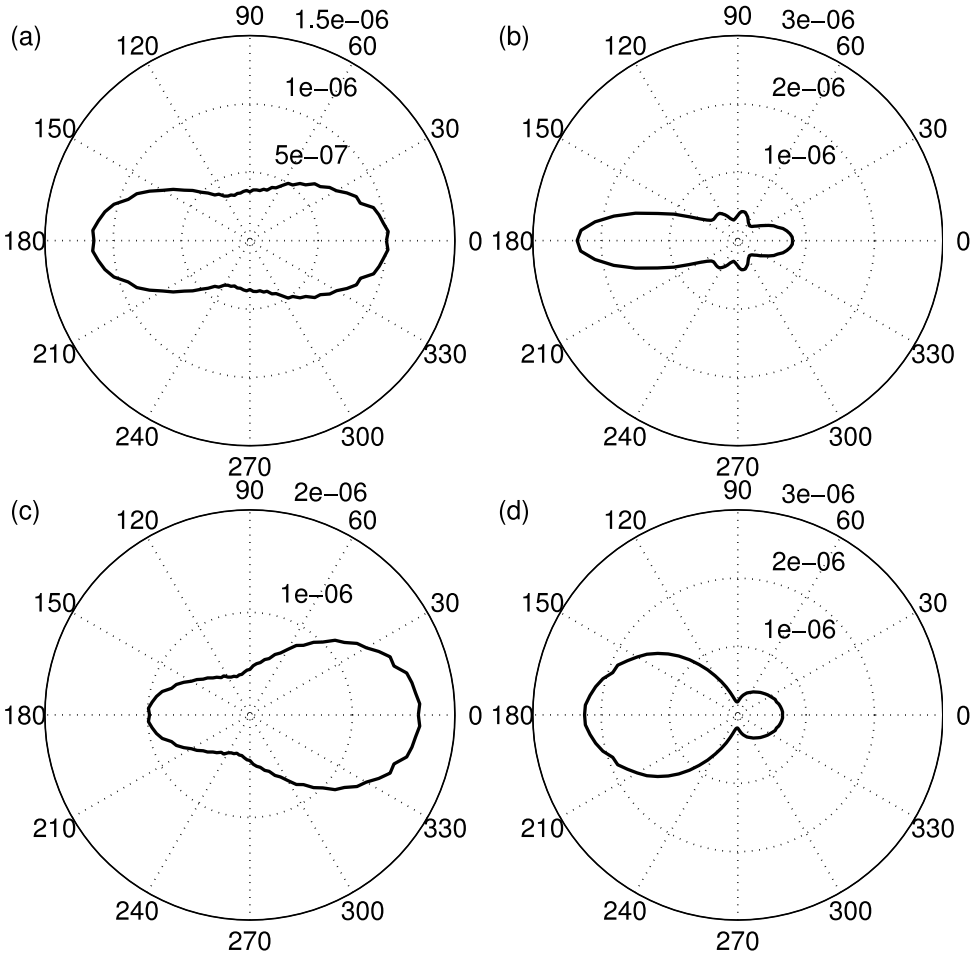

Figure 3.11. Angular distributions of the primary (left column) and knockout electron (right column) in double photoionization of the helium dimer. Results from simulation with different abridged Hamiltonians are compared: panels (a) and (b) correspond to $H_{\mathrm{E1,local1}}$ [Eqn. (3.13)] and panels (c) and (d) correspond to $H_{\mathrm{E1,local2}}$ [Eqn. (3.14)]. In each of the simulations, a 4-cycle 20 nm XUV laser pulse with a peak intensity of 1×10^{14} W/cm^2 and parallel orientation of the dimer axis with respect to the polarization direction of the field (along the horizontal axis of the figure) was considered.

electrons with respect to their initial location in the dimer as well as the role of electron-nucleus and electron-electron interaction during the impact ionization. The result in Fig. 3.11(a), obtained using $H_{\mathrm{E1,local1}}$ [Eqn. (3.13)], in which all interactions of the primary electron are retained, shows that the primary electron is scattered both in forward and backward direction with respect to the propagation direction (from right to left in the figure) after absorption of the photon. Further restriction by suppression of the electron-nucleus scattering in the energy transfer process, $H_{\mathrm{E1,local2}}$ [Eqn. (3.14)], reveals that the electron-electron scattering favors backward scattering of the primary electron, as expected in a head-on collision from a repulsive center [Fig. 3.11(c)].

On the other hand the knockout electron is predominantly ionized along the momentum direction of the incoming primary electron in the impact ionization process, c.f., Fig. 3.11(b) and Fig. 3.11(d). The contribution from the electron-electron interaction leads to a rather broad angular distribution with respect to the molecular axis [Fig. 3.11(d)], in agreement with a similar distribution of the primary electron in the opposite direction [Fig. 3.11(c)]. The inclusion of the electron-nuclear contribution leads to a distribution which is more aligned along the polarization direction [Fig. 3.11(b)].

Finally, we obtained the angular distributions of the knockout electron when the primary electron is fixed along certain emission directions. For the results presented in Fig. 3.12, we considered emission of the primary electron either in backward (with respect to the impact direction, panels on the left) or forward direction (panels on the right), using abridged Hamiltonians $H_{\mathrm{E1,local1}}$ [Eqn. (3.13), panels (a) and (b)] and $H_{\mathrm{E1,local2}}$ [Eqn. (3.14), panels (c) and (d)]. The distributions show that the two electrons are predominantly emitted back-to-back in particular for backward scattering of the primary electron. As can be seen in the distributions, we observe for backward scattering that inclusion of electron-nucleus interaction leads to a stronger alignment of the distribution along the direction of electron impact [c.f., Fig. 3.12(a) and Fig. 3.12(c)]. On the other hand, for forward direction we see pronounced wings in the angular distributions of the knockout electron when $H_{\mathrm{E1,local1}}$ is used where all interactions of the primary electrons are included [Fig. 3.12(b)].

Similar conclusions hold for other emission angles of the primary electron with respect to

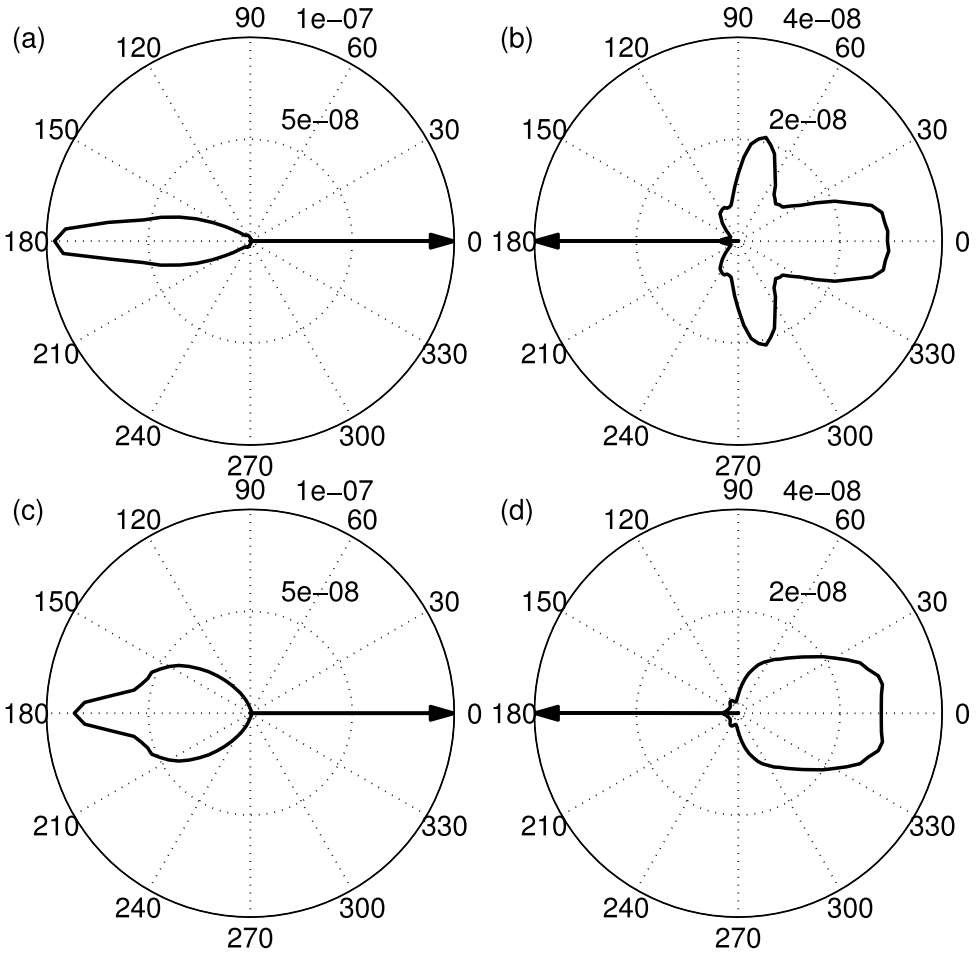

Figure 3.12. Angular distributions of the knockout electron in double photoionization obtained using $H_{\mathrm{E1,local1}}$ [Eqn. (3.13), panels (a) and (b)] and $H_{\mathrm{E1,local2}}$ [Eqn. (3.14), panels (c) and (d)]. The emission of the primary electron is fixed along the direction indicated by the arrow. The field parameters were the same as in Fig. 3.11.

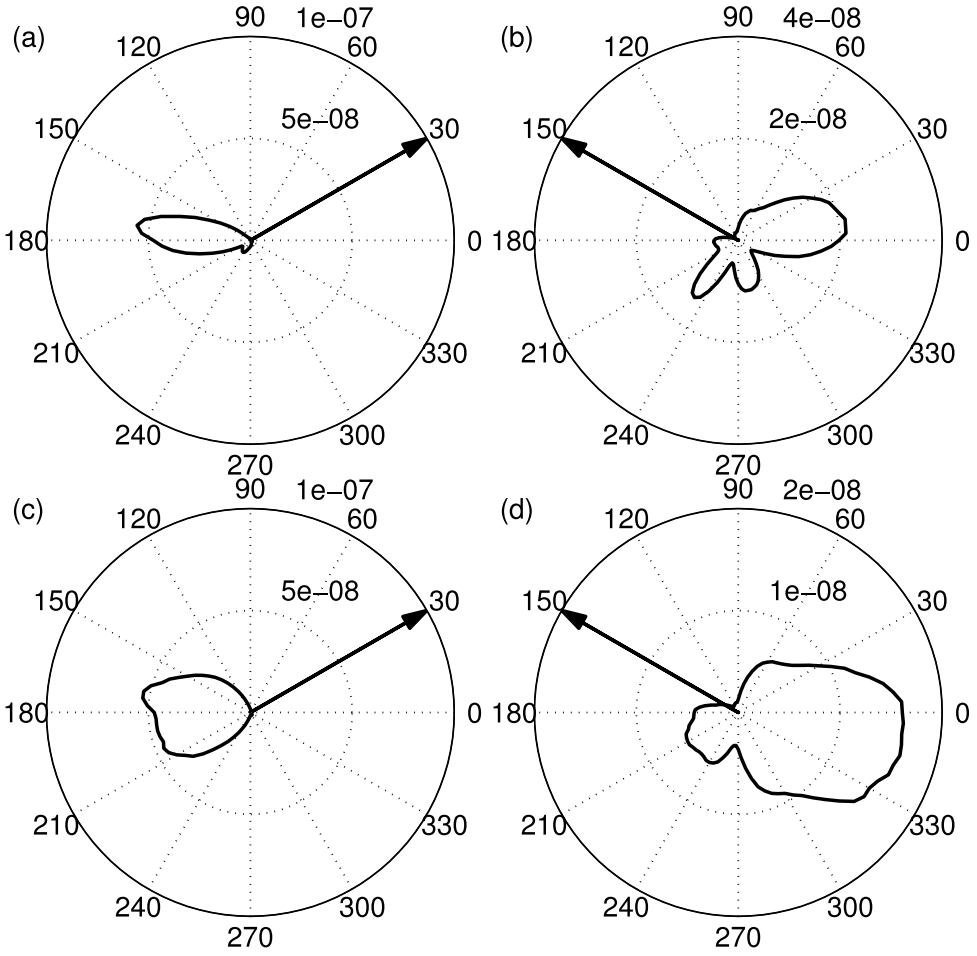

Figure 3.13. Same as Fig. 3.12, but for different emission direction of the primary electron.

the molecular axis and the polarization direction as well, as can be seen from the results presented in Fig. 3.13. In general, we observe that the electrons are predominantly emitted in opposite half planes to the polarization direction. For backward scattering of the primary electron, inclusion of the electron-nucleus interaction leads to a narrower angular distribution of the knockout electron.

3.5.4 Exchange ionization

Using abridged Hamiltonians, we can further study interesting phenomena like the exchange ionization under electron impact. To this end, we use the abridged Hamiltonian H_{E1} [Eqn. (3.12)], in which only electron 1 interacts with the XUV laser pulse. In this scenario, electron 1 is the primary electron during the knockout double photoionization process. In the second step of this process, electron 1 knocks out electron 2 from the other atom. However, it is also possible that electron 1 gets captured by the residual ion from which electron 2 is emitted, a process we denote as exchange ionization.

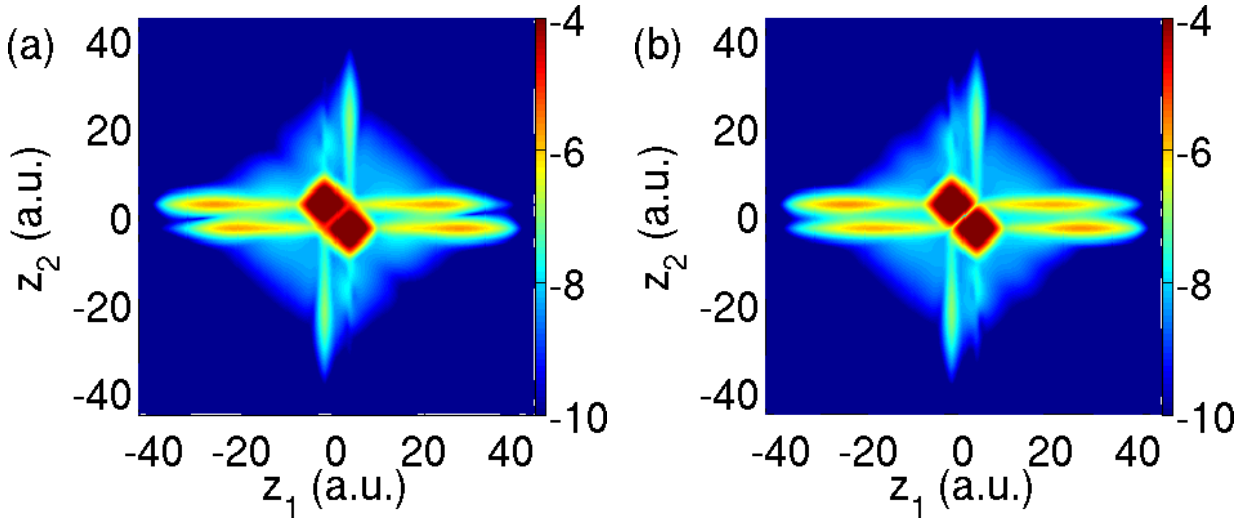

Figure 3.14. Exchange ionization under electron impact for (a) singlet and (b) triplet scattering using the abridged Hamiltonian H_{E1} [Eqn. (3.12)].

The exchange ionization can be clearly seen in Fig. 3.14, which shows a snapshot of the probability density distribution as a function of z_1 and z_2 (integrated over x_1 and x_2) of the helium dimer at $t = 12$ a.u. after interacting with a 4-cycle XUV laser pulse with central wavelength of 20

nm and peak intensity of 1×10^{14} W/cm^2 starting from the (a) singlet and (b) triplet state using the abridged Hamiltonian H_{E1} [Eqn. (3.12)]. As can be seen in the figure, the two intense stripes near $z_2 = 0$ represent the single ionization of electron 1 (primary electron), and the two weaker stripes near $z_1 = 0$ stand for the single ionization of electron 2 (secondary electron). Since only electron 1 interacts with the laser pulse, only it can be ionized in the first step. Thus electron 2 must be knocked out by electron 1 under its impact in the second step, and electron 1 gets captured at the same time since the vertical stripes near $z_1 = 0$ represent single ionization instead of double ionization.

3.6 Summary

In conclusion, we have proposed a planar two-active electron model to analyze the recently observed correlation effects in double photoionization of the helium dimer. Results of numerical simulations for the angular distribution of the electron are found to be in good agreement with the experimental data. Furthermore, theoretical predictions for the double ionization probability as functions of the orientation of the dimer axis as well as the distance of the atoms in the dimer reveal direct evidence for the knockout mechanism, in which the photon energy is transferred over distances of several Angstroms in the dimer to be shared between the electrons. Our conclusions are further supported by an analysis of the temporal evolution of the two-electron probability distribution. An analogue situation to the one discussed here for the helium dimer is encountered in the creation of two-site double core holes of molecules [96, 97] discovered recently. Here the photon is absorbed at one K-shell, e.g., in the C_2H_2 molecule [97]. The two K-shells have almost negligible overlap and their spatial separation is much bigger than the extension of the individual K-shell itself. Hence we expect that the conclusions drawn from our calculations are also valid for the case of single-photon-induced two-site double core hole production.

We have also shown how scattering effects in single and double photoionization of the helium dimer can be studied in *ab-initio* numerical simulations. Due to the large internuclear separation in the dimer, the interaction between the electrons and between each electron and the distant nucleus

in the ground state of the dimer is small. This has enabled us to consider abridged Hamiltonians for the dimer model, in which these interactions are neglected without changing the initial state significantly. Based on the comparison of angular distributions of the primary photoelectron and the secondary knockout electron obtained with different abridged Hamiltonians in numerical simulations, we were able to identify the role of the different Coulomb interactions. For single photoionization our results show that the electron correlation interaction leads to scattering of the photoelectron off the dimer axis, when the latter is oriented along the polarization direction of the field. On the hand the electron-nucleus interaction tends to focus the electron along the polarization direction. In double photoionization the primary photoelectron is scattered both in forward as well as backward direction with respect to its initial momentum direction obtained upon photon absorption. Keeping the direction of the primary electron fixed we then further found that the two electrons are primarily emitted back-to-back in the double photoionization process.

Chapter 4

Selection rules in the few-photon double ionization process[1]

In this chapter, we analyze the selection rules for the emission of two electrons from the helium atom and the helium dimer following the absorption of a few photons in an intense laser field. The rules arise, as generalization of the well-studied one-photon case, due to the symmetries of the accessible final states in the two-electron continuum. We show, in particular, that an increase of the number of absorbed photons leads to alternating suppression and non-suppression of the back-to-back emission of the two electrons with equal energy sharing. Results of numerical simulations using models of the helium atom and the helium dimer are in agreement with the theoretical predictions. We further generalize the selection rules and find that they apply whenever the system has central symmetry with respect to its center of mass.

4.1 Introduction

The evolution of three or more Coulomb-interacting particles in the continuum after the break-up of the atomic or molecular system has been a topic of recurring interest over many years. Despite the complex dynamics of an interacting few-body system, the final-state distributions of the particles often show some general structures. In particular, prominent nodes in the distributions represent restrictions for the correlated momenta of the outgoing particles. These restrictions arise either due to the Coulomb repulsion between the charged particles or due to symmetries (spin, angular momentum, parity, etc.) of the final state of the few-body process. In this respect,

[1] The results of this chapter are in part based on "H. Ni, S. Chen, C. Ruiz, and A. Becker, J. Phys. B **44**, 175601 (2011)" [98].

the break-up of an atomic or molecular system following absorption of a single photon has been studied in detail. Selection rules for the correlated electron momenta arising from the symmetry of the final state have been established for single-photon double ionization of the helium atom [99] and the hydrogen molecule [100], as well as the general case of a N-electron break-up following photoionization of the helium atom [101]. In contrast, the selection rules after absorbing multiple photons have not been studied yet. However, we may expect that the final two-electron states in few-photon double ionization possess a few definite symmetries and that the well-established selection rules in the single-photon case can be applied to the few-photon interactions as well.

In this chapter we study the restrictions to the position and momentum distributions of the emitted electrons in the continuum following the few-photon double ionization of the helium atom and the helium dimer from the ground state. To this end, we first briefly discuss the application of the final-state selection rules, derived by Briggs and co-workers [99–101], to the few-photon double ionization. The selection rules based on the symmetry consideration and the correlated Keldysh–Faisal–Reiss (KFR) theory are discussed as well. We then make use of a model for the interaction of the helium atom [63] and the helium dimer [86] with a laser field to test our expectations in numerical simulations. In our simulations we will, in particular, analyze double ionization pathways in which up to four photons are absorbed simultaneously by the two electrons to overcome the double ionization threshold. Based on these studies, we further generalize the selection rules to arbitrary molecules.

4.2 Selection rules for transitions to two-electron continuum states

The symmetries of a state in the two-electron continuum can lead to nodes in the corresponding configuration space wave function and the correlated momentum distribution [99]. Preparation of a system in an initial state of a given symmetry (e.g., the ground state) as well as the symmetry of the transition operator (e.g., photon absorption) limit the symmetries of the final states that can be accessed in a specific process [100]. If in a transition all accessible final states share one or more symmetries or final states of different symmetries lead to the same nodes, there are zeros in the

differential cross sections of the corresponding process. These selection rules have been accurately studied in the theory of single-photon double ionization of atoms and molecules and reproduced in experiments (for a review, see [51]).

4.2.1 Selection rules based on general studies of the two-electron continuum

In order to identify and apply selection rules for double ionization of the helium atom and the helium dimer by absorption of a few photons, we first briefly review the relevant symmetries of the final states in the two-electron continuum, as discussed by Briggs and co-workers (see Ref. [99, 100] and references therein). For the specification of the nodes in the configuration space wave function and the correlated electron momentum distributions we employ the position vectors $\boldsymbol{r}_1$ and $\boldsymbol{r}_2$ and the momentum vectors $\boldsymbol{k}_1$ and $\boldsymbol{k}_2$ of the two electrons as well as the Jacobi coordinates $\boldsymbol{r}_- = \boldsymbol{r}_1 - \boldsymbol{r}_2$ (relative coordinate) and $\boldsymbol{r}_+ = (\boldsymbol{r}_1 + \boldsymbol{r}_2)/2$ (center-of-mass coordinate) and the corresponding momentum vectors $\boldsymbol{k}_- = (\boldsymbol{k}_1 - \boldsymbol{k}_2)/2$ and $\boldsymbol{k}_+ = \boldsymbol{k}_1 + \boldsymbol{k}_2$. We will consider double ionization from the ground state of the helium atom and the helium dimer in a linearly polarized laser field with polarization axis aligned along the quantization axis of the system, which is chosen to be the z-axis. Furthermore, energies of the photons will be small enough such that the photon absorption can be described by an electric dipole transition. Thus, the quantum numbers $M = 0$ (projection of the total angular momentum to the quantization axis) and $S = 0$ (total spin) do not change in the cases considered here.

For single-photon double ionization from the ground state of the helium atom and the helium dimer, which is of $^1\mathrm{S}^{\mathrm{even}}$ symmetry, the transition into the two-electron continuum leads to exclusive population of the $^1\mathrm{P}^{\mathrm{odd}}$ state. In this case and for linear polarization three selection rules have been identified leading to nodes in the correlated wave function and momentum distribution [99, 100]. We analyze each of these selection rules in view of their application to the absorption of more than one photon by the atom:

(1) There is a node in the two-electron wave function and a corresponding vanishing contribution to the correlated momentum distributions for both $\boldsymbol{r}_1$ and $\boldsymbol{r}_2$ ($\boldsymbol{k}_1$ and $\boldsymbol{k}_2$) perpendicular

to the quantization axis of the system (here, the polarization axis of the field) if the final state is of odd parity. Since in dipole transitions the parity of the state changes, this selection rules applies for absorption of either an even or an odd number of photons from the field depending on the parity of the initial state of the system. Thus, in the case of double ionization from the ground state of helium atom we expect the corresponding node to show up for odd-photon processes.

(2) For final states with even S and odd parity (or odd S and even parity) there appears a node in the configuration space wave function (or momentum distribution) for $\boldsymbol{r}_1 = -\boldsymbol{r}_2$ (or $\boldsymbol{k}_1 = -\boldsymbol{k}_2$), which is equivalent to $\boldsymbol{r}_+ = 0$ (or $\boldsymbol{k}_+ = 0$). Since the total spin quantum number S does not change, while the parity of the state does change in an electric dipole transition, the selection rules applies again either for an even-photon or an odd-photon process depending here on the total spin and the parity of the initial state. For few-photon double ionization from the ground state, the node appears, as in the case of selection rule (1), if the number of absorbed photons is odd.

(3) Another node exists for $r_1 = r_2$ ($k_1 = k_2$) and $\theta_1 = \pi - \theta_2$ for final states with even S, odd L, and odd parity (or odd S, even L, and even parity). Concerning the total spin quantum number and the parity the same considerations as in the case of selection rule (2) apply. Thus, for double ionization from the ground state (even S, even parity and even L) the node is expected to be present for absorption of an odd number of photons.

In summary, these selection rules should lead to alternating suppression and non-suppression of electron emission for certain configurations in the two-electron continuum wave function and momentum distribution as the number of absorbed photons increases beyond one. Our analysis is based on the assumption that the electron-field coupling is perturbative, which is justified for the parameter regime considered in the numerical simulations below [102]. We may however note that similar conclusions have been drawn based on a S-matrix analysis of double ionization of helium atom by simultaneous multiphoton absorption in the nonperturbative intensity and wavelength

regime [103, 104], which will be discussed below. Please note that we have restricted our discussion above to those selection rules, which are relevant for the most significant case of double ionization of helium atom from the ground state in a linearly polarized laser pulse. This case will be considered in the numerical simulations below as well. For an initial state with different symmetry or a different choice of the field polarization, other or further symmetry rules may have to be considered.

4.2.2 Selection rules based on the symmetry of the transition matrix

In the previous section, we outline the selection rules based on the general studies of the two-electron continuum by Briggs and co-workers [99, 100]. Indeed, the selection rules can be well reproduced by studying the symmetry in the transition matrix, which determines the symmetry in the two-electron continuum based on the symmetry in the initial state and the transition matrix itself.

The transition matrix for a one-photon process here can be written as

$$T_1 = \langle \psi_\mathrm{f} | \boldsymbol{E} \cdot (\boldsymbol{r}_1 + \boldsymbol{r}_2) | \psi_\mathrm{i} \rangle, \tag{4.1}$$

where ψ_i is the initial state, ψ_f is the final state, $\boldsymbol{r}_1$ and $\boldsymbol{r}_2$ are the position vector of the two electrons respectively, and $\boldsymbol{E}$ is the electric field of the laser pulse. If the laser pulse is linearly polarized in the z direction, then the transition matrix for the one-photon process reduces to

$$T_1 = \langle \psi_\mathrm{f} | E(z_1 + z_2) | \psi_\mathrm{i} \rangle = 2E \langle \psi_\mathrm{f} | Z | \psi_\mathrm{i} \rangle, \tag{4.2}$$

where $Z = (z_1 + z_2)/2$ is the center of mass of the two electrons in the z direction. From the expression for the transition matrix, it is obvious that the final-state wave function needs to be opposite in Z-symmetry to the initial-state wave function to make the transition matrix T_1 nonzero. If the initial state is the ground state that is symmetric in Z, then the final state must be antisymmetric in Z, i.e., there will be a node in the configuration space wave function at $Z = 0$, or a node in the correlated momentum distribution at $p_Z = 0$.

In contrast, the transition matrix for a two-photon process would be

$$T_2 = \sum_{\tilde{\psi}} \langle \psi_{\rm f} | \boldsymbol{E} \cdot (\boldsymbol{r}_1 + \boldsymbol{r}_2) | \tilde{\psi} \rangle \langle \tilde{\psi} | \boldsymbol{E} \cdot (\boldsymbol{r}_1 + \boldsymbol{r}_2) | \psi_{\rm i} \rangle = 4E^2 \langle \psi_{\rm f} | Z^2 | \psi_{\rm i} \rangle, \tag{4.3}$$

where $\tilde{\psi}$ is the intermediate state. Here, it is evident that the final-state wave function needs to have the same Z-symmetry as the initial-state wave function to make the transition matrix T_2 nonzero. If the initial state is symmetric in Z, then the final state must be symmetric in Z as well, i.e., there is not necessarily a node in the configuration space wave function at $Z = 0$ (or $p_Z = 0$ in the correlated momentum distribution).

For higher-photon processes, the pattern goes on in an alternating manner. An increase of the number of absorbed photons leads to alternating nodes and antinodes of the two-electron wave function at $Z = 0$. If the initial state is symmetric in Z, then odd-photon double ionization leads to a node at $Z = 0$, and even-photon double ionization results in an antinode at $Z = 0$.

Note that the initial-state wave function needs to have a definite Z-symmetry for the selection rules to apply. In a system whose Hamiltonian is symmetric in Z, it can be approved that the eigenstates of this system should have a definite symmetry in Z. Therefore, the selection rules apply to the systems whose Hamiltonian is symmetric in Z. For the Hamiltonian of a two-electron system, this Z-symmetry indeed only exists when $X = (x_1 + x_2)/2 = 0$ and $Y = (y_1 + y_2)/2 = 0$. As a result, the restriction in the correlated emission of the two electrons in the configuration space wave function is indeed at $X = Y = Z = 0$, which is equivalent to $\boldsymbol{r}_1 = -\boldsymbol{r}_2$ in selection rule (2) above. As a result, an increase of the number of absorbed photons leads to an alternating suppression and non-suppression of the back-to-back emission of the two electrons with equal energy sharing.

4.2.3 Selection rules based on the correlated Keldysh–Faisal–Reiss theory

The KFR theory [4, 105, 106] is a S-matrix [107] treatment of the above-threshold-ionization process [108–110], and the same selection rules can be concluded from the correlated version of the KFR theory [103, 104]. The fully differential cross section for a N-photon process in this theory

can be written as

$$\frac{d^3\sigma^{(N)}}{d\Omega_1 d\Omega_2 dE_2} \propto J_N^2\left(\boldsymbol{\alpha}_0, \boldsymbol{k}_1, \boldsymbol{k}_2\right), \tag{4.4}$$

where $\boldsymbol{\alpha}_0$ is the quiver radius, and

$$J_N\left(\boldsymbol{\alpha}_0, \boldsymbol{k}_1, \boldsymbol{k}_2\right) = \sum_{m=-\infty}^{\infty} J_{N+2m}\left(\boldsymbol{\alpha}_0 \cdot (\boldsymbol{k}_1 + \boldsymbol{k}_2)\right) J_m\left(\frac{U_\mathrm{p}}{\omega}\right), \tag{4.5}$$

where U_p is the ponderomotive potential, ω is the frequency of the laser field, and J is the Bessel function. In a linearly polarized laser pulse, the quiver radius is along the polarization direction, or the z direction in the present case. Here, J_N reduces to

$$J_N\left(\boldsymbol{\alpha}_0, \boldsymbol{k}_1, \boldsymbol{k}_2\right) = \sum_{m=-\infty}^{\infty} J_{N+2m}(\alpha_0 p_Z) J_m\left(\frac{U_\mathrm{p}}{\omega}\right), \tag{4.6}$$

which further reduces to

$$J_N\left(\boldsymbol{\alpha}_0, \boldsymbol{k}_1, \boldsymbol{k}_2\right) = \sum_{m=-\infty}^{\infty} J_{N+2m}(0) J_m\left(\frac{U_\mathrm{p}}{\omega}\right), \tag{4.7}$$

at $p_Z = 0$. Note that the Bessel function $J_n(0)$ is non-zero only when $n = 0$, and that N and m are integers, we therefore have (at $p_Z = 0$)

$$J_N\left(\boldsymbol{\alpha}_0, \boldsymbol{k}_1, \boldsymbol{k}_2\right) = \begin{cases} J_{-N/2}\left(\frac{U_\mathrm{p}}{\omega}\right), & (\text{even } N) \\ 0. & (\text{odd } N) \end{cases} \tag{4.8}$$

As a result, the same selection rules as discussed above can be found from the correlated KFR theory, namely there is a suppression of back-to-back emission of the two electrons with equal energy sharing when odd number of photons are absorbed, while there is no such a suppression for even number of photons absorbed.

4.3 Selection rules in the helium atom

The general selection rules above apply for the helium atom, the helium dimer, and homogeneous diatomic molecules. To study them more thoroughly, we apply numerical model simulations to the helium atom and the helium dimer for more details. In this section, we focus on the selection rules in the helium atom. To this end, we first introduce a restricted 3D model of the helium atom and then numerically study the selection rules in this model.

4.3.1 The restricted 3D model of the helium atom

Following earlier achievements towards the solution of the full TDSE for the helium atom interacting with an intense laser pulse in view of an analysis of nonsequential double ionization at optical and near-infrared laser wavelengths (see [111] and references therein), in recent years much theoretical interest has been devoted to the double ionization of atoms by absorption of two photons (see [112–116] for most recent studies and references therein). In the case of the two-photon process, results for the total cross sections as well as for momentum distributions have been reported. In particular, the passage from a simultaneous absorption of the photons (and simultaneous ejection of the electrons) to sequential double ionization, in which absorption of the first photon generates a singly charged ion before absorption of the second photon leads to the removal of the second electron, has been studied.

We are interested in analyzing the occurrence of nodes for particular configurations of the position and momentum vectors in the probability density and the momentum distributions in numerical simulations. To this end, we may make use of any (lower-dimensional) model, which exhibits all or some of the above selection rules. Here, we employ of a model for the helium atom in which the center-of-mass motion of the two electrons is restricted to the polarization axis of the linearly polarized external laser field. The Hamiltonian of this two-electron model (in Jacobi coordinates) is given by [63]

$$\begin{aligned} H(\rho,z,Z;t) =& p_\rho^2 + p_z^2 + \frac{p_Z^2}{4} - \frac{p_Z A_Z(t)}{c} + \frac{1}{\sqrt{\rho^2+z^2}} \\ & - \frac{2}{\sqrt{\rho^2/4+(Z+z/2)^2+a^2}} - \frac{2}{\sqrt{\rho^2/4+(Z-z/2)^2+a^2}}, \end{aligned} \tag{4.9}$$

where a^2 is a soft-core parameter to smooth the Coulomb singularity.

Our model, as shown in Fig. 4.1, restricts the center-of-mass motion of the two electrons along the polarization direction, but does not restrict the symmetry of the dipole transition operator. Since a linearly polarized laser field interacts with the center-of-mass of the two electrons along the polarization axis, the symmetry of the dipole transition operator is present in the model. Thus, the considerations regarding the symmetries of the accessible final states discussed above apply in

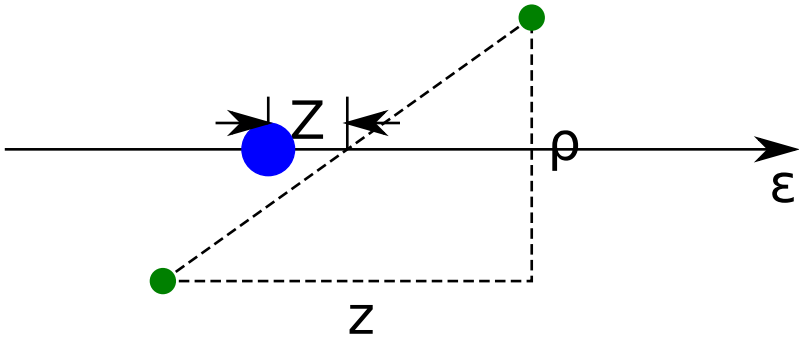

Figure 4.1. The restricted 3D model of the helium atom. The blue dot represents the helium nucleus, and the two green dots stand for the two electrons in the helium atom, the center of mass of which is fixed along the polarization direction ε (the z direction) of the laser field.

this model as well. In general, in our model the momentum components of the individual electron along the polarization direction differ and therefore both equal and unequal energy sharings occur. However, along $Z = 0$ and $p_Z = 0$ only equal energy sharing is present in the model. This coincides with the kinematics for the nodes according to selection rules (2) and (3), which are predicted to occur for equal energy sharing. Thus, for these two selection rules the model captures the relevant dynamics. Selection rule (1) can occur for special cases of unequal momentum components in the transverse direction as well, which is not captured by the present model and is a restriction in view of the present analysis. Moreover, in our model the node arising due to selection rule (3) coincides with that due to selection rule (2). Thus, in the remainder of the article, we will mainly discuss our results in view of selection rule (2).

In the actual computations the TDSE of the two-electron model is solved using the Crank–Nicolson method. The initial ground state wave function $\psi(\rho, z, Z; t = 0)$ is computed through imaginary time propagation using a grid size of $\Delta\rho = \Delta z = \Delta Z = 0.3$, and $a^2 = 0.135$. The field-free ground state energies of helium atom and helium ion are found to be -2.937 and -1.985 respectively, which are both close to the real values of -2.904 and -2. The propagation of the wave function in the field is conducted using a box size with $N_\rho = 300$, $N_z = 600$, and $N_Z = 300$ points in the respective directions. An absorbing boundary of the form $\cos^{1/6}\left(\frac{\pi}{2}\frac{|x-x_0|}{L}\right)$ with $|x| \geqslant |x_0|$, spanning 10% of the box size in a certain direction, is used, where x_0 denotes the border of the

boundary region and L is its width.

In this following sections, we present the results of a series of numerical simulations based on the model presented above. In our calculations we change the wavelength and peak intensity of the laser pulse such that the double ionization process can proceed via simultaneous absorption of one up to four photons. The wavelengths are chosen such that the probability for sequential double ionization is small (or negligible) in each of the cases considered, as shown schematically in Fig. 4.2. In each of the computations we use a $\sin^2$-pulse with a total length of six cycles.

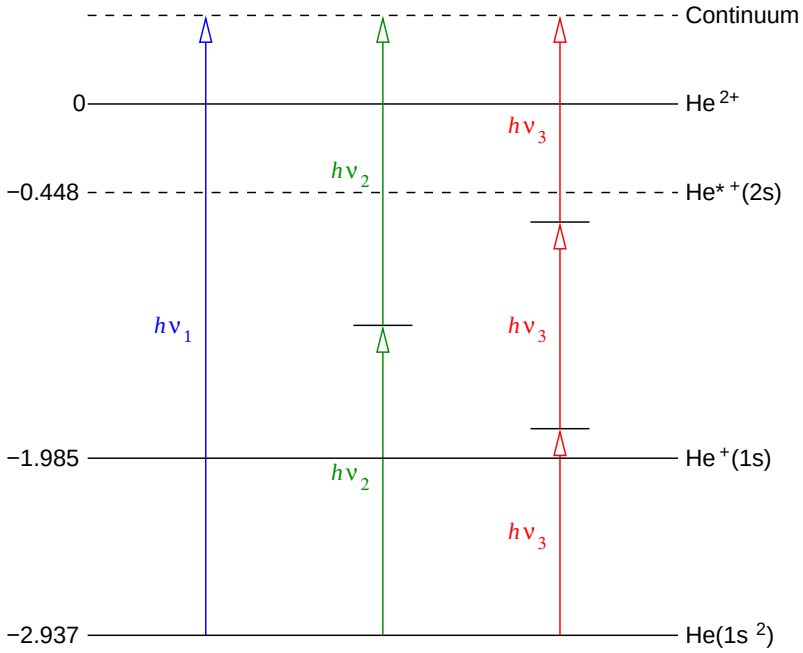

Figure 4.2. The photoabsorption scheme in the restricted 3D model of the helium atom. In the scheme, $h\nu_1$, $h\nu_2$, and $h\nu_3$ correspond to one-, two-, three-photon double ionization, respectively. The wavelengths used in these three cases are $\lambda_1 = 14.32$ nm, $\lambda_2 = 28.64$ nm, and $\lambda_3 = 42.96$ nm, respectively.

4.3.2 One-photon double ionization

First, we consider a central laser wavelength of 14.32 nm and a peak intensity of $I_0 = 1 \times 10^{14}$ W/cm^2. At this wavelength the photon energy of 3.182 a.u. exceeds the double ionization threshold of our model He atom and the two electrons can be emitted after absorption of a single photon. Fig. 4.3 shows snapshots of the probability density distribution $|\psi(\rho, z, Z; t)|^2$ integrated over ρ (left

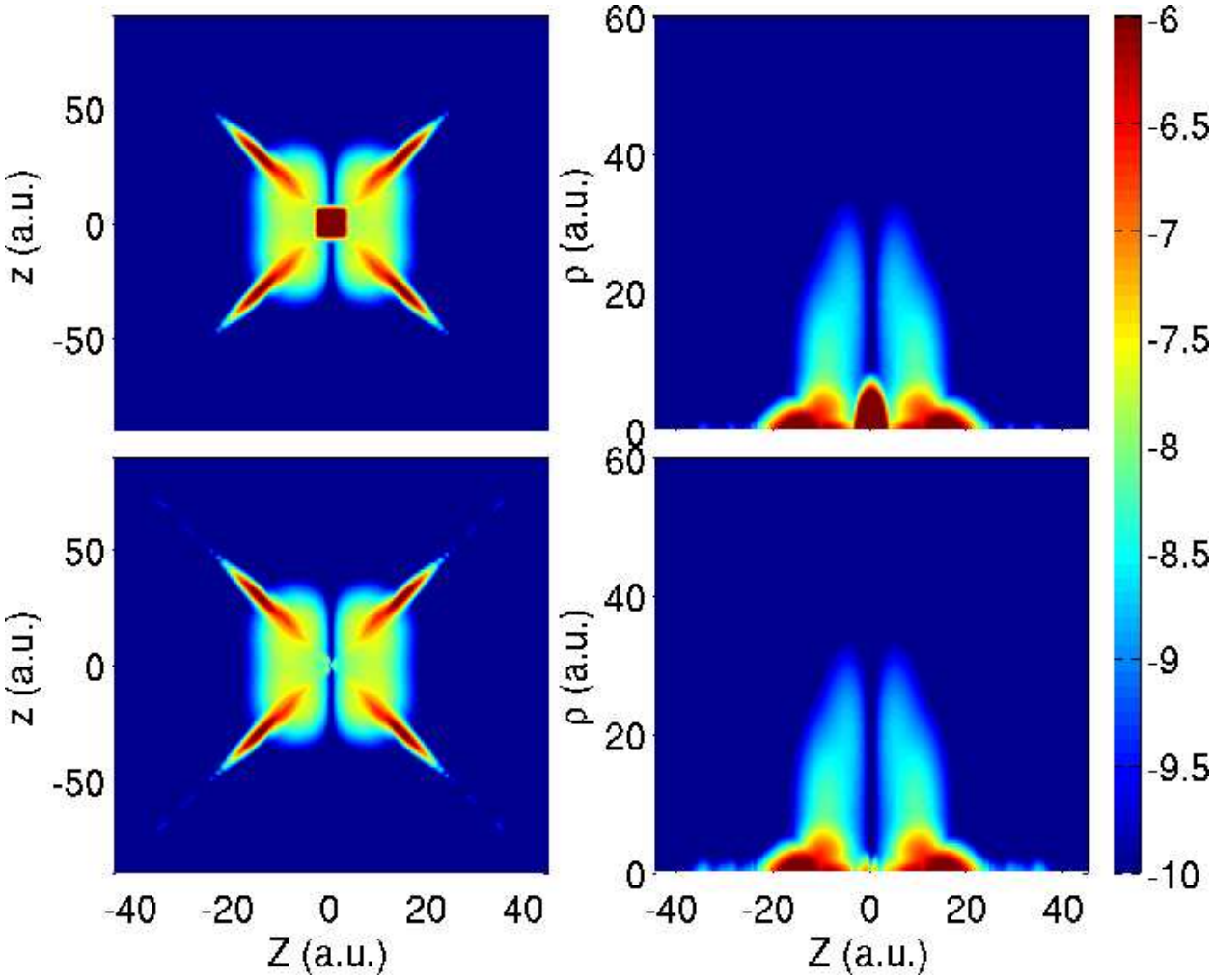

Figure 4.3. Probability density distribution (on a logarithmic scale) as a function of z and Z (integrated over ρ, left hand column) and as a function of ρ and Z (integrated over z, right hand column) following single-photon double ionization. In the results, presented in the panels in the lower row, the ground state wave function was removed before calculating the probability density distribution. The snapshots are taken at $t = 10$ a.u. after the end of the laser pulses. Laser parameters: wavelength $\lambda = 14.32$ nm, peak intensity $I_0 = 1 \times 10^{14}$ W/cm^2, and total pulse length 6 cycles.

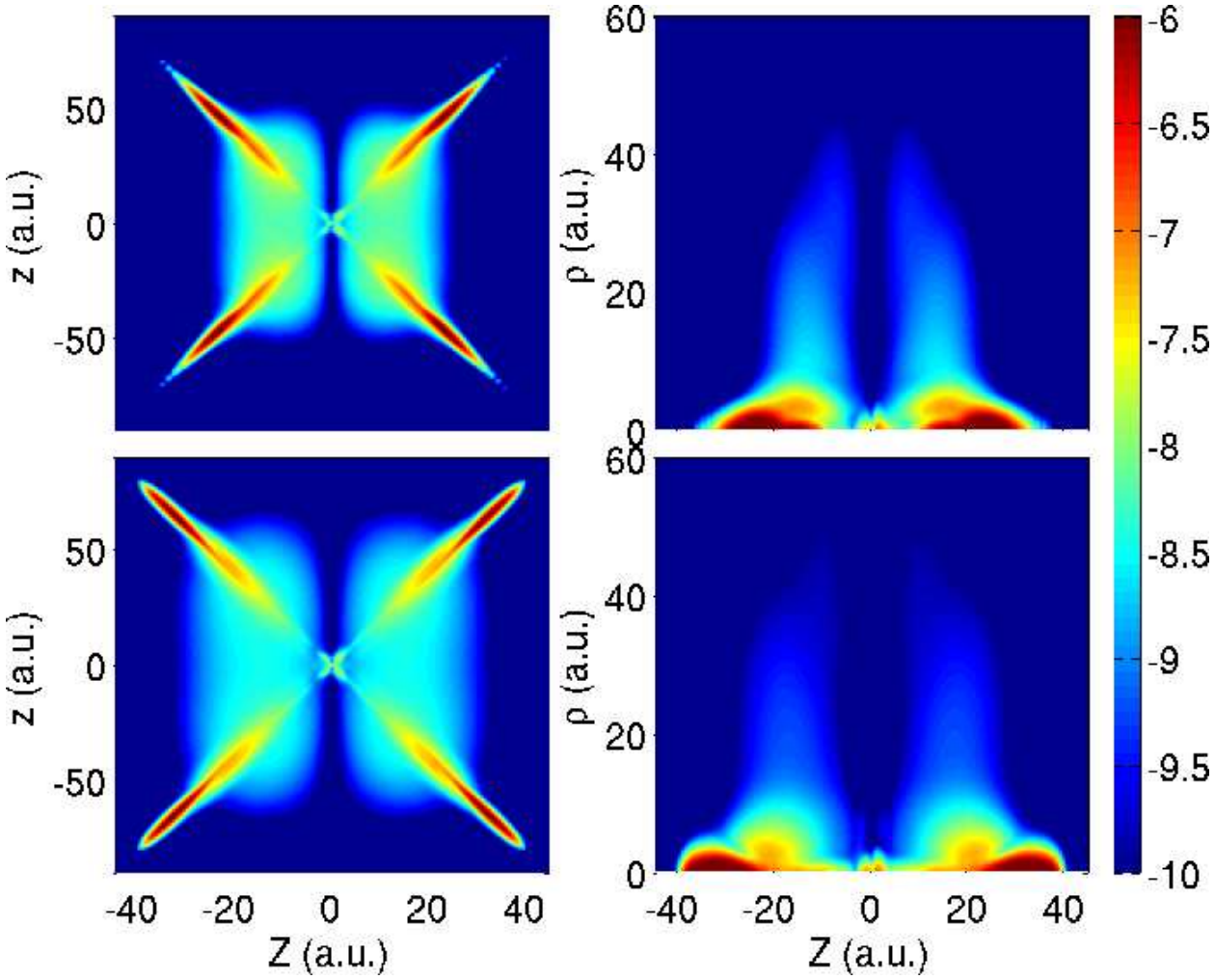

Figure 4.4. Same as Fig. 4.3 but at times $t = 20$ a.u. (upper row) and $t = 30$ a.u. (lower row) after the end of the laser pulses. Shown are the probability density distributions after removal of the He ground state from the full wave function.

hand panels) or z (right hand panels) at time $t = 10$ a.u. after the end of the pulse. Plots in the column on the left show distributions in the $Z-z$ plane (integrated over the ρ-coordinate). In these plots the contributions at the center ($z \approx Z \approx 0$) mainly correspond to the remaining population in the neutral helium atom after the interaction. This can be clearly seen from the comparison of the plots in the upper and lower panel in the left hand column, since the He ground state contribution is removed in the results in the lower panel. The single ionized population is displayed along the diagonals, while the contributions to double ionization can be found in the regions in between the diagonals. We clearly see a node along $Z = 0$ in the distribution, as predicted by selection rule (2) and shown by Briggs and co-workers before [99]. In previous analysis of single-photon double ionization, usually asymptotic final states (in time-independent S-matrix calculations) were considered, the present results offer a time-dependent view. It is seen from the results in Figs. 4.3 and 4.4 (the latter shows the distributions at two later time instants) that the node is present as soon as the pulse is over.

The plots in the right hand columns of Figs. 4.3 and 4.4 offer the complementary view of the $Z - \rho$ distributions, integrated over z. While the distributions at small ρ are mainly due to contributions from the neutral He atom and the He^+ ion, the population at large ρ indicates a highly correlated process, i.e., the double ionization. Again, in all of the plots we see a node at $Z = 0$ for the contribution belonging to double ionization, as expected from the selection rule (2) and the earlier work on single-photon double ionization [99].

4.3.3 Two-photon double ionization

Next, we consider two-photon double ionization, for which we expect that the node at $Z = 0$ is not present according to the selection rules. Simultaneous absorption of two photons does occur either as a second above-threshold double ionization peak (ATDI) [103, 104] at higher intensities in the wavelength regime considered above, or at longer wavelengths at which the photon energy is smaller than the double ionization threshold. In our simulations we have analyzed both cases.

First, we present in Fig. 4.5 results at the same wavelength as above but at a higher peak

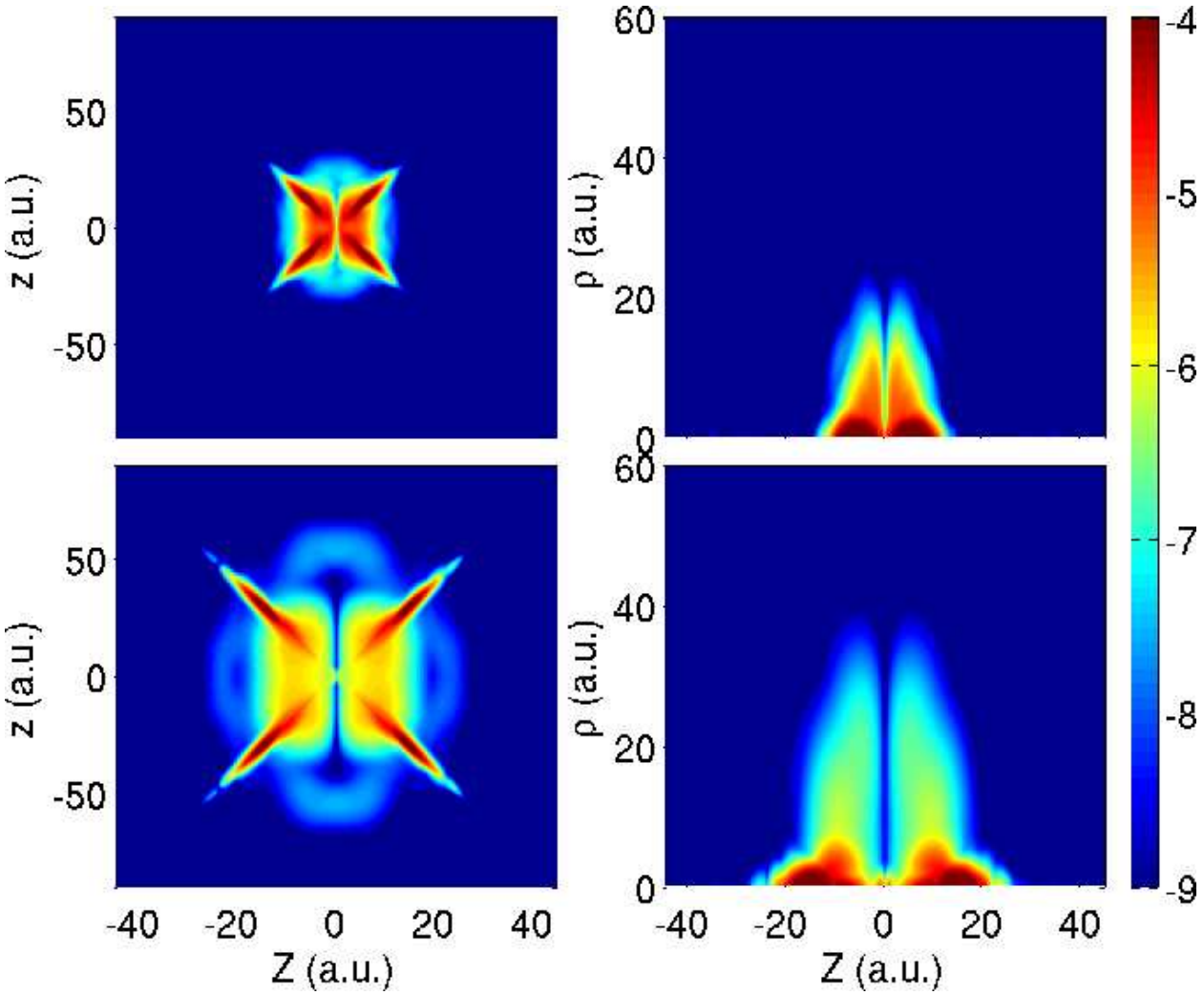

Figure 4.5. Probability density distribution (on a logarithmic scale) as a function of z and Z (integrated over ρ, left hand column) and as a function of ρ and Z (integrated over z, right hand column). The ground state wave function was removed before calculating the probability density distribution. The snapshots are taken at the end of the pulse (upper row) and $t = 10$ a.u. after the pulse (lower row). Laser parameters: wavelength $\lambda = 14.32$ nm, peak intensity $I_0 = 1 \times 10^{16}$ W/cm^2, and total pulse length 6 cycles.

intensity of $I_0 = 1 \times 10^{16}$ W/cm^2. While in the $z - Z$ distribution taken at the end of the pulse (panel in upper left corner) the evolving population in the double ionization region does not show a clear structure, we can distinguish the contributions from single-photon and two-photon double ionization at some later time after the end of the pulse ($t = 10$ a.u., panel in lower left corner). Please note that due to the difference in total kinetic energy the single-photon contribution propagates at a smaller velocity than the two-photon contribution. Consequently, we find the latter contribution at larger distances from the center of the $z - Z$ distribution (i.e., the nucleus) than the one-photon distribution. Our expectations for the contribution along $Z = 0$ are obviously realized in the numerical results for the $z - Z$ distribution (lower panel in left hand column): The absorption of two photons results in a maximum in the corresponding part of the distribution, while the node in the single-photon contribution is still present. In the $Z - \rho$ distributions (panels in right hand column) there is no clear separation of the two processes possible and, hence, we observe a small population along $Z = 0$ due to the two-photon process.

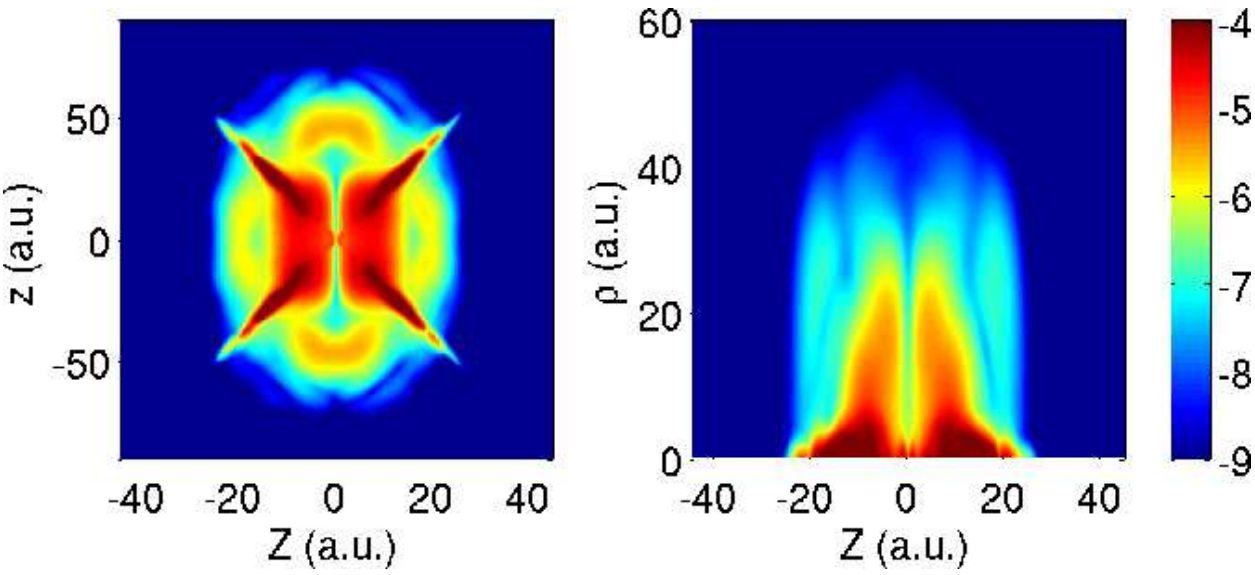

Figure 4.6. Same as Fig. 4.5, but at $I_0 = 1 \times 10^{17}$ W/cm^2 and $t = 7.5$ a.u. after the end of the pulse.

Similar conclusions hold for the results at an even higher intensity of $I_0 = 1 \times 10^{17}$ W/cm^2, shown in Fig. 4.6. Here the contribution from the two-photon absorption (2nd ATDI peak) with

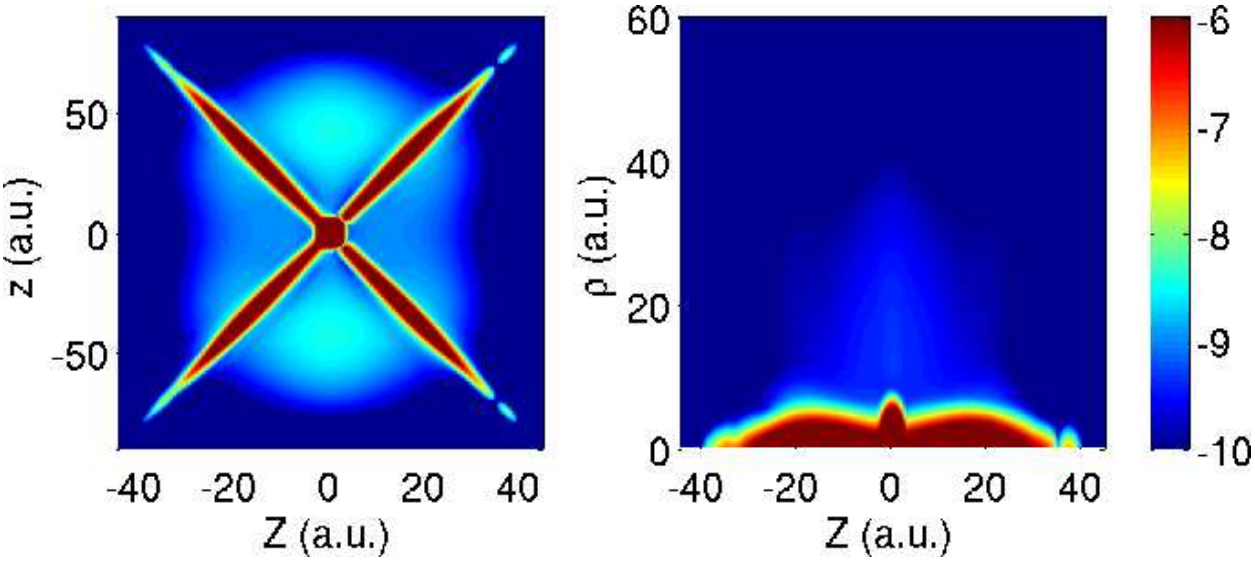

Figure 4.7. Probability density distribution (on a logarithmic scale) as a function of z and Z (integrated over ρ, left hand column) and as a function of ρ and Z (integrated over z, right hand column). The snapshots are taken $t = 30$ a.u. after the pulse. Laser parameters: wavelength $\lambda = 28.64$ nm, peak intensity $I_0 = 1 \times 10^{14}$ W/cm^2, and total pulse length 6 cycles.

a maximum along $Z = 0$ in the $Z - z$ distribution is much stronger, as expected due to the nonlinearity of the process. A clear separation of the single-photon process from the two-photon process is however not longer possible on the grid size used in the present simulations.

Next, we double the central wavelength of the laser field to $\lambda = 28.64$ nm (photon energy of 1.591 a.u.). At this wavelength the (simultaneous) absorption of two photons is needed to overcome the double ionization threshold. Please note that the photon energy has been chosen such that a competing sequential double ionization process requires the absorption of at least three photons and, hence, the corresponding contribution to the two-electron configuration space wave function is strongly suppressed. The results in Fig. 4.7 do not show a node along $Z = 0$ either in the $Z - z$ or in the $Z - \rho$ distribution, in agreement with the selection rule (2) for a two-photon process from the He ground state. Instead, we observe as in the previous results in Figs. 4.5 and 4.6 a maximum in the contributions from double ionization along this axis in the $Z - z$ distribution. Please note that the maximum indicates a preferential back-to-back emission of the two electrons at the present laser parameters, in agreement with recent observations in experiments on two-photon double ionization of He [117] and Ne [118], as well as recent theoretical predictions [119].

4.3.4 Three- and four-photon double ionization

Finally, we consider double ionization processes via the simultaneous absorption of more than two photons in order to verify (or, disprove) the alternating appearance of suppression and non-suppression of electron emission along the $Z = 0$ axis in the configuration space wave function for double ionization as the number of absorbed photons increases. We found that at longer wavelengths the contributions of competing processes such as sequential double ionization are usually of similar (or even larger) strengths than the probability for the ejection of two electrons via simultaneous absorption of photons. However, at specific wavelengths (and peak intensities), here 42.96 nm and 57.28 nm, we observe double ionization which arises from simultaneous three- and four-photon absorption. The results of the numerical simulations (see Fig. 4.8) clearly exhibit the suppression (for the odd-number-photon process) and the non-suppression (for the even-number-photon process)

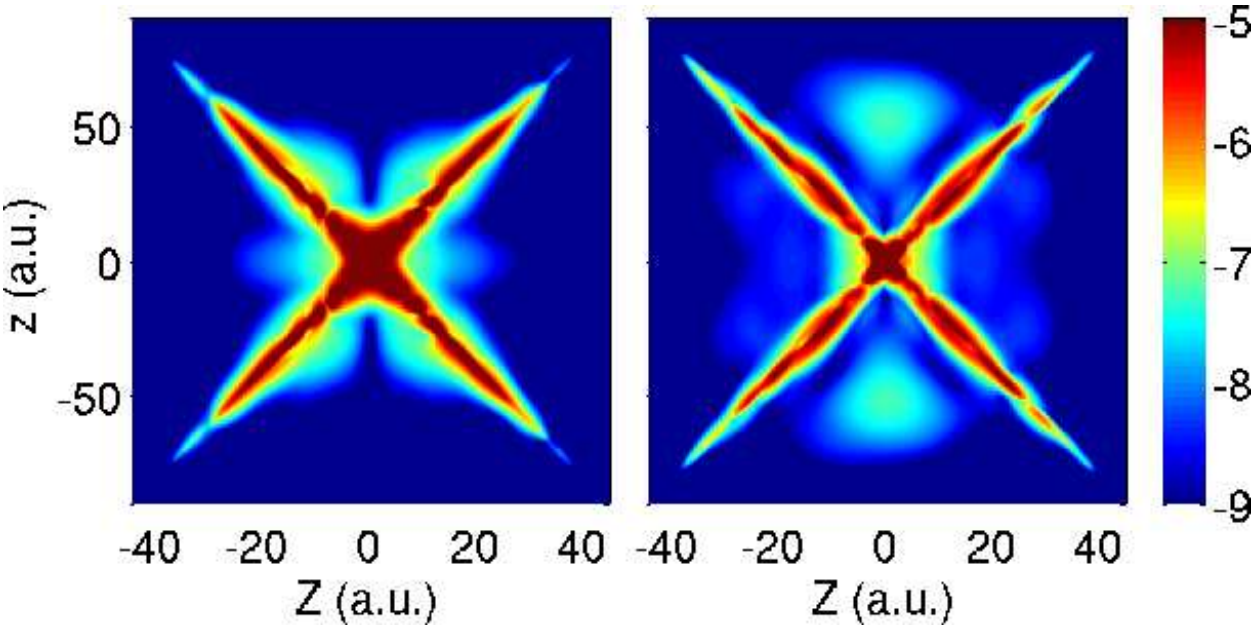

Figure 4.8. Probability density distribution (on a logarithmic scale) as a function of z and Z (integrated over ρ). The snapshots are taken $t = 12.25$ a.u. after the pulse. Laser parameters: wavelength $\lambda = 42.96$ nm (left hand column) and 57.28 nm (right hand column), peak intensity $I_0 = 5 \times 10^{14}$ W/cm^2, and total pulse length 6 cycles.

of electron emission along the $Z = 0$ axis in the $Z - z$ distributions, as expected from the selection rule (2).

4.3.5 Momentum distributions

As of now, we have demonstrated the selection rules in the configuration space of the two electrons. At the same time, the selection rules also apply to the momentum space distributions. As discussed above: When there is a node in the configuration space, there should be a corresponding node in the momentum space; and when there is an antinode in the configuration space, there should also be a corresponding antinode in the momentum space. Due to the lower dimensionality of our numerical model we cannot provide quantitative predictions for the full momentum distributions but test certain aspects, here the existence of nodes.

Fig. 4.9 shows correlated momentum distributions for the two electrons in the $p_Z - p_z$ plane (upper row, integrated over p_ρ direction) and along the p_Z axis (lower row, integrated over both p_z and p_ρ). The momentum distributions are obtained by first separating the doubly ionized part of the configuration space wave function from the rest. To this end, we partition the coordinate space (refer to Sec. 2.7) as [63]

$$\begin{cases} r_1 \leqslant 12 \cap r_2 \leqslant 12 : & \text{He atom} \\ (r_1 \leqslant 6 \cap r_2 > 12) \cup (r_1 > 12 \cap r_2 \leqslant 6) : & \text{He}^+ \text{ ion} \\ \text{complementary space} : & \text{He}^{2+} \text{ ion}, \end{cases} \tag{4.10}$$

where $r_{1,2} = \sqrt{\rho^2/4 + (Z \pm z/2)^2}$. Then, we project the doubly ionized part onto the final-state wave function, which we approximate by a product state of a Coulomb wave in the relative coordinates ρ and z and a plane wave in the center-of-mass coordinate Z.

The momentum distributions displayed in the three columns correspond to the probability density distributions

(a) in the lower row of Fig. 4.4, in which the single-photon process dominates,

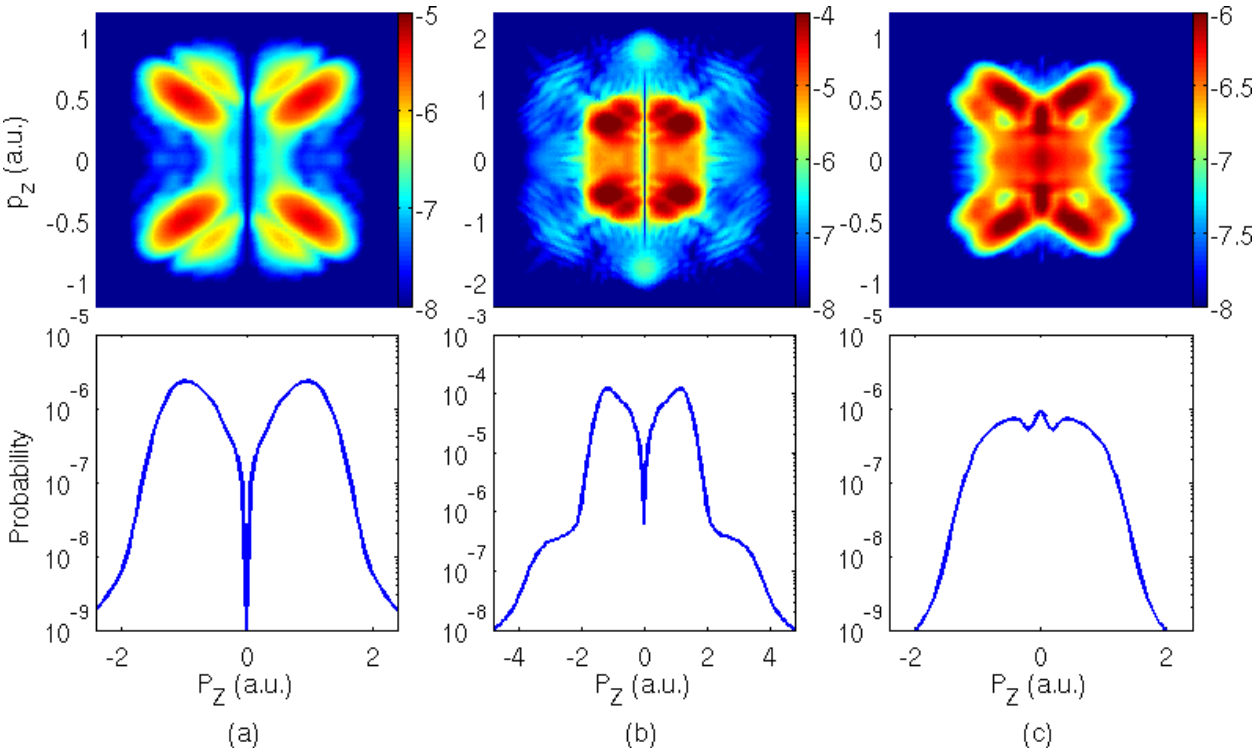

Figure 4.9. Correlated momentum distribution of p_z and p_Z (upper row) and momentum distribution in p_Z (lower row, integrated from upper row over p_z) by projection onto the approximate final-state wave function of a Coulomb wave in the relative coordinates ρ and z and a plane wave in the center-of-mass coordinate Z. Laser parameters: wavelength $\lambda = 14.32$ nm [column (a) and (b)] and 28.64 nm [column (c)], peak intensity $I_0 = 1 \times 10^{14}$ W/cm^2 [column (a) and (c)] and 1×10^{16} W/cm^2 [column (b)], and total pulse length 6 cycles.

(b) in the lower row of in Fig. 4.5, in which both one- and two-photon processes are present, and

(c) in Fig. 4.7, in which the two-photon process is prominent.

It is obvious from the comparison of the results in Fig. 4.9 with the corresponding spatial distributions that both show the same nodes and antinodes. In particular, the nodes for the odd-number photon processes along $p_Z = 0$ in the $p_Z - p_z$ distributions (upper row of Fig. 4.9) can be clearly seen. We have found that the appearance of the nodes is insensitive to the method by which we extract the ionized population from the full wave function. It is also independent of how long the wave function is propagated after the end of the pulse and of the choice of the basis set for the two-electron continuum wave functions.

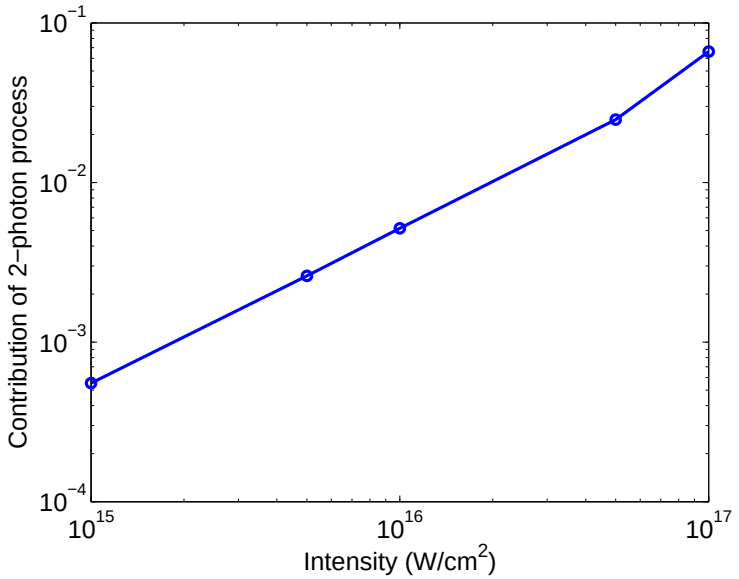

Figure 4.10. Ratio of the probability at $p_Z = 0$ to the maximum probability in the p_Z distributions as a function of intensity at a wavelength of 14.32 nm.

Comparing the momentum distributions in columns (a) and (b) we find that the contribution of the two-photon process increases with intensity at the wavelength of 14.32 nm. This can be quantified by the ratio of the probability at $p_Z = 0$ to the maximum probability in the p_Z distributions (lower row in Fig. 4.9), as shown in Fig. 4.10. One can see that the ratio increases

almost linearly as a function of intensity. This is expected since the ratio basically represents the ratio between the probabilities for one- to two-photon absorption, which should follow the power law $I^2/I^1 = I^1$.

Instead of using the approximate final-state wave function of a Coulomb wave in the relative coordinates ρ and z and a plane wave in the center-of-mass coordinate Z to get the momentum distributions, we can also use the approximate final-state wave function of a plane wave, which is equivalent to carrying out a Fourier transform to the respective spatial wave function to obtain the momentum distributions. Shown in Fig. 4.11 is the same plot as in Fig. 4.9 but is obtained by projection onto a plane wave (Fourier transform).

The difference between these two methods, i.e., projection onto the approximate final-state wave function of a Coulomb wave in the relative coordinates ρ and z and a plane wave in the center-of-mass coordinate Z (Fig. 4.9) and projection onto the approximate final-state wave function of a plane wave (Fig. 4.11), is that electron-electron correlation is taken into consideration in the former case, and it is not accounted for in the latter case. The electron-electron correlation, or electron-electron repulsion, will cause the two electrons to stay away from each other, which would result in a node at $\rho = z = 0$ (and $p_\rho = p_z = 0$). This can be clearly seen in Fig. 4.12, in which the first row is the cut of Fig. 4.9 and the second row is the cut of Fig. 4.11 at $p_\rho = 0$. A node at $p_z = 0$ is evident in the first row, in which electron-electron correlation is taken into account, and it is missing in the second row, where electron-electron repulsion is absent.

4.4 Selection rules in the helium atom within the planar 4D model

In the last section, we studied the selection rules in the helium atom using the restricted 3D model. To illustrate that the selection rules do not depend on the specific model, we introduce a planar 4D model of the helium atom and then study part of the selection rules within this model.

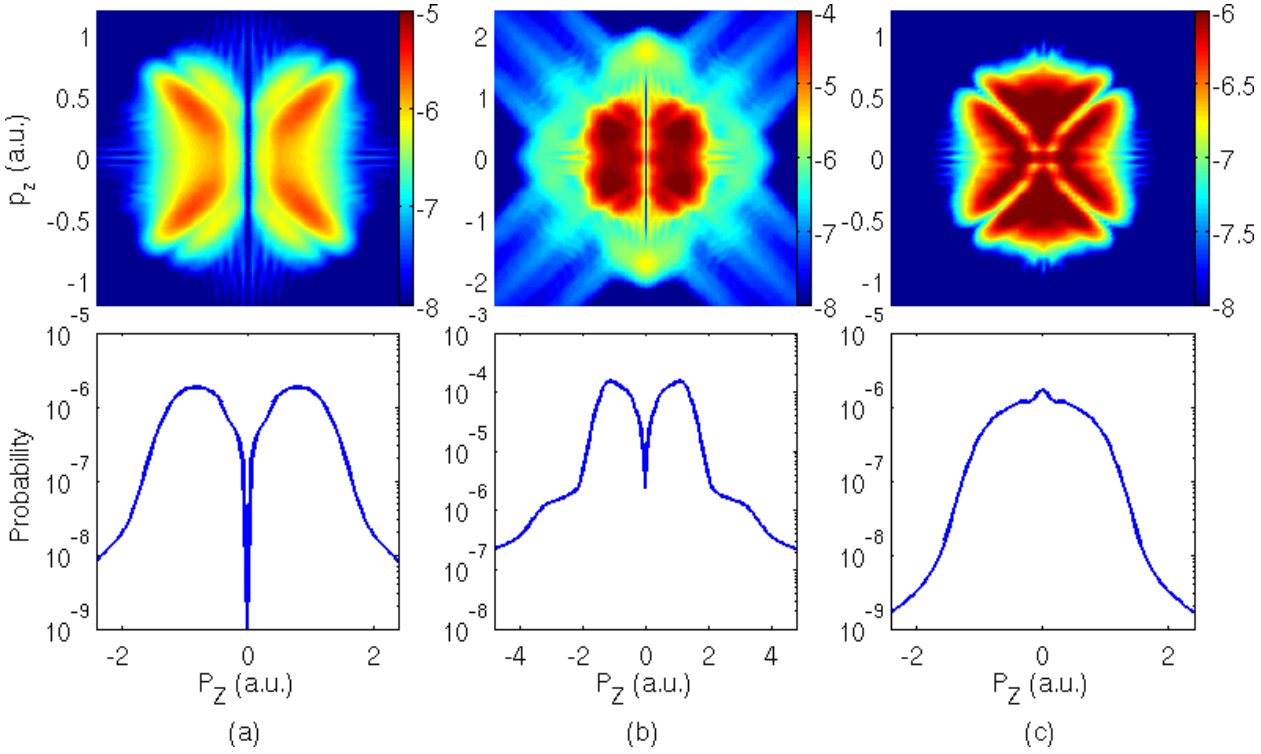

Figure 4.11. Correlated momentum distribution of p_z and p_Z (upper row) and momentum distribution in p_Z (lower row, integrated from upper row over p_z) by projection onto the approximate final-state wave function of a plane wave (Fourier transform). Same laser parameters are used as in Fig. 4.9.

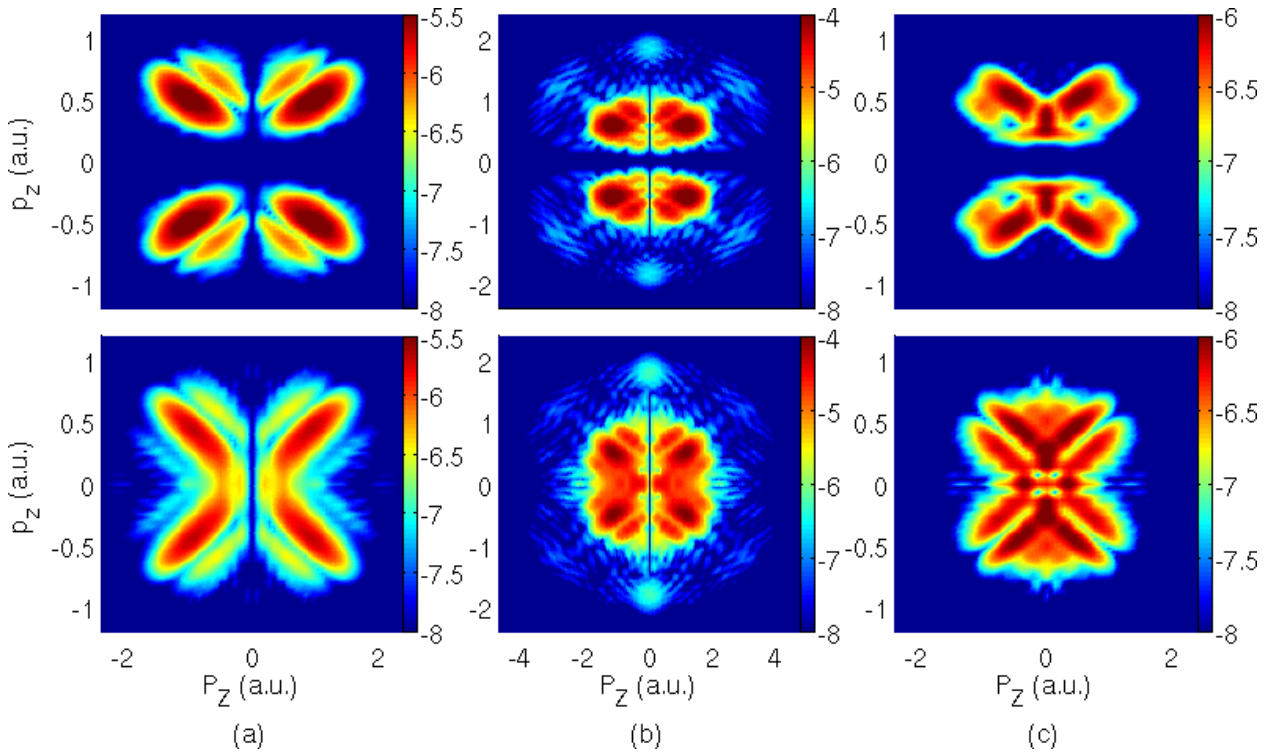

Figure 4.12. Correlated momentum distribution of p_z and p_Z cut at $p_\rho = 0$ by projection onto the approximate final-state wave function of a Coulomb wave in the relative coordinates ρ and z and a plane wave in the center-of-mass coordinate Z (upper row) and by projection onto the approximate final-state wave function of a plane wave (Fourier transform, lower row). Same laser parameters are used as in Figs. 4.9 and 4.11.

4.4.1 The planar 4D model of the helium atom

The planar 4D model of the helium atom removes the restriction of the center of mass of the two electrons to the polarization direction of the laser field in the restricted 3D model of the atom, but restrains the two electrons and the helium nucleus to the same plane. After this change, each electron has two spatial dimensions and the corresponding four-dimensional model Hamiltonian is then given by

$$\begin{aligned} H(x_1, x_2, z_1, z_2; t) =& \frac{p_{x_1}^2 + p_{z_1}^2}{2} + \frac{p_{x_2}^2 + p_{z_2}^2}{2} + E(t)(z_1 + z_2) \\ & - \frac{2}{\sqrt{x_1^2 + z_1^2 + a^2}} - \frac{2}{\sqrt{x_2^2 + z_2^2 + a^2}} + \frac{1}{\sqrt{(x_1 - x_2)^2 + (z_1 - z_2)^2 + b^2}}, \end{aligned} \tag{4.11}$$

where $\boldsymbol{p}_i = (p_{x_i}, p_{z_i})$ and $\boldsymbol{r}_i = (x_i, z_i)$ (with $i = 1, 2$) are the momentum operators and spatial coordinates of the two electrons and a^2 and b^2 are the soft-core parameters to smooth the Coulomb singularity. The linearly polarized laser field is given in the form of

$$E(t) = \cos^2\left(\frac{\omega t}{2N}\right)\cos(\omega t + \phi), \tag{4.12}$$

where ω is the central frequency, N is the number of cycles, and ϕ is the carrier-envelope phase of the laser pulse, which is set to $-\pi/2$ is the present simulations.

In the actual computations the TDSE of the two-electron model is solved using the Crank–Nicolson method. The initial ground state wave function $\psi(x_1, x_2, z_1, z_2; t = 0)$ is computed through imaginary time propagation using a grid size of $\Delta x_1 = \Delta x_2 = \Delta z_1 = \Delta z_2 = 0.3$, $a^2 = 0.164$, and $b^2 = 0.068$, which is found to have an energy of -2.9034. The propagation of the wave function in the field is conducted using a box with $N_{x_1} = N_{x_2} = 200$ and $N_{z_1} = N_{z_2} = 300$ points in the respective directions. An absorbing boundary of the form $\cos^{1/6}\left(\frac{\pi}{2}\frac{|x - x_0|}{L}\right)$ with $|x| \geqslant |x_0|$, spanning 10% of the box size in a certain direction, is used, where x_0 denotes the border of the boundary region and L is its width. The double ionization contributions are obtained with the space-partitioning method in Sec. 2.7 for an atomic system with $d_{\text{small}} = 7$ and $d_{\text{big}} = 11$.

4.4.2 One-photon double ionization

First, we consider a central laser wavelength of 13 nm and a peak intensity of $I_0 = 1 \times 10^{14}$ W/cm^2. At this wavelength the photon energy of 3.507 a.u. exceeds the double ionization threshold of our model helium atom and the two electrons can be emitted after absorption of a single photon. Fig. 4.13(a) shows the snapshot of the probability density distribution $|\psi(x_1, x_2, z_1, z_2; t)|^2$ integrated over x_1 and x_2 at time $t = 4$ a.u. after the end of the pulse. However, no node is visible along $z_1 + z_2 = 0$, or $Z = 0$. This can indeed be easily understood as due to the symmetry of the Hamiltonian, which determines the symmetry of the initial state. To see this clearly, we express the Hamiltonian in the center-of-mass (X and Z) and relative coordinates (x and z) of the two electrons

$$\begin{aligned} H(x, X, z, Z; 0) =& p_x^2 + p_z^2 + \frac{p_X^2 + p_Z^2}{4} + \frac{1}{\sqrt{x^2 + z^2 + b^2}} \\ & - \frac{2}{\sqrt{(X + \frac{x}{2})^2 + (Z + \frac{z}{2})^2 + a^2}} - \frac{2}{\sqrt{(X - \frac{x}{2})^2 + (Z - \frac{z}{2})^2 + a^2}}, \end{aligned} \tag{4.13}$$

where $X = (x_1 + x_2)/2$, $Z = (z_1 + z_2)/2$, $x = x_1 - x_2$, and $z = z_1 - z_2$. Obviously, the Hamiltonian is not symmetric in Z, since it changes if we let $Z \to -Z$. This means that there is no symmetry with respect to Z for the initial state either, which thus, according to the arguments in Sec. 4.2.2, tells us that there should not be a node at $Z = 0$ for the final state either. However, the node can be retrieved if we consider the probability distribution at $X = 0$, $x = 0$, or $z = 0$. In the first case, this leads to the following Hamiltonian

$$\begin{aligned} H(x, X, z, Z; 0) =& p_x^2 + p_z^2 + \frac{p_X^2 + p_Z^2}{4} + \frac{1}{\sqrt{x^2 + z^2 + b^2}} \\ & - \frac{2}{\sqrt{(\frac{x}{2})^2 + (Z + \frac{z}{2})^2 + a^2}} - \frac{2}{\sqrt{(\frac{x}{2})^2 + (Z - \frac{z}{2})^2 + a^2}}, \end{aligned} \tag{4.14}$$

which is symmetric in Z. The respective probability density distribution is shown in Fig. 4.13(b), which clearly has a node at $Z = 0$. In the restricted 3D model this restriction is always imposed, as discussed before.

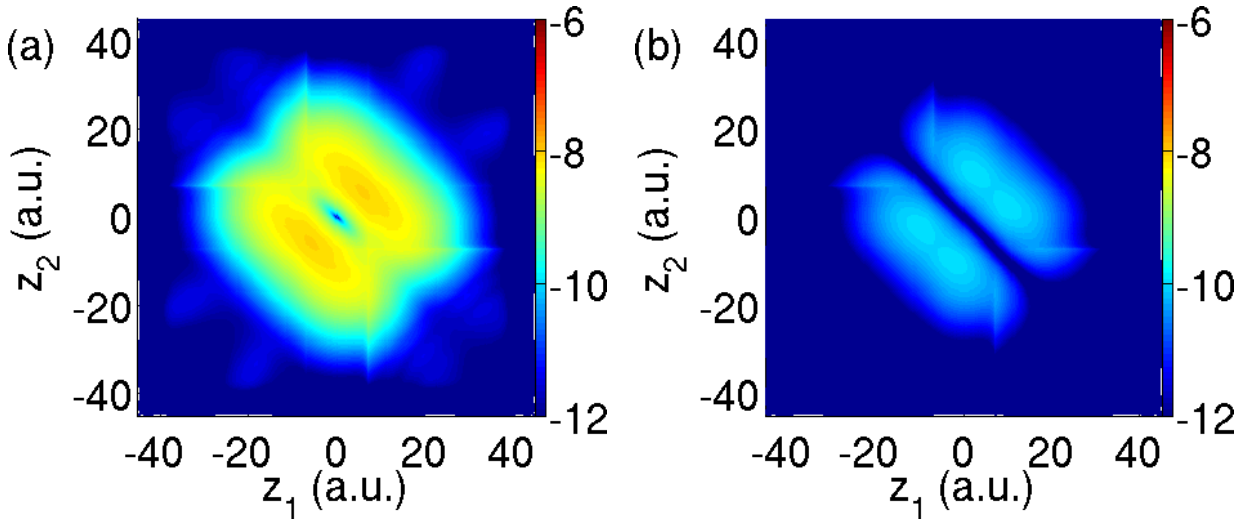

Figure 4.13. Probability density distribution (on a logarithmic scale) as a function of z_1 and z_2 (integrated over x_1 and x_2) following single-photon double ionization. The distribution in panel (b) represents a cut at $X = 0$. The snapshots are taken at $t = 4$ a.u. after the end of the laser pulse. Laser parameters: wavelength $\lambda = 13$ nm, peak intensity $I_0 = 1 \times 10^{14}$ W/cm^2, and total pulse length 12 cycles.

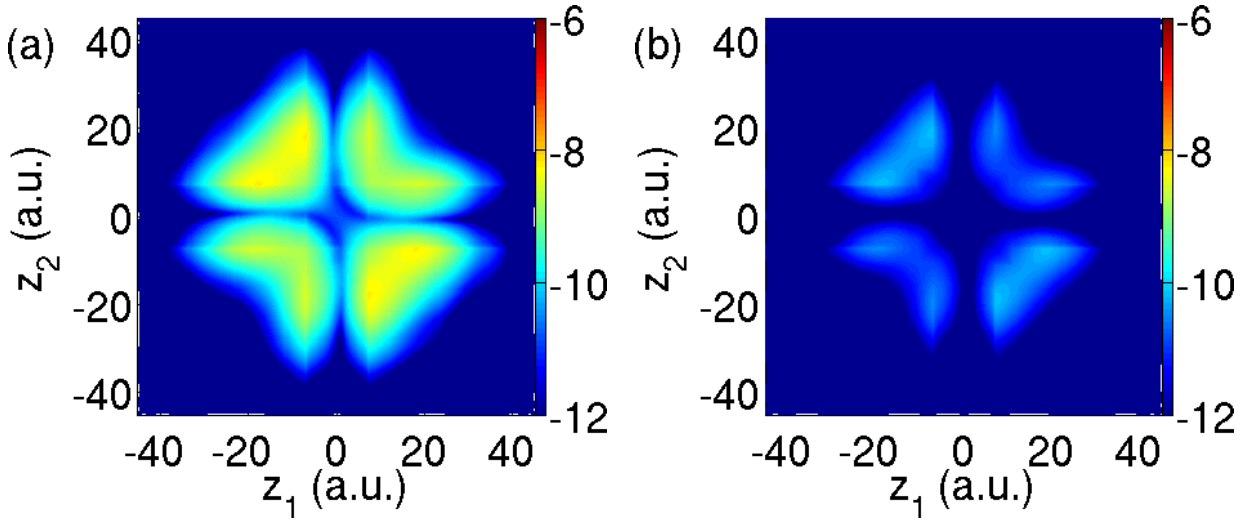

Figure 4.14. Probability density distribution (on a logarithmic scale) as a function of z_1 and z_2 (integrated over x_1 and x_2) following two-photon double ionization. The distribution in panel (b) represents a cut at $X = 0$. The snapshots are taken at $t = 4$ a.u. after the end of the laser pulse. Laser parameters: wavelength $\lambda = 26$ nm, peak intensity $I_0 = 1 \times 10^{14}$ W/cm^2, and total pulse length 6 cycles.

4.4.3 Two-photon double ionization

Next, we consider two-photon double ionization, for which we expect that the node at $Z = 0$ is not present according to the selection rules. Here, we only consider the case when the photon energy is smaller than the double ionization threshold and a simultaneous absorption of two photons is necessary to produce double ionization. To this end, we double the central wavelength of the laser field to $\lambda = 26$ nm (photon energy of 1.753 a.u.). Indeed, the results in Fig. 4.14 do not show a node along $Z = 0$ either in the probability distribution integrated over x_1 and x_2 or in that which is further restricted to $X = 0$, in agreement with the selection rule (2) for a two-photon process from the helium ground state.

4.4.4 Momentum distributions

The selection rules, just as in the restricted 3D model, also apply to the momentum-space distributions. When there is a node in the configuration space, there should be a corresponding node in the momentum space, and when there is an antinode in the configuration space, there should also be a corresponding antinode in the momentum space.

Fig. 4.15 shows correlated momentum distributions for the two electrons in the $p_{z_1} - p_{z_2}$ plane for the single-photon process (upper row) and for the two-photon process (lower row). The momentum distributions are obtained by projecting the doubly ionized part onto the final-state wave function, which we approximate by a product state of a Coulomb wave in the relative coordinates x and z and a plane wave in the center-of-mass coordinates X and Z. Then an integration over p_{x_1} and p_{x_2} results in the momentum-space distribution in the $p_{z_1} - p_{z_2}$ plane. Note that the distributions in the right column further restrict the distributions to $p_X = 0$, just like we restricted to $X = 0$ in the spatial distributions in order to retrieve the node in odd-photon double ionization. Obviously, there is a node present at $p_Z = 0$ for the single-photon process when the $p_X = 0$ condition is enforced, while the node is missing for the two-photon process even when the cut at $p_X = 0$ is done.

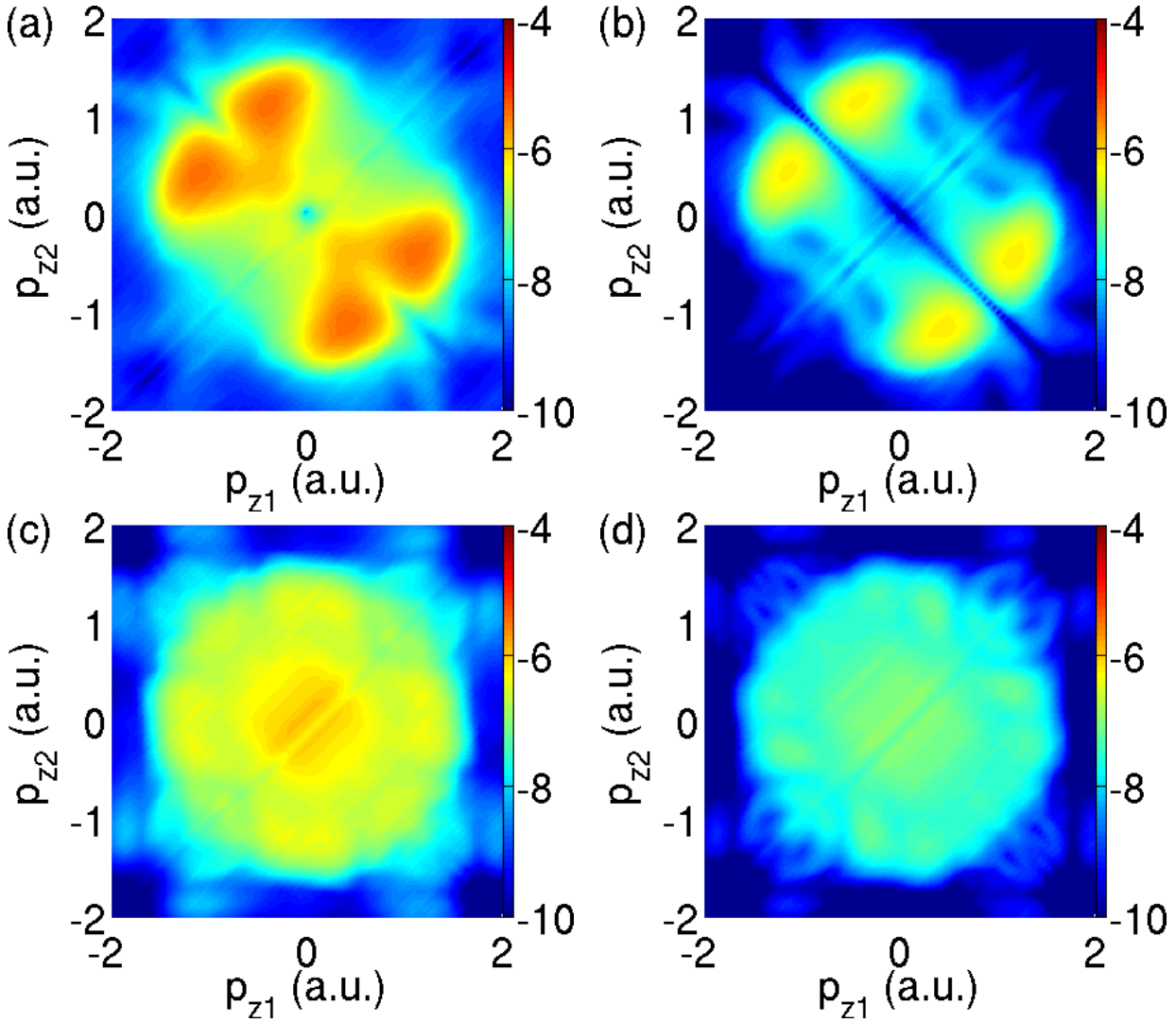

Figure 4.15. Correlated momentum distribution of p_{z_1} and p_{z_2} for the single-photon double ionization (upper row) and two-photon double ionization (lower row) by projection onto the approximate final-state wave function of a Coulomb wave in the relative coordinates x and z and a plane wave in the center-of-mass coordinates X and Z. The distributions in the right column represent a cut at $p_X = 0$. Laser parameters: wavelength $\lambda = 13$ nm (upper row) and 26 nm (lower row), peak intensity $I_0 = 1 \times 10^{14}$ W/cm^2, and total pulse length 12 cycles (upper row) and 6 cycles (lower row).

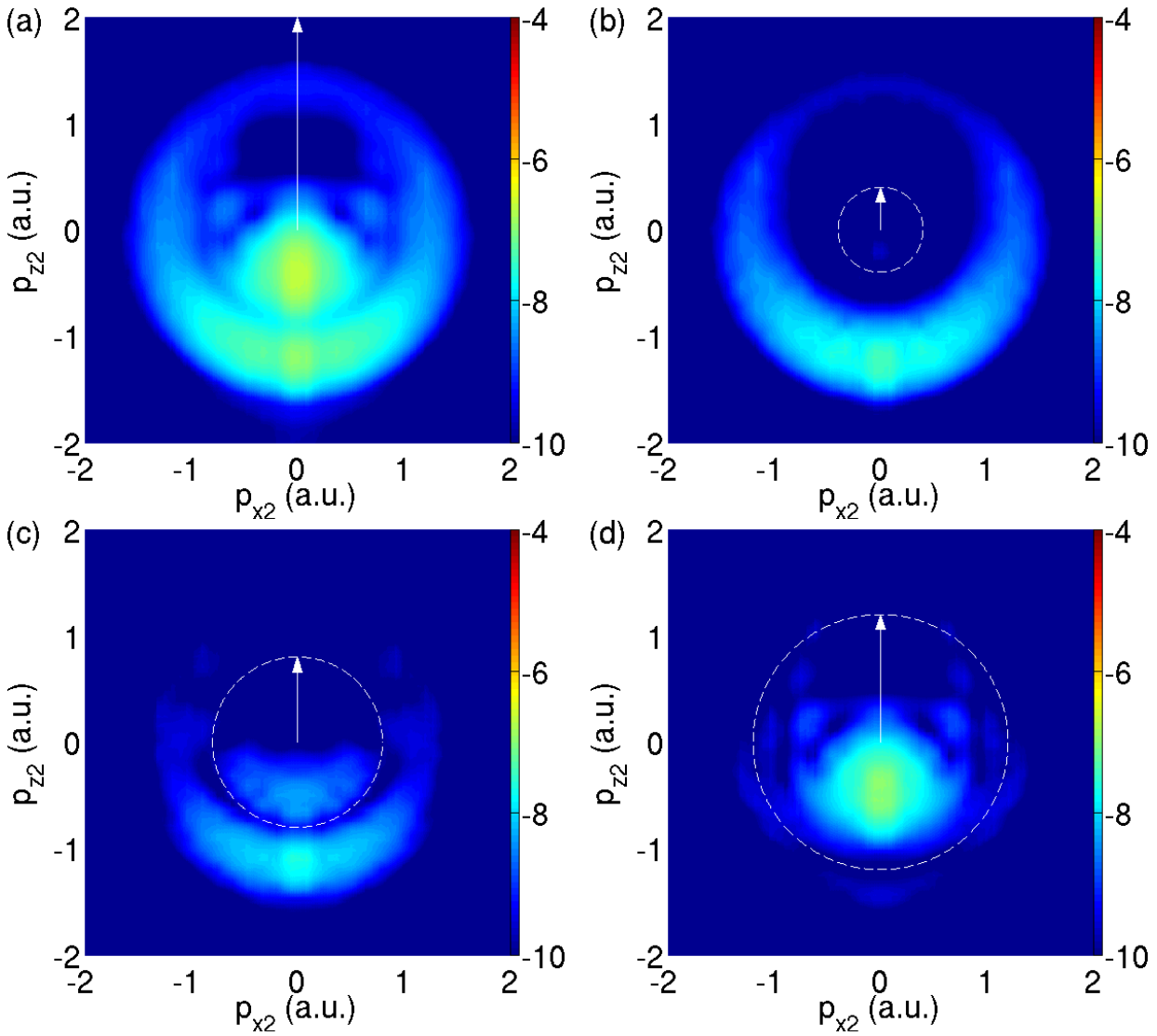

Figure 4.16. Momentum distributions of electron 2 for the single-photon double ionization process when electron 1 is fixed to be emitted along the $+z$ direction. In panels (b), (c), and (d), the magnitude of the momentum of electron 1 is further restricted to certain values, i.e., 0.4, 0.8, and 1.2, respectively. Laser parameters: wavelength $\lambda = 13$ nm, peak intensity $I_0 = 1 \times 10^{14}$ W/cm^2, and total pulse length 12 cycles.

The momentum-space wave function further provides the opportunity to reveal the selection rules in a more straightforward way, i.e., by fixing the momentum of one electron and observing the momentum distribution of the other electron. Shown in Fig. 4.16(a) is the probability distribution of electron 2 when the emission of electron 1 is fixed along the $+z$ direction, which is marked as an arrow, for the single-photon double ionization process. There is no node in the opposite direction of the momentum of electron 1. If we however further select the magnitude of the momentum of electron 1, as it has been done for the results presented in the other panels of Fig. 4.16, we find that, electron 2 cannot be emitted back-to-back to electron 1 for equal energy sharing.

Thus, the selection rules in the few-photon double ionization of the helium atom do not depend on the specific numerical model we are using, and the selection rules apply in both configuration-space and momentum-space wave functions. Generally, the two electrons cannot be emitted back-to-back with equal energy sharing in an odd-photon process, but that is allowed in an even-photon process.

4.5 Selection rules in the helium dimer

In the last sections, we studied the selection rules in the helium atom. In this section, we focus on the selection rules in the helium dimer using the planar 4D model introduced in Sec. 3.2.

4.5.1 One-photon double ionization

First, we consider a central laser wavelength of 20 nm and a peak intensity of $I_0 = 1 \times 10^{14}$ W/cm^2. At this wavelength the photon energy of 2.279 a.u. exceeds the double ionization threshold of our model helium dimer and the two electrons can be emitted after absorption of a single photon. Fig. 4.17(a) and Fig. 4.17(c) shows snapshots of the probability density distribution $|\psi(x_1, x_2, z_1, z_2; t)|^2$ integrated over x_1 and x_2 at time $t = 4$ a.u. after the end of the pulse. Again, no node is visible along $z_1 + z_2 = 0$, or $Z = 0$. Similarly, this can indeed be easily understood as due to the symmetry of the Hamiltonian, which determines the symmetry of the initial state. To see this clearly, we express the Hamiltonian in the center-of-mass (X and Z) and relative coordinates

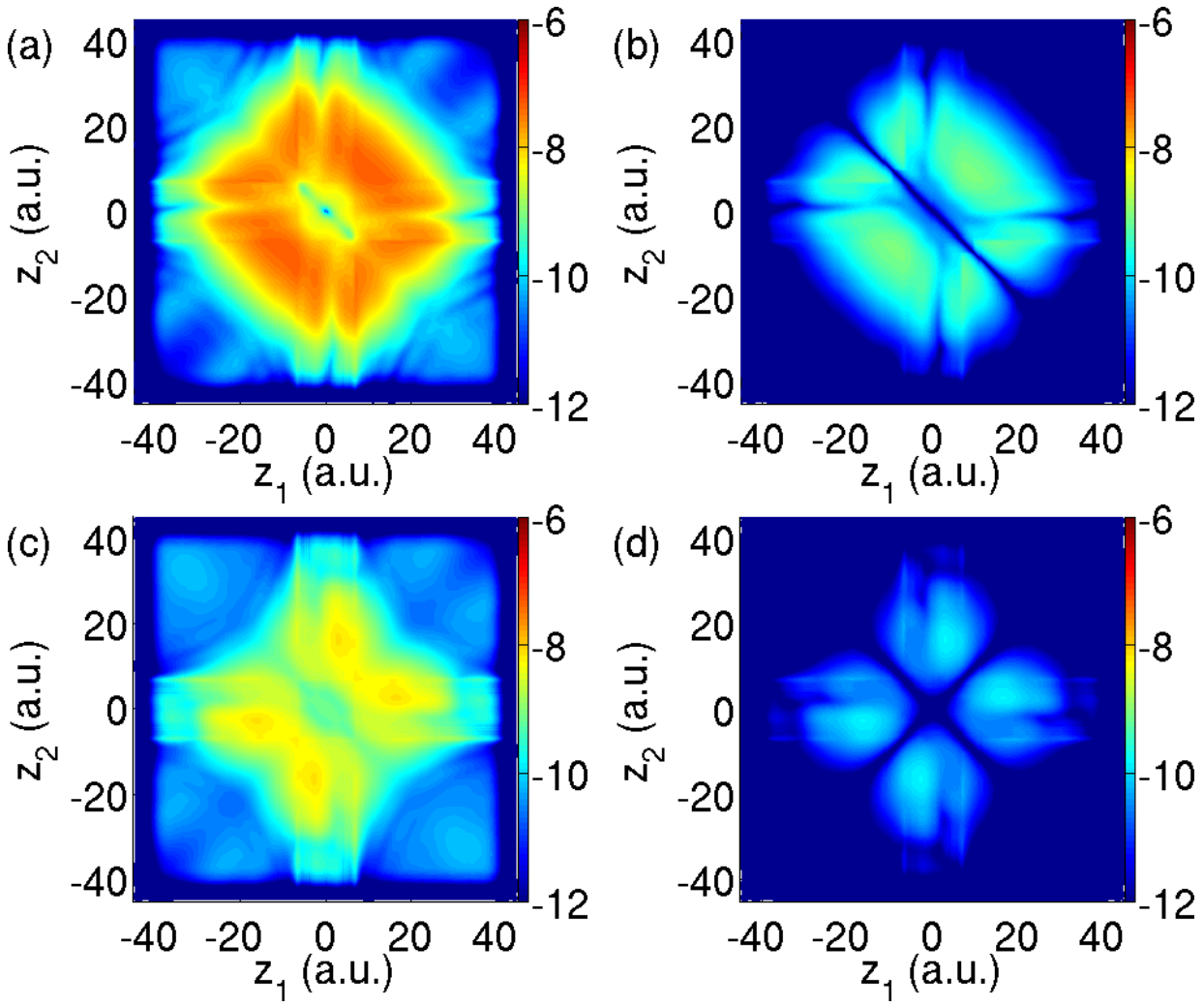

Figure 4.17. Probability density distribution (on a logarithmic scale) as a function of z_1 and z_2 (integrated over x_1 and x_2) following single-photon double ionization starting from the singlet (upper row) and triplet (lower row) states. The distributions in the right column represent a cut at $X = 0$. The snapshots are taken at $t = 4$ a.u. after the end of the laser pulse. Laser parameters: wavelength $\lambda = 20$ nm, peak intensity $I_0 = 1 \times 10^{14}$ W/cm^2, and total pulse length 12 cycles.

(x and z) of the two electrons

$$\begin{aligned} H(x,X,z,Z;0) =& p_x^2 + p_z^2 + \frac{p_X^2+p_Z^2}{4} + \frac{1}{\sqrt{x^2+z^2+b^2}} \\ &+ V_{\rm SAE}\left(\sqrt{\left[X+\frac{x}{2}-\frac{R}{2}\sin\theta\right]^2+\left[Z+\frac{z}{2}-\frac{R}{2}\cos\theta\right]^2+a^2}\right) \\ &+ V_{\rm SAE}\left(\sqrt{\left[X+\frac{x}{2}+\frac{R}{2}\sin\theta\right]^2+\left[Z+\frac{z}{2}+\frac{R}{2}\cos\theta\right]^2+a^2}\right) \\ &+ V_{\rm SAE}\left(\sqrt{\left[X-\frac{x}{2}-\frac{R}{2}\sin\theta\right]^2+\left[Z-\frac{z}{2}-\frac{R}{2}\cos\theta\right]^2+a^2}\right) \\ &+ V_{\rm SAE}\left(\sqrt{\left[X-\frac{x}{2}+\frac{R}{2}\sin\theta\right]^2+\left[Z-\frac{z}{2}+\frac{R}{2}\cos\theta\right]^2+a^2}\right), \end{aligned} \tag{4.15}$$

where $X=(x_1+x_2)/2$, $Z=(z_1+z_2)/2$, $x=x_1-x_2$, and $z=z_1-z_2$. As in the planar He case, the Hamiltonian is not symmetric in Z, since it changes if we let $Z\to -Z$. This means that there is no symmetry with respect to Z for the initial state and therefore no node at $Z=0$ for the final state either. However, as before the node can be retrieved if we consider the probability distribution at $X=0$, $x=0$, or $z=0$. For example, for $X=0$, the Hamiltonian becomes

$$\begin{aligned} H(x,X,z,Z;0) =& p_x^2 + p_z^2 + \frac{p_X^2+p_Z^2}{4} + \frac{1}{\sqrt{x^2+z^2+b^2}} \\ &+ V_{\rm SAE}\left(\sqrt{\left[\frac{x}{2}-\frac{R}{2}\sin\theta\right]^2+\left[Z+\frac{z}{2}-\frac{R}{2}\cos\theta\right]^2+a^2}\right) \\ &+ V_{\rm SAE}\left(\sqrt{\left[\frac{x}{2}+\frac{R}{2}\sin\theta\right]^2+\left[Z+\frac{z}{2}+\frac{R}{2}\cos\theta\right]^2+a^2}\right) \\ &+ V_{\rm SAE}\left(\sqrt{\left[\frac{x}{2}+\frac{R}{2}\sin\theta\right]^2+\left[Z-\frac{z}{2}-\frac{R}{2}\cos\theta\right]^2+a^2}\right) \\ &+ V_{\rm SAE}\left(\sqrt{\left[\frac{x}{2}-\frac{R}{2}\sin\theta\right]^2+\left[Z-\frac{z}{2}+\frac{R}{2}\cos\theta\right]^2+a^2}\right), \end{aligned} \tag{4.16}$$

which is symmetric in Z. The respective probability density distribution is shown in Fig. 4.17(b) and Fig. 4.17(d), the former of which clearly has a node at $Z=0$. Note that the node (minimum) at $z=0$ is due to the exchange asymmetry in the two-electron wave function.

4.5.2 Two-photon double ionization

Next, we consider two-photon double ionization, for which we expect that the node at $Z = 0$ is not present according to the selection rules. As before, we consider only the case when the energy of the photon is smaller than the double ionization threshold and a simultaneous absorption of two photons is necessary to produce double ionization. To this end, we double the central wavelength of the laser field to $\lambda = 40$ nm (photon energy of 1.140 a.u.). The results in Fig. 4.18 do not show a node along $Z = 0$ either in the probability distribution integrated over x_1 and x_2 or in that which is restricted to $X = 0$, in agreement with the selection rule (2) for a two-photon process from the dimer ground state.

4.5.3 Momentum distributions

The selection rules, just as in the case of the helium atom, also apply to the momentum-space distributions. Fig. 4.19 shows correlated momentum distributions for the two electrons in the $p_{z_1} - p_{z_2}$ plane for single-photon double ionization. The momentum distributions are obtained by projecting the doubly ionized part onto the final-state wave function, which we approximate by a product state of a Coulomb wave in the relative coordinates x and z and a plane wave in the center-of-mass coordinates X and Z. Then an integration over p_{x_1} and p_{x_2} results in the momentum-space distribution in the $p_{z_1} - p_{z_2}$ plane. Note that for the distributions in the right column, we have further restricted the distributions to $p_X = 0$. Again, there is a node present at $p_Z = 0$ for the single-photon double ionization process when the $p_X = 0$ condition is enforced.

Fig. 4.20, in contrast, shows correlated momentum distributions for the two electrons in the $p_{z_1} - p_{z_2}$ plane for the two-photon double ionization and there is, as expected, no node present at $p_Z = 0$ for the two-photon double ionization process even when the $p_X = 0$ condition is enforced.

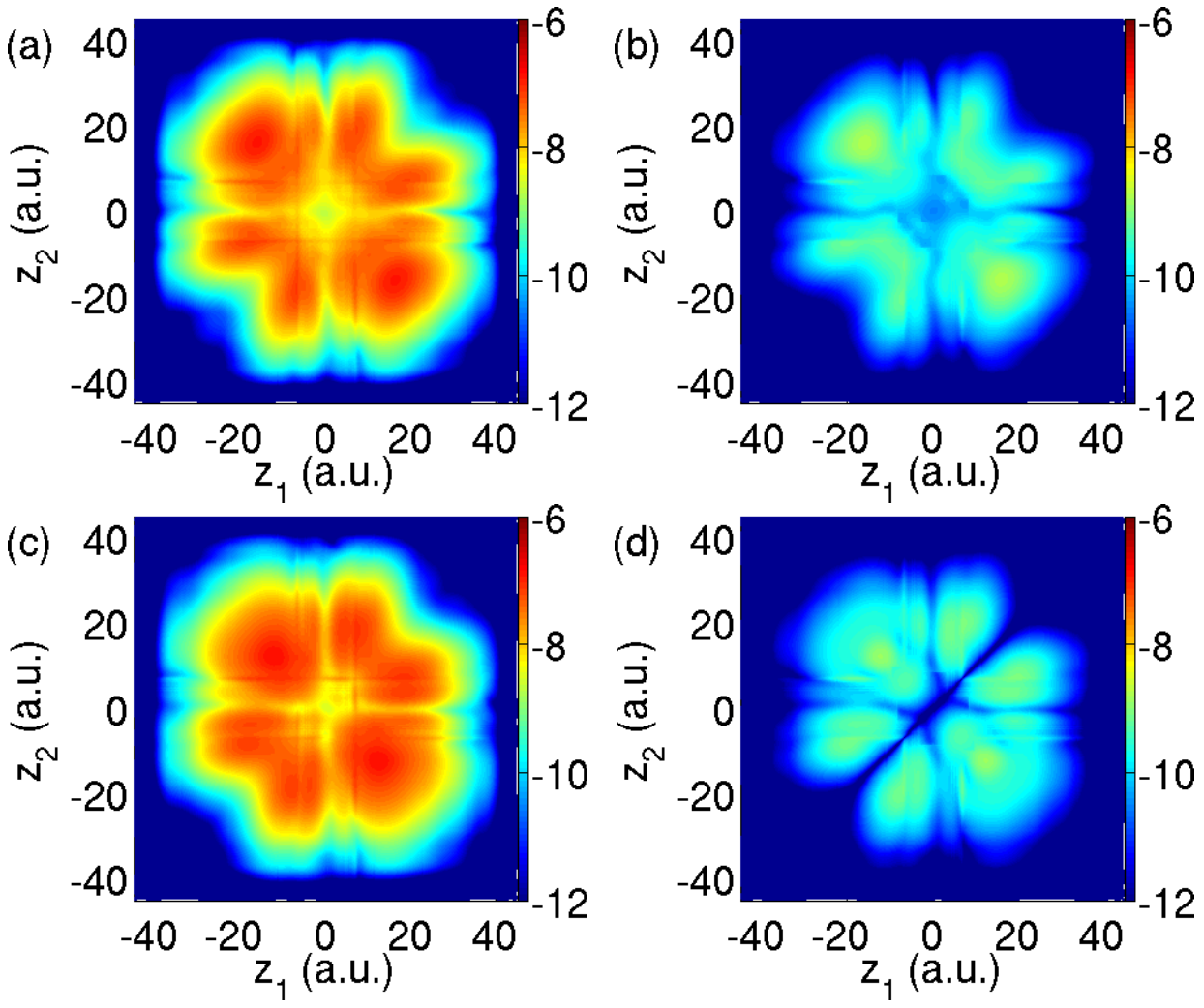

Figure 4.18. Probability density distribution (on a logarithmic scale) as a function of z_1 and z_2 (integrated over x_1 and x_2) following two-photon double ionization starting from the singlet (upper row) and triplet (lower row) states. The distributions in the right column represent a cut at $X = 0$. The snapshots are taken at $t = 4$ a.u. after the end of the laser pulse. Laser parameters: wavelength $\lambda = 40$ nm, peak intensity $I_0 = 1 \times 10^{14}$ W/cm^2, and total pulse length 6 cycles.

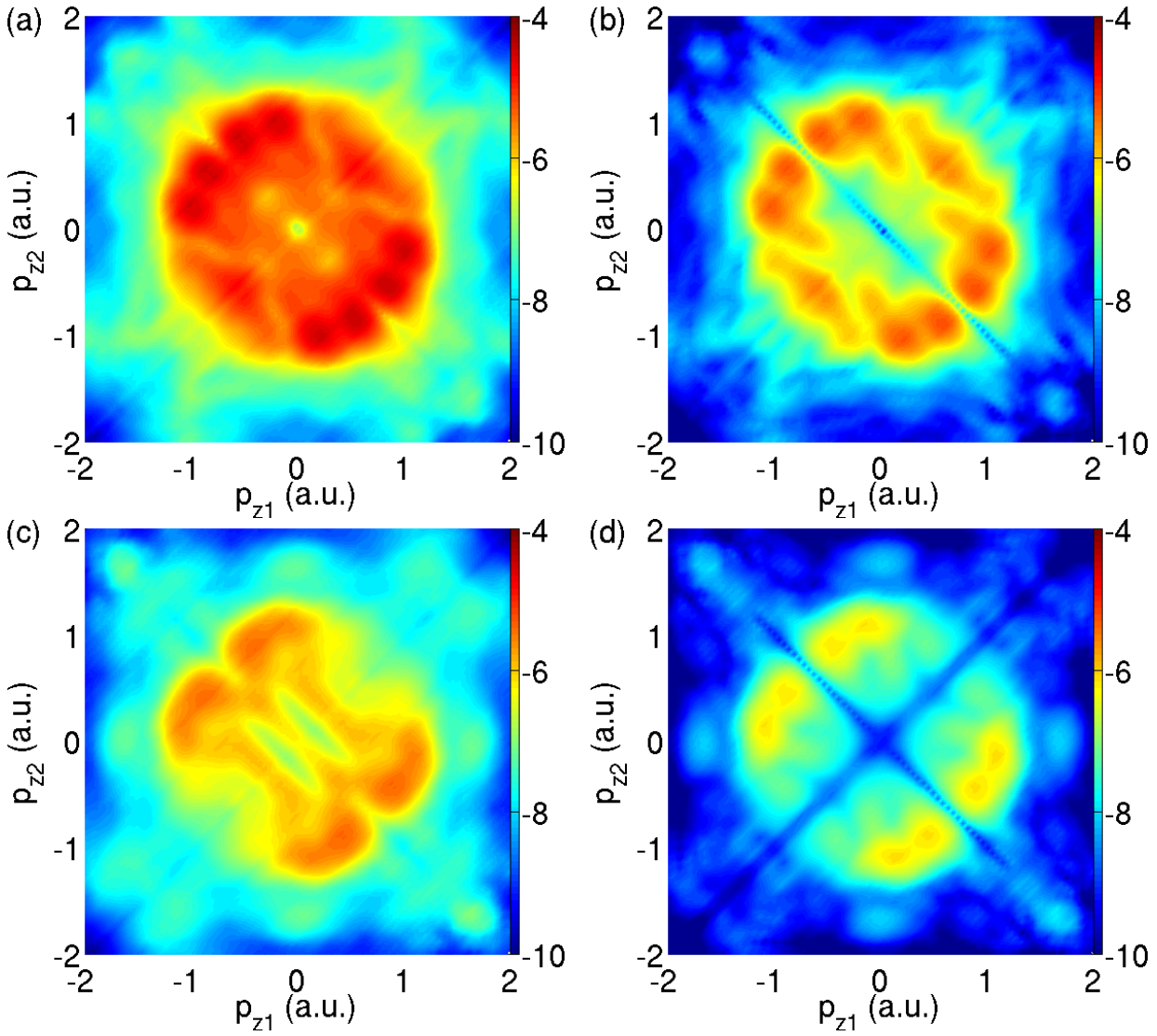

Figure 4.19. Correlated momentum distribution of p_{z_1} and p_{z_2} for the single-photon double ionization double ionization by projection onto the approximate final-state wave function of a Coulomb wave in the relative coordinates x and z and a plane wave in the center-of-mass coordinates X and Z starting from the singlet (upper row) and triplet (lower row) states. The distributions in the right column represent a cut at $p_X = 0$. Laser parameters: wavelength $\lambda = 20$ nm, peak intensity $I_0 = 1 \times 10^{14}$ W/cm^2, and total pulse length 12 cycles.

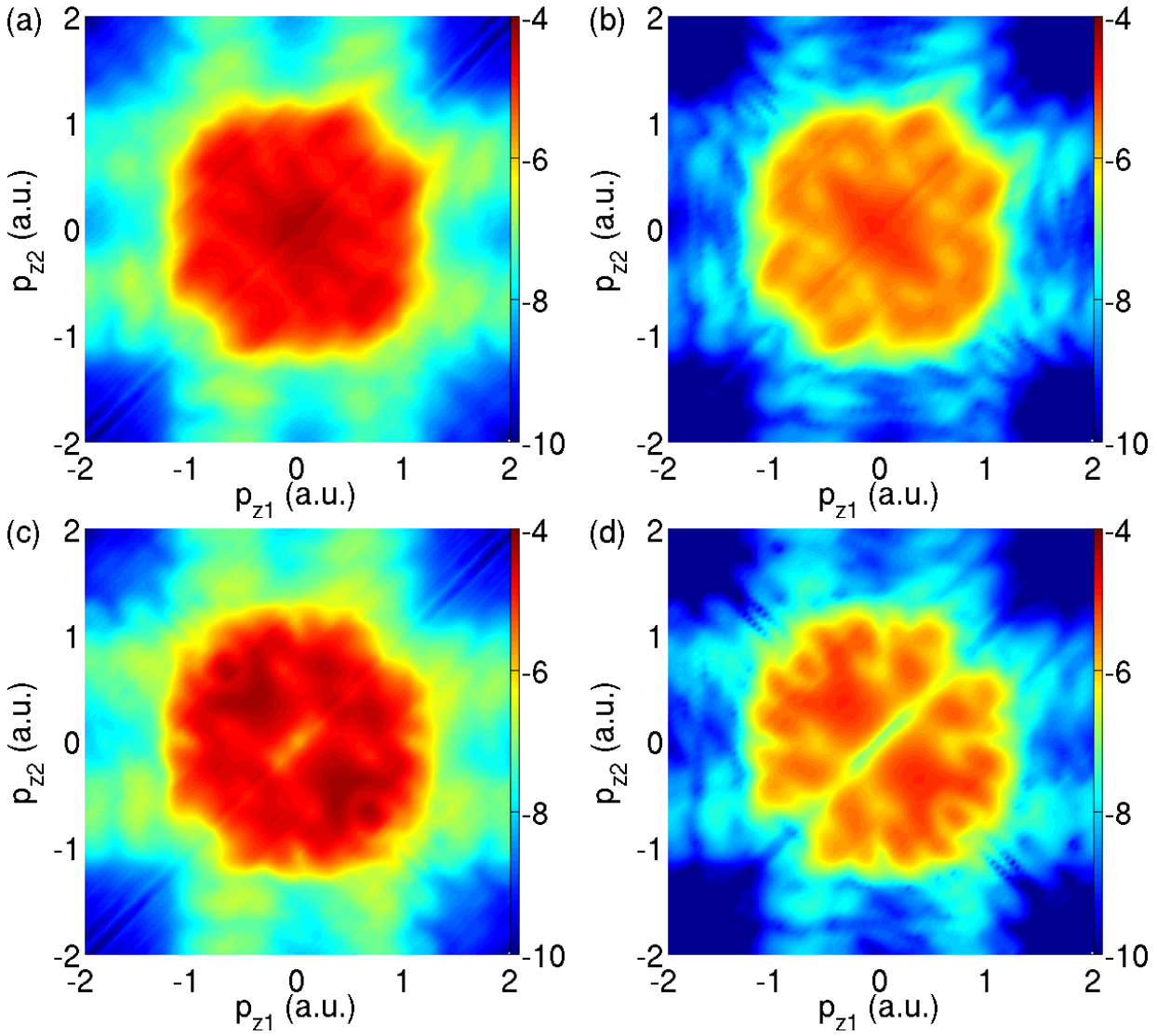

Figure 4.20. Correlated momentum distribution of p_{z_1} and p_{z_2} for the two-photon double ionization double ionization by projection onto the approximate final-state wave function of a Coulomb wave in the relative coordinates x and z and a plane wave in the center-of-mass coordinates X and Z starting from the singlet (upper row) and triplet (lower row) states. The distributions in the right column represent a cut at $p_X = 0$. Laser parameters: wavelength $\lambda = 40$ nm, peak intensity $I_0 = 1 \times 10^{14}$ W/cm^2, and total pulse length 6 cycles.

4.6 General molecules

In previous sections, we focused on one- and two-center systems. In this section, we discuss the symmetry and selection rules in general multicenter systems during few-photon double ionization. To this end, we illustrate the procedure for a homogeneous N-center system. The corresponding Hamiltonian, using center of mass and relative coordinates of the two electrons, can be written as

$$\begin{aligned} H(x,X,z,Z;0) =& p_x^2 + p_z^2 + \frac{p_X^2+p_Z^2}{4} + \frac{1}{\sqrt{(x_1-x_2)^2+(z_1-z_2)^2+b^2}} \\ &+ \sum_{j=1}^{N} V_{\mathrm{SAE}}\left(\sqrt{\left[\frac{X}{2}+x-r_j\sin\theta_j\right]^2+\left[\frac{Z}{2}+z-r_j\cos\theta_j\right]^2+a^2}\right) \\ &+ \sum_{j=1}^{N} V_{\mathrm{SAE}}\left(\sqrt{\left[\frac{X}{2}-x-r_j\sin\theta_j\right]^2+\left[\frac{Z}{2}-z-r_j\cos\theta_j\right]^2+a^2}\right). \end{aligned} \tag{4.17}$$

When we change Z to $-Z$, the Hamiltonian becomes

$$\begin{aligned} H'(x,X,z,Z;0) =& p_x^2 + p_z^2 + \frac{p_X^2+p_Z^2}{4} + \frac{1}{\sqrt{(x_1-x_2)^2+(z_1-z_2)^2+b^2}} \\ &+ \sum_{j=1}^{N} V_{\mathrm{SAE}}\left(\sqrt{\left[\frac{X}{2}+x-r_j\sin\theta_j\right]^2+\left[\frac{Z}{2}-z+r_j\cos\theta_j\right]^2+a^2}\right) \\ &+ \sum_{j=1}^{N} V_{\mathrm{SAE}}\left(\sqrt{\left[\frac{X}{2}-x-r_j\sin\theta_j\right]^2+\left[\frac{Z}{2}+z+r_j\cos\theta_j\right]^2+a^2}\right). \end{aligned} \tag{4.18}$$

Clearly, there is no Z symmetry in this Hamiltonian since it changes after $Z \to -Z$. However, if we set $X = 0$, $x = 0$, or $z = 0$, and at the same time enforce an central symmetry of the system with respect to the origin (i.e., the center of mass), then there is Z symmetry in the Hamiltonian. We illustrate for a four-center system why this central symmetry is necessary. The corresponding

Hamiltonian for $X = 0$ is

$$
\begin{aligned}
H(x,0,z,Z;0) =& p_x^2 + p_z^2 + \frac{p_X^2 + p_Z^2}{4} + \frac{1}{\sqrt{(x_1-x_2)^2 + (z_1-z_2)^2 + b^2}} \\
&+ V_{\mathrm{SAE}}\left(\sqrt{[x - r_1\sin\theta_1]^2 + \left[\frac{Z}{2} + z - r_1\cos\theta_1\right]^2 + a^2}\right) \\
&+ V_{\mathrm{SAE}}\left(\sqrt{[x + r_1\sin\theta_1]^2 + \left[\frac{Z}{2} - z - r_1\cos\theta_1\right]^2 + a^2}\right) \\
&+ V_{\mathrm{SAE}}\left(\sqrt{[x - r_2\sin\theta_2]^2 + \left[\frac{Z}{2} + z - r_2\cos\theta_2\right]^2 + a^2}\right) \\
&+ V_{\mathrm{SAE}}\left(\sqrt{[x + r_2\sin\theta_2]^2 + \left[\frac{Z}{2} - z - r_2\cos\theta_2\right]^2 + a^2}\right) \\
&+ V_{\mathrm{SAE}}\left(\sqrt{[x - r_3\sin\theta_3]^2 + \left[\frac{Z}{2} + z - r_3\cos\theta_3\right]^2 + a^2}\right) \\
&+ V_{\mathrm{SAE}}\left(\sqrt{[x + r_3\sin\theta_3]^2 + \left[\frac{Z}{2} - z - r_3\cos\theta_3\right]^2 + a^2}\right) \\
&+ V_{\mathrm{SAE}}\left(\sqrt{[x - r_4\sin\theta_4]^2 + \left[\frac{Z}{2} + z - r_4\cos\theta_4\right]^2 + a^2}\right) \\
&+ V_{\mathrm{SAE}}\left(\sqrt{[x + r_4\sin\theta_4]^2 + \left[\frac{Z}{2} - z - r_4\cos\theta_4\right]^2 + a^2}\right),
\end{aligned}
\tag{4.19}
$$

which, after we change Z to $-Z$, becomes

$$\begin{aligned}
H'(x,0,z,Z;0) =& p_x^2 + p_z^2 + \frac{p_X^2 + p_Z^2}{4} + \frac{1}{\sqrt{(x_1-x_2)^2+(z_1-z_2)^2+b^2}} \\
&+ V_{\mathrm{SAE}}\left(\sqrt{[x - r_1\sin\theta_1]^2 + \left[\frac{Z}{2} - z + r_1\cos\theta_1\right]^2 + a^2}\right) \\
&+ V_{\mathrm{SAE}}\left(\sqrt{[x + r_1\sin\theta_1]^2 + \left[\frac{Z}{2} + z + r_1\cos\theta_1\right]^2 + a^2}\right) \\
&+ V_{\mathrm{SAE}}\left(\sqrt{[x - r_2\sin\theta_2]^2 + \left[\frac{Z}{2} - z + r_2\cos\theta_2\right]^2 + a^2}\right) \\
&+ V_{\mathrm{SAE}}\left(\sqrt{[x + r_2\sin\theta_2]^2 + \left[\frac{Z}{2} + z + r_2\cos\theta_2\right]^2 + a^2}\right) \\
&+ V_{\mathrm{SAE}}\left(\sqrt{[x - r_3\sin\theta_3]^2 + \left[\frac{Z}{2} - z + r_3\cos\theta_3\right]^2 + a^2}\right) \\
&+ V_{\mathrm{SAE}}\left(\sqrt{[x + r_3\sin\theta_3]^2 + \left[\frac{Z}{2} + z + r_3\cos\theta_3\right]^2 + a^2}\right) \\
&+ V_{\mathrm{SAE}}\left(\sqrt{[x - r_4\sin\theta_4]^2 + \left[\frac{Z}{2} - z + r_4\cos\theta_4\right]^2 + a^2}\right) \\
&+ V_{\mathrm{SAE}}\left(\sqrt{[x + r_4\sin\theta_4]^2 + \left[\frac{Z}{2} + z + r_4\cos\theta_4\right]^2 + a^2}\right).
\end{aligned} \tag{4.20}$$

The Hamiltonian remains unchanged if any of the following conditions is satisfied:

$$\boldsymbol{r}_1 = -\boldsymbol{r}_2, \quad \boldsymbol{r}_3 = -\boldsymbol{r}_4; \tag{4.21}$$

$$\boldsymbol{r}_1 = -\boldsymbol{r}_3, \quad \boldsymbol{r}_2 = -\boldsymbol{r}_4; \tag{4.22}$$

$$\boldsymbol{r}_1 = -\boldsymbol{r}_4, \quad \boldsymbol{r}_2 = -\boldsymbol{r}_3. \tag{4.23}$$

That is to say, the system has to have central symmetry relative to the origin (center of mass).

For systems consisting of an odd number of centers, such pairs as shown above do not exist. In this case, one atom has to be located at the origin. In a three-center system, for example, any

of the following conditions has to be satisfied:

$$\boldsymbol{r}_1 = 0, \quad \boldsymbol{r}_2 = -\boldsymbol{r}_3; \tag{4.24}$$

$$\boldsymbol{r}_2 = 0, \quad \boldsymbol{r}_1 = -\boldsymbol{r}_3; \tag{4.25}$$

$$\boldsymbol{r}_3 = 0, \quad \boldsymbol{r}_1 = -\boldsymbol{r}_2. \tag{4.26}$$

Then, the central symmetry is still necessary.

Indeed, the system does not have to be homogeneous as discussed above. For example, in the four-center system above, when the first condition, i.e.,

$$\boldsymbol{r}_1 = -\boldsymbol{r}_2, \quad \boldsymbol{r}_3 = -\boldsymbol{r}_4 \tag{4.27}$$

satisfies, we only need to require nucleus 1 and 2 to be the same and nucleus 3 and 4 to be the same separately. Here, again, the central symmetry is still valid.

Furthermore, our analysis above relies on a two-dimensional model for each of the electrons. However, it can be easily shown that our conclusions do not depend on this 2D analysis and are valid for real 3D cases as well. Molecules, such as C_{60}, have central symmetry. Therefore, the few-photon double ionization of C_{60} should also follow the same selection rules as in the case of simple atoms.

Note that the central symmetry is needed when the two active electrons are included as well as excluded, since both definite symmetries in the initial-state and the final-state Hamiltonians are necessary so that both initial-state and final-state wave functions possess definite symmetries. For molecules like C_6H_6 or C_{60}, the p electrons are delocalized, thus the selection rules apply when two p electrons are ionized if the remaining p electrons redistribute faster than the duration of the ionizing laser pulse. If the p electrons redistribute slower than the duration of the ionizing laser pulse, then the selection rules do not apply. In this sense, we may be able to map out the redistribution time of the p electrons by controlling the duration of the ionizing laser pulse. In contrast, if two s electrons are ionized from C_6H_6 or C_{60}, then the selection rules do not apply since the s electrons are localized.

Other interesting applications of the selection rules include determining the ionizing orbitals of the electrons in molecules like CO_2. If the two electrons are ionized from the different π bonds in the molecule, then the selection rules apply; while the selection rules do not apply in other cases, e.g., when they are ionized from the same π bond or when any of them is ionized from the σ bonds or any inner s orbital of the individual atoms in the molecule.

4.7 Summary

In summary, we showed that the well-known selection rules for single-photon double ionization can be generalized to the emission of two electrons following the simultaneous absorption of a few photons from an intense laser pulse. These selection rules, which arise due to the symmetries of the accessible final states in the two-electron continuum, correspond to nodes in the configuration space wave function and the correlated momentum distributions. In particular, the back-to-back emission of the two electrons with equal energy sharing is alternating either suppressed (forbidden) or non-suppressed as the number of absorbed photons increases. The theoretical predictions are tested well in numerical simulations. The numerical results for one- to four-photon double ionization of the helium atom clearly show the presence of the node in the back-to-back emission in the case of odd-number photon processes. Moreover, we showed that the presence of the selection rules does not depend on the numerical model. Furthermore, we have also shown that the same selection rules exist in the helium dimer, which is a diatomic molecule. Based on the studies of the homogeneous two-center molecules like the helium dimer, we further studied multicenter molecules in general, and found that the selection rules apply whenever the molecule has the central symmetry.

Chapter 5

Photoabsorption and correlation time delay

In this chapter, we propose a self-consistent-time method to account for the Coulomb-laser coupling effect and obtain the intrinsic photoabsorption time delay measured by the attosecond streak camera. We illustrate this method with a one dimensional numerical model of the hydrogen atom. The concept of the method is based on an iteration to obtain the photoabsorption time delay. Starting from an initial guess for this time delay, we iteratively obtain an improved time delay by using the classical trajectory calculations and comparison with the vector potential of the streaking pulse. We demonstrate the convergence and robustness of the self-consistent-time method, investigate the photoemission at different positions, and study the resonant two-photon ionization time delay.

Furthermore, we resolve the correlation time delay, defined as the delay between the absorption of the photon by the first electron (single ionization) and the transfer of the second electron into the continuum (double ionization) in a single-photon double-ionization process of the helium dimer via the variable space-partitioning method as well as the attosecond streaking technique, which is extended to many-electron systems. The streaked variable for the single ionization is the momentum of the first electron, while the streaked variable for the double ionization is the center-of-mass momentum of both electrons. The correlation time delays obtained for different laser parameters are compared with classical estimates.

5.1 Introduction

A recent report [120] on the photoemission time delay of 21 as from the $2s$ and $2p$ shells of the neon atom using the attosecond streak camera induced a vigorous debate among theoreticians about the origin of the time delay [121–140]. A large part of them was focused on the discussion concerning the role of the Wigner-Smith (WS) time delay [141, 142] in the photoionization, which itself diverges for long-range potentials like the Coulomb potential. Among others, our previous works [138–140] addressed the concern regarding the divergence of the observed time delays by showing that it can be written as a piecewise field-free time delays weighted by the ratio of the instantaneous streaking field strength relative to its strength at the instant of transition of the electron into continuum. The theoretical analysis was based on the agreement between results of *ab-initio* quantum-mechanical and classical-mechanical simulations of the propagation of the electron in the combined field of the Coulomb potential of the residual ion and the streaking laser field for the streaking time delay. This led to the interpretation of the measured time delay as due to the Coulomb-laser coupling effect, i.e., the coupled dynamics of the electron in the fields of the Coulomb potential and the streaking laser pulse.

In this chapter, we propose an alternative self-consistent-time (SCT) method to account for the Coulomb-laser coupling effect and obtain the intrinsic photoabsorption time delay measured by the attosecond streak camera. We illustrate this method using a one dimensional numerical model of the hydrogen atom. The concept of the method is based on an iteration to obtain the photoabsorption time delay. The convergence and robustness of the method is also demonstrated. Further, the photoemission at different positions and the resonant two-photon ionization time delay is studied as well.

Beyond the temporal resolution of single-electron processes, one next challenge in attosecond science is the real-time observation of energy exchange between electrons via their mutual correlation. The basic process to study energy exchange between electrons is the single-photon double ionization. At low photon energy, one electron (primary electron) absorbs the photon before its

energy is shared with the other electron via the Coulomb interaction $V_{\rm C}$ (refer to Sec. 3.4), and finally both electrons emit from the target together [see Fig. 5.6(a)]. The correlation time, over which the energy is exchanged, can be defined as the delay between the absorption of photon energy by the primary electron and the emission of both electrons, or equivalently, the time delay between single and double ionization. In this chapter, we further study the correlation time delay in the helium dimer via the variable space-partitioning method as well as the attosecond streaking technique. The correlation time delays obtained for different laser parameters are compared with classical estimates.

5.2 Photoabsorption time delay

In this section, we describe the one dimensional numerical model of the hydrogen atom used in the simulations and develop the SCT method.

5.2.1 Numerical model

To make the SCT scheme transparent, we use a one dimensional numerical model of the hydrogen atom with Hamiltonian

$$H = \frac{p^2}{2} + [E_{\rm XUV}(t) + E_{\rm s}(t)]x + V(x), \tag{5.1}$$

where

$$V(x) = -\frac{Z}{\sqrt{x^2 + a^2}} \tag{5.2}$$

is the Coulomb potential for the hydrogen atom with effective charge $Z = 1$ and soft-core parameter $a^2 = 2$, and $E_{\rm XUV}$ and $E_{\rm s}$ are the ionizing XUV laser field and streaking IR laser field, respectively, both of which are given in the form of

$$E(t) = \cos^2\left(\frac{\omega t}{2N}\right)\cos(\omega t + \phi), \tag{5.3}$$

where ω is the central frequency, N is the number of cycles, and ϕ is the carrier-envelope phase of the laser pulse, which is set to $-\pi/2$ in the present simulations.

The TDSE is numerically solved using the Crank–Nicolson method on a grid with $N = 200000$ points, a grid step of $\Delta x = 0.05$, and a time step of $\Delta t = 0.01$. The ground state energy of the model hydrogen atom is found to be $\varepsilon_0 = -0.500009$ under current conditions. In the simulations, the interaction with a 16-cycle XUV laser pulse at a central wavelength of 30 nm and a peak intensity of 5×10^{14} W/cm^2 and a 3-cycle IR laser pulse at a central wavelength of 2400 nm and a peak intensity of 1×10^{11} W/cm^2 is used. A streaking pulse of 2400 nm instead of 800 nm is used because we want to keep the XUV pulse shorter than one half period of the streaking pulse. We employ absorbing boundaries of the form $\cos^{1/6}\left(\frac{\pi}{2}\frac{|x-x_0|}{L}\right)$ with $|x| \geqslant |x_0|$, where x_0 denotes the border of the boundary region and L is its width. The boundary was chosen to span 10% of the grid size in each direction.

To obtain the streaking trace, we propagate the ionizing wave packet over long times and large distances until both laser fields cease and before the respective ionizing wave packet reaches the boundary. The momentum spectrum is obtained by applying the Fourier transform to the corresponding ionizing wave packet, which is well separated from the remaining bound state. We verified that the error due to the finite grid step and projection onto the plane wave is negligible.

5.2.2 The self-consistent-time method[1]

In this section, we present the framework of the SCT method. First, we detail the SCT scheme and illustrate it with a flowchart. Second, we show the convergence properties and robustness of the SCT method. Third, we study the cases where photoemission takes places at different positions other than the center of the hydrogen atom. Last, we study the resonant photoionization process, where an intrinsic photoabsorption time delay exists.

5.2.2.1 Scheme of the self-consistent-time method

To extract the final intrinsic photoabsorption time delay, we first obtain the streaking trace from the quantum-mechanical simulations. To this end, we scan the delay τ between the ionizing

[1] The results presented in this section are currently prepared for publication (H. Ni, J. Su, A. Becker, and A. Jaroń-Becker).

XUV laser pulse and the streaking IR laser pulse, and for each τ we obtain the momentum distribution of the ionizing wave packet after it has been propagated far away from the remaining bound state. Afterwards, the expectation value of the momentum distribution is obtained for each τ, which constitutes the quantum streaking trace $p^0(\tau)$. To minimize the error caused by finite propagation distances, we correct the quantum streaking trace $p^0(\tau)$ by calculating the asymptotic momentum via energy conservation based on the expectation value of the position of the corresponding ionizing wave packet.

Next we obtain the quantum time delay Δt^0 based on the quantum streaking trace $p^0(\tau)$ by fitting it to the vector potential A_s of the streaking laser field with fitting parameter α and temporal offset Δt_s,

$$p^{\mathrm{iter}}(\tau) = p_0 - \alpha A_\mathrm{s}(\tau + \Delta t^{\mathrm{iter}})/c, \tag{5.4}$$

where p_0 is the asymptotic momentum of the electron in the absence of the streaking laser field and c is the vacuum speed of light. This apparent measured quantum time delay Δt^0 can well be used as the initial guess for the intrinsic photoabsorption time delay, although it may include other contributions. At this moment, the Coulomb-laser coupling effect has not been taken into account from the apparent measured photoabsorption time delay and no SCT iteration has been implemented yet, and thus the superscript iter $= 0$, which tracks the number of iterations done, is used in notations $p^0(\tau)$ and Δt^0.

To obtain the momentum shift in the quantum streaking trace induced by the Coulomb-laser coupling effect, we classically propagate the electron in the combined Coulomb-laser fields using the Runge–Kutta method. To this end, we assume the photoemission takes place at the center of the hydrogen atom ($x_\mathrm{i} = 0$) with initial momentum

$$p_\mathrm{i} = \mathrm{sgn}(p_0)\sqrt{p_0^2 - 2V(x_\mathrm{i})} = \mathrm{sgn}(p_0)\sqrt{p_0^2 - 2V(0)}, \tag{5.5}$$

where p_0 is the asymptotic momentum of the electron in the absence of the streaking laser field, as mentioned before.

We propagate the electron classically in the combined field of the Coulomb potential of the

residual ion and the laser pulses, starting at instant

$$t_{\mathrm{i}}^{\mathrm{iter}}(\tau) = \tau + \Delta t^{\mathrm{iter}} \tag{5.6}$$

and end the calculation at the same time instant t_{f} as the quantum-mechanical calculation. After this we note the final position $x_{\mathrm{f}}^{\mathrm{iter}}(\tau)$ and final momentum $p_{\mathrm{f}}^{\mathrm{iter}}(\tau)$ of the electron. The parametric dependence of t_{i} on the XUV-IR delay τ implies that we need to repeat this calculation for each τ.

Now we repeat the classical propagation of the electron first in the case where there is only the streaking laser field during the same time span from $t_{\mathrm{i}}^{\mathrm{iter}}(\tau)$ to t_{f}, and then in the case where there is only the Coulomb potential within the same spatial extension from x_{i} to $x_{\mathrm{f}}^{\mathrm{iter}}(\tau)$, separately, after which the momentum shift in the quantum streaking trace induced by the Coulomb-laser coupling effect can be obtained by

$$\Delta p_{\mathrm{coupling}}^{\mathrm{iter}}(\tau) = \left[p_{\mathrm{f,IR+Coulomb}}^{\mathrm{iter}}(\tau) - p_{\mathrm{i}}\right] - \left[p_{\mathrm{f,IR}}^{\mathrm{iter}}(\tau) - p_{\mathrm{i}}\right] - \left[p_{\mathrm{f,Coulomb}}^{\mathrm{iter}}(\tau) - p_{\mathrm{i}}\right], \tag{5.7}$$

or equivalently,

$$\Delta p_{\mathrm{coupling}}^{\mathrm{iter}}(\tau) = p_{\mathrm{f,IR+Coulomb}}^{\mathrm{iter}}(\tau) + A[t_{\mathrm{i}}^{\mathrm{iter}}(\tau)] - \mathrm{sgn}(p_0)\sqrt{p_0^2 - 2V[x_{\mathrm{f}}^{\mathrm{iter}}(\tau)]}, \tag{5.8}$$

by taking advantage of the conservation of energy and canonical momentum and the fact that $A(t_{\mathrm{f}}) = 0$ since we end our propagations well after the end of the streaking pulse.

The improved streaking trace, where the Coulomb-laser coupling effect has been accounted for, can then be obtained as

$$p^{\mathrm{iter+1}}(\tau) = p^0(\tau) - \Delta p_{\mathrm{coupling}}^{\mathrm{iter}}(\tau). \tag{5.9}$$

Fitting this improved streaking trace to the vector potential of the streaking field again, an improved photoabsorption time delay $\Delta t^{\mathrm{iter+1}}$ results, which can be used as the next guessed photoabsorption time delay.

We repeat the iteration until $\Delta t^{\mathrm{iter+1}}$ and Δt^{iter} are approximately equal, the condition of which in the present simulations is

$$\left|\Delta t^{\mathrm{iter+1}} - \Delta t^{\mathrm{iter}}\right| \leqslant 1 \times 10^{-6}. \tag{5.10}$$

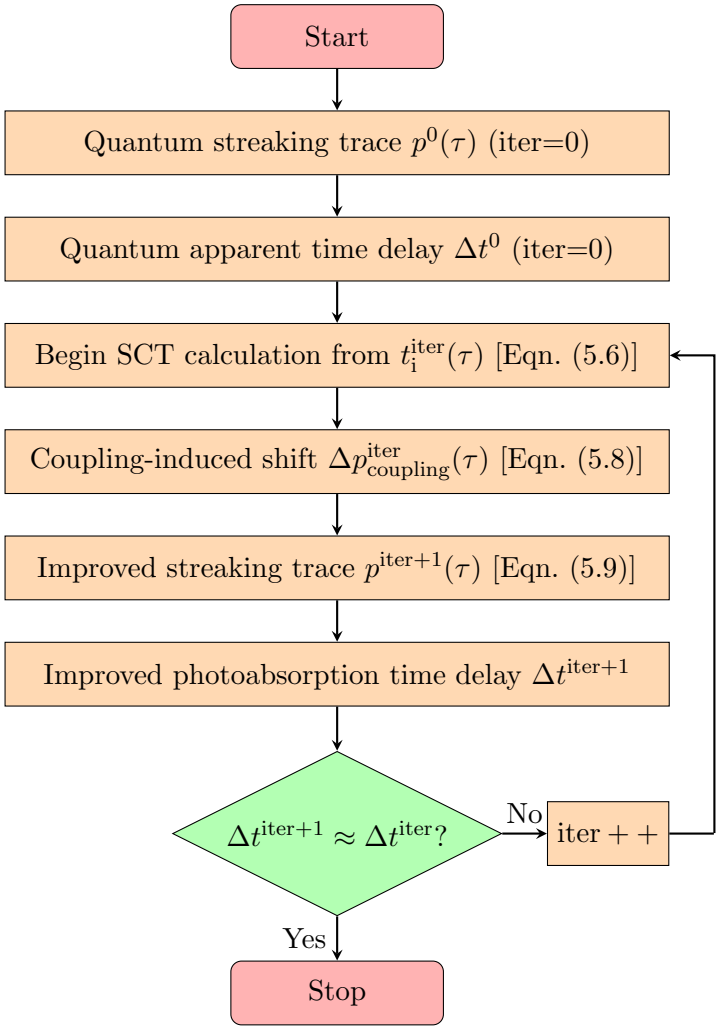

Figure 5.1. Flowchart of the self-consistent-time (SCT) method.

As soon as this condition is fulfilled, convergence within the chosen error bound is reached, and the final intrinsic photoabsorption time delay is achieved. We summarize the iteration procedure as a flowchart in Fig. 5.1.

5.2.2.2 Properties of the self-consistent-time method

We illustrate the iteration process by showing the streaking traces for the case of the one dimensional model hydrogen atom during the iteration. Shown in Fig. 5.2 are the streaking traces of the model hydrogen atom when exposed to a 16-cycle 30 nm XUV pulse with a peak intensity of 5×10^{14} W/cm^2 and a 3-cycle 2400 nm IR streaking pulse with a peak intensity of 1×10^{11} W/cm^2. The (blue) open circles are the expectation values of the momentum at different XUV-IR delay τ and the solid (red) lines are their fits to the vector potential of the streaking field. Small insets in the figures show the enlargements of the central part of the corresponding streaking trace from $\tau = -20$ to 20. Shown in panel (a) is the streaking trace before the SCT process, shown in panel (b) is the streaking trace after the first SCT iteration, and shown in panel (c) is the streaking trace after the last SCT iteration.

As can be seen in the insets of the figures, there is an apparent measured photoabsorption time delay for iter = 0, when no Coulomb-laser coupling effect has been taken into account, since the central part of the trace tilts towards one side. After one self-consistent iteration, this apparent time delay is already much reduced and hard to see, since the central trace is almost balanced on both sides. For the next three iterations, the apparent time delay reduces slightly to finally reach convergence within the present error bound for iter = 4.

Now, we illustrate the convergence process of the self-consistent iterations by extracting the time delay through fitting the streaking traces in Fig. 5.2 to the vector potential of the streaking laser field according to Eqn. (5.4). Shown in Fig. 5.3 are the fitted photoabsorption time delays for each iteration. The solid (red) line with open circles stands for the fitted time delay for emission to the positive direction, and the dashed (blue) line with open squares denotes that for emission to the negative direction. As it is obvious from the figure, the convergence is rapidly reached after

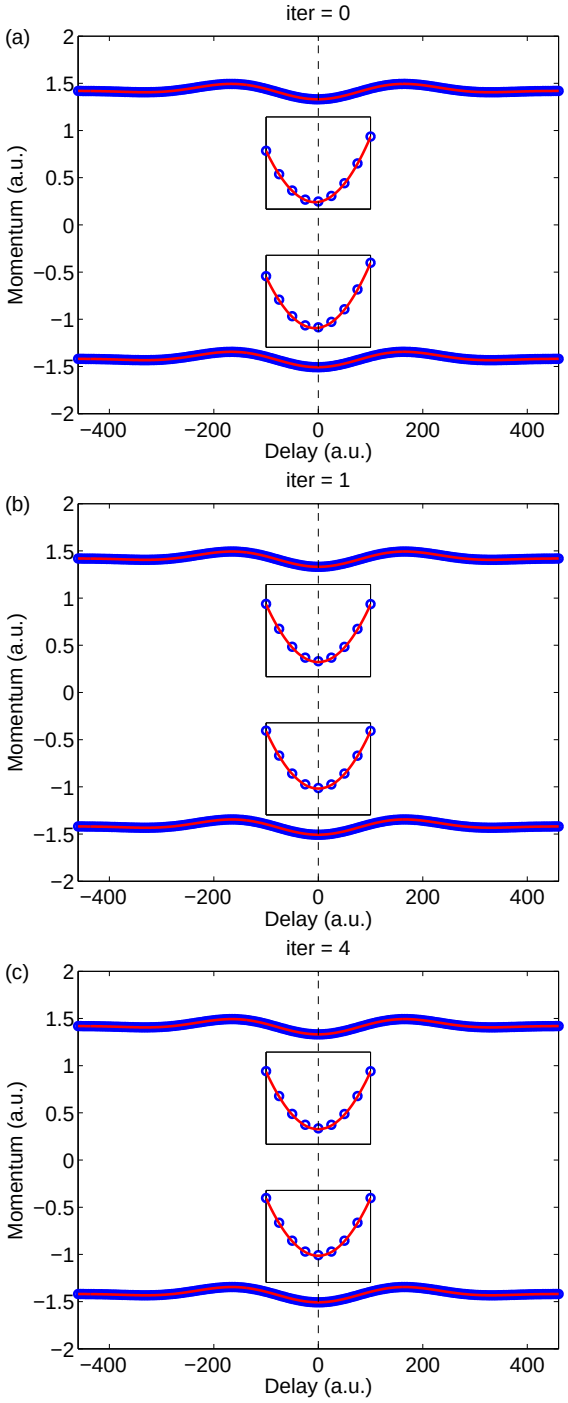

Figure 5.2. Iterations of the streaking trace of the one dimensional model hydrogen atom when exposed to a 16-cycle 30 nm XUV pulse with a peak intensity of 5×10^{14} W/cm^2 and a 3-cycle 2400 nm IR streaking pulse with a peak intensity of 1×10^{11} W/cm^2. The (blue) open circles are the expectation values of the momentum at different XUV-IR delay τ and the solid (red) lines are their fits to the vector potential of the streaking field. Small boxes in the figures are the enlargements of the central part of the corresponding streaking trace from $\tau = -20$ to 20. Shown in panel (a) is the streaking trace before any SCT iteration, shown in panel (b) is the streaking trace after the first SCT iteration, and shown in panel (c) is the streaking trace after the last SCT iteration.

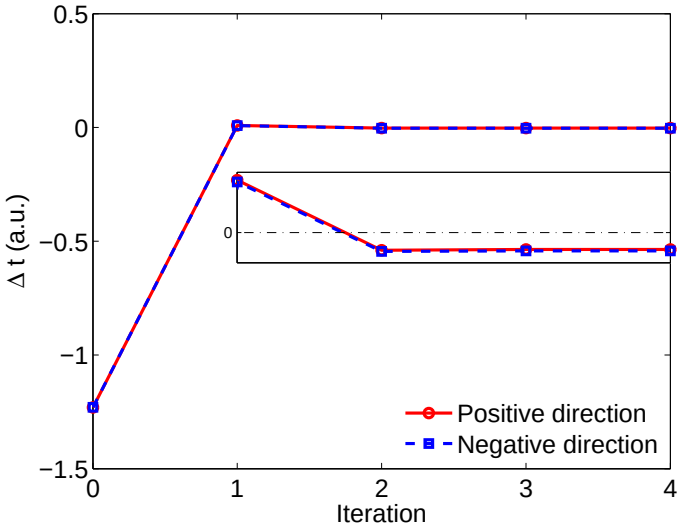

Figure 5.3. Convergence of the self-consistent iterations of the photoabsorption time delay of the one dimensional model hydrogen atom when exposed to a 16-cycle 30 nm XUV pulse with peak intensity of 5×10^{14} W/cm^2 and a 3-cycle 2400 nm IR streaking pulse with a peak intensity of 1×10^{11} W/cm^2. The solid (red) line with open circles stands for the fitted time delay for emission to the positive direction, and the dashed (blue) line with open squares denotes that for emission to the negative direction. The inset shows the extracted time delays for iterations 1 through 4 on a different scale.

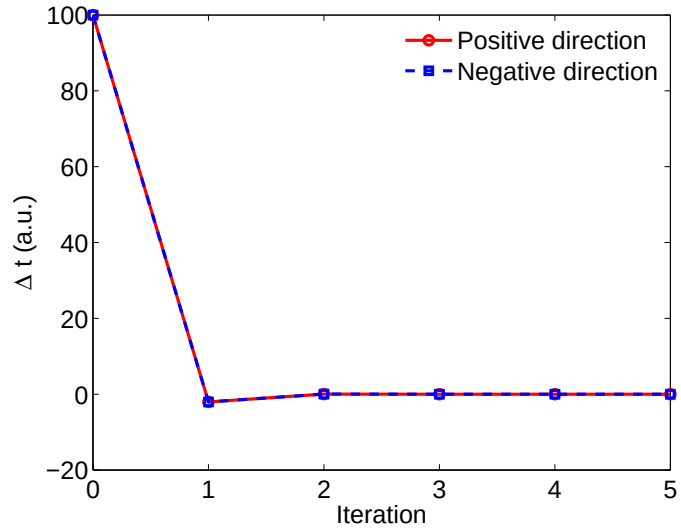

Figure 5.4. Robustness of the self-consistent-time (SCT) method of the photoabsorption time delay of the one dimensional model hydrogen atom when exposed to a 16-cycle 30 nm XUV pulse with 5×10^{14} W/cm^2 peak intensity and a 3-cycle 2400 nm IR streaking pulse with 1×10^{11} W/cm^2 peak intensity. The solid (red) line with open circles stands for the fitted time delay for emission to the positive direction, and the dashed (blue) line with open squares denotes that for emission to the negative direction.

only 4 iterations.

Next, we illustrate the robustness of the SCT method by deliberately using an obviously wrong initial time delay. Thus, instead of using the fitted photoabsorption time delay from the quantum streaking trace $p^0(\tau)$ as the initial guess for the time delay, we use a largely exaggerated wrong time delay as initial guess, and observe whether and how the convergence of the SCT method takes place. Shown in Fig. 5.4 are the fitted photoabsorption time delay for each iteration when an initial guess of 100 a.u. is taken. The solid (red) line with open circles stands for the fitted time delay for emission to the positive direction, and the dashed (blue) line with open squares denotes that for emission to the negative direction. Obviously, the iteration still rapidly converges to the correct intrinsic photoabsorption time delay despite of the large deviation of the initial guess from the correct value.

5.2.2.3 Different photoemission positions

Up to now, we have only considered the case when the photoemission takes place at the center of the atom, i.e., $x_\mathrm{i} = 0$. In this section, we remove this restriction by assuming different photoemission positions of the electron in the atom and repeat the SCT iterations for these different initial positions.

Shown in Fig. 5.5 are the converged photoabsorption time delays of the one dimensional model hydrogen atom when exposed to a 16-cycle 30 nm XUV pulse with 5×10^{14} W/cm^2 peak intensity and a 3-cycle 2400 nm IR streaking pulse with 1×10^{11} W/cm^2 peak intensity when the photoemission takes places at different positions x_i. The solid (red) line stands for the fitted time delay for emission to the positive direction, and the dashed (blue) line denotes that for emission to the negative direction. As obvious from the figure, there is no unique solution for the photoemission position and photoabsorption time. For each assumed photoemission position x_i, there is a corresponding photoabsorption time $t_\mathrm{i} = \tau + \Delta t$ that fulfills all the requirements.

However, if we demand that photoionization for emission to positive and negative directions has to occur at the same position due to the symmetry of the initial state, i.e., $x_\mathrm{i}^\mathrm{pos} = x_\mathrm{i}^\mathrm{neg}$, we find

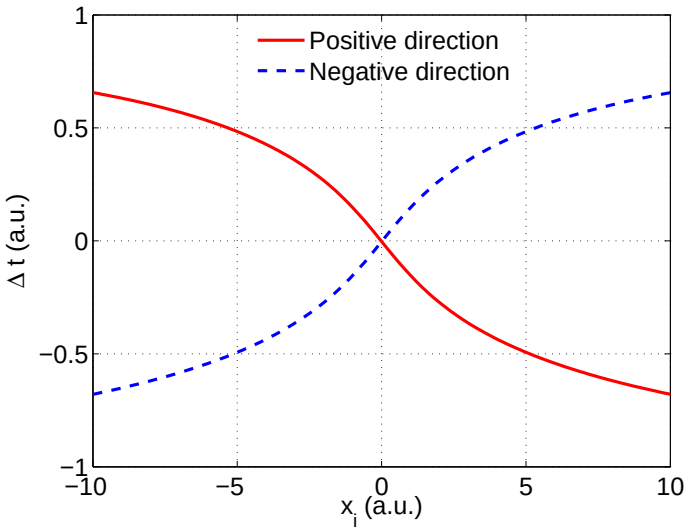

Figure 5.5. Converged photoabsorption time delays of the one dimensional model hydrogen atom when exposed to a 16-cycle 30 nm XUV pulse with 5×10^{14} W/cm^2 peak intensity and a 3-cycle 2400 nm IR streaking pulse with 1×10^{11} W/cm^2 peak intensity when the photoemission takes places at different positions x_i. The solid (red) line stands for the fitted time delay for emission to the positive direction, and the dashed (blue) line denotes that for emission to the negative direction.

that there is an unique solution, namely $\Delta t = -0.00291755 \approx 0$. On the other hand, if we demand that the photoionization for emission to positive and negative directions has the same time delay, i.e., $\Delta t^{\rm pos} = \Delta t^{\rm neg}$, we find that there is also an unique solution, namely $x_{\rm i} = 0.000706299 \approx 0$. While it is impossible to distinguish between all these non-unique solutions, it is straightforward from the physical sense that, $x_{\rm i} \approx 0$ and $\Delta t \approx 0$ is the most probable solution.

That said, we can still seek to do an ensemble average over the initial spatial distribution of the ground state of the hydrogen atom to take into account the possibility of photoemission at different positions. To this end, we associate a weight for the converged photoabsorption time delay at each $x_{\rm i}$ according to the probability of the initial state at that point. For the ground state of our 1D model, the averaged photoabsorption time delay can be shown to be $\Delta t^{\rm pos}_{\rm ave} = -0.0029164$ for emission to the positive direction and $\Delta t^{\rm neg}_{\rm ave} = -0.0031470$ for emission to the negative direction. If we further average over the emission to both directions, we have $\Delta t_{\rm ave} = -0.0030317$.

5.2.2.4 Resonant two-photon ionization time delay

In the previous sections, we have considered direct photoionization of the hydrogen atom where no intermediate state plays a role. Here, photoabsorption occurs instantaneously, and no intrinsic photoabsorption time delay is present. However, one may consider the case when an intermediate state plays a role, e.g., the resonant two-photon ionization, in which the absorption of the first photon promotes the electron to an excited state, and the absorption of the other photon ionizes the electron. If the electron absorbs the two photons in sequence, there might be a time delay between these steps [143].

In this section, we consider the resonant two-photon ionization of the Li^{2+} ion [143]. The reason to choose this ion is that it has larger energy gaps than the hydrogen atom and we can ensure that only one excited state participates in this process. For comparison, we also consider the case of nonresonant two-photon ionization of the same ion.

To this end, we use the same Coulomb potential as in Eqn. (5.2), but with an effective charge $Z = 3$ and soft-core parameter $a^2 = 0.15$. The ground-state energy, the first-excited-state energy,

Table 5.1. Two-photon ionization time delay for Li^{2+}

Case	$\Delta t_{\text{non-SCT}}$	Δt_{SCT}
Nonresonant	0.0050	−0.000059
Resonant	9.203688	9.135658

and the second-excited-state energy of the model ion are found to be $\varepsilon_0 = -5.31689$, $\varepsilon_1 = -2.31053$, and $\varepsilon_2 = -1.29547$, respectively, using the same grid parameters. In the simulations, the interaction with a 40-cycle XUV laser pulse at a central frequency of 3.51403 for the nonresonant case and a central frequency of 3.00636 for the resonant case (resonant with the first excited state starting from the ground state) and a peak intensity of 1×10^{13} W/cm^2 and a 3-cycle IR laser pulse at a central wavelength of 4800 nm and a peak intensity of 1×10^{11} W/cm^2 is used.

Listed in Tab. 5.1 are the two-photon ionization time delays in both cases of nonresonant and resonant two-photon ionization. The values are averaged over emissions to two directions. Shown are the time delays obtained from both the previous non-SCT method [138–140] and the SCT method. As can be seen from the table and it has been concluded by us recently [138–140], there is no intrinsic photoabsorption time delay if it is a nonresonant two-photon ionization process, in which no intermediate states are involved. On the other hand, if the XUV pulse is tuned to be in resonance with the first excited state of the model ion, there is an intrinsic time delay of about 9 a.u. This suggests that there might be a time delay between the absorption of the first and the second photon, i.e., the electron may stay at the first excited state for a while before absorbing another photon.

As for the accuracy of these two methods, the SCT method can be deemed as more accurate as it can be seen from the obtained time delay in nonresonant two-photon ionization. If we assume the accurate value of this time delay is 0, then the SCT method has an error of almost two orders lower than the previous non-SCT method. In the case of resonant two-photon ionization, the non-SCT method then has a relative error of 0.74%. Although it is not as accurate as the SCT method, the non-SCT method is still quite accurate considering this small error. For the detailed studies of

the resonant two-photon ionization time delay, interested readers are referred to Ref. [143].

5.3 Correlation time delay

In this section, we study the correlation time delay, which is the time delay for the two electrons to interact and exchange energy and be transferred to the continuum relative to the single ionization process, which is the first step of the knockout double photoionization process. To this end, we first discuss the method that employs the attosecond streak camera to streak the momentum of the primary electron in the first step, and streak the center-of-mass momentum of the two electrons in the second step, then we show the results of the correlation time delay.

5.3.1 Correlation time delay in the helium dimer

To time-resolve correlated electronic dynamics, it has been recently proposed [144] to extend the attosecond streak camera technique [42]. In the case of single ionization, the asymptotic momentum $\boldsymbol{p}_0$ of the electron freed at time instance t_s is shifted by a value proportional to the vector potential $\boldsymbol{A}$ of the infrared pulse at the release time t_s

$$\boldsymbol{p}_\mathrm{f} = \boldsymbol{p}_0 - \boldsymbol{A}(t_\mathrm{s})/c. \tag{5.11}$$

By varying the time delay between the triggering attosecond XUV pulse and the streaking infrared pulse, the time of ionization of the electron is mapped onto its final momentum distribution. We apply the attosecond streak camera technique to many-electron dynamics by noting that it is the center-of-mass electron momentum that couples to the external field [63, 145]. Thus, Eqn. (5.11) can be readily extended to many-electron dynamics by replacing the single-electron momentum by the center-of-mass momentum of the many-electron system:

$$\boldsymbol{P}_\mathrm{f} = \boldsymbol{P}_0 - Z\boldsymbol{A}(t_\mathrm{c})/c, \tag{5.12}$$

where t_c denotes the time of correlated emission of two or more electrons from the atom or molecule, and Z stands for the number of electrons in the many-electron ionization process. We may further

note that the center-of-mass electron momentum is often observed in experiments using the so-called COLTRIMS technique via the momentum of the recoil ion [55, 56].

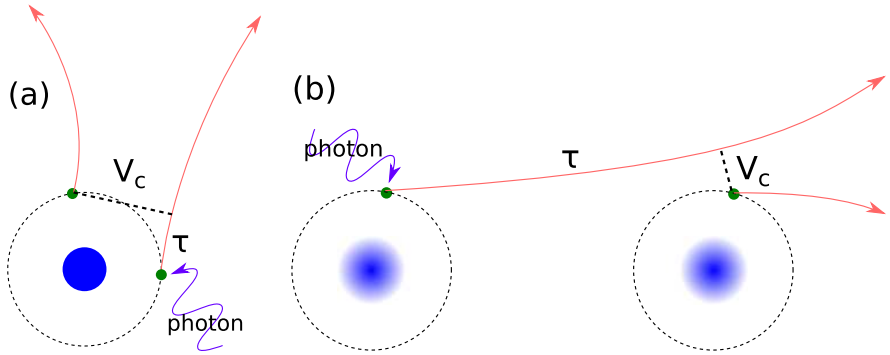

Figure 5.6. Scheme of the correlation time delay τ. V_c is the Coulomb correlation between the two electrons.

Theoretical time-delay analysis for correlated electron emission using the streaking technique have been previously done for the helium atom. Schemes based on measurements of the angle between the two escaping electrons [144] or the absolute quantum phase [146] have been analyzed. However, according to our analysis [147] the time delay between single and double ionization for two electrons in the ground state of helium atom is very small and hence difficult to resolve by the attosecond streak camera technique. Alternative scenarios, e.g., the correlated dynamics in the excited helium atom, which has been considered as well [144], are experimentally more difficult to realize since those are easily being ionized by the streaking pulse itself. Here, we propose an alternative to study the time delay of correlated electron emission in the helium dimer instead.

Due to the large separation between the atoms, dimers are ideal systems to study electron correlation over long distances [86, 89]. At low photon energies, double photoionization of the dimer proceeds by energy sharing over distances of approximately the internuclear distance of the dimer via the knockout mechanism [86, 89] [cf. Fig. 5.6(b)]. We therefore expect that in the dimer the time delay between photon absorption by the primary electron and transfer of part of the energy to the other electron is much larger than in the helium atom.

5.3.2 Correlation time delay in the planar 4D helium dimer

In order to study this problem, we employ the 4D planar model of the helium dimer with two active electrons located at separate atoms in the dimer (see Sec. 3.2).

5.3.2.1 Correlation time delay using attosecond streak camera

We employ the attosecond streaking camera technique to resolve the time delay within the double photoionization process. As mentioned above, we identify this delay as the temporal difference between the time instants of single and double ionization of the dimer. The time instants can be identified by streaking the single electron and the center-of-mass momenta of the electrons along the polarization direction of the streaking pulse, respectively [see Eqns. (5.11) and (5.12)]. The corresponding streaking signals are obtained by varying the time delay between the ionizing XUV pulse with respect to a 800 nm infrared streaking pulse (peak intensity of 5×10^{12} W/cm^2, a sin^2-shaped envelope, and a total of 3 cycles) and are shown in Fig. 5.7. To save computation time, only a scan of the time delay between the two pulses at the central streaking cycle is done. The white solid lines passing through the middle of the streaking signals correspond to the expectation values of the respective streaked momentum, which are fitted to the shape of the vector potential of the infrared streaking pulse as $p(t) = a + bA_{\mathrm{IR}}(t + \tau_{\mathrm{streak}})$, where a, b, and τ_{streak} are fitting parameters. One clearly sees a small, but observable shift between these two traces, which is the apparent measured time delay

$$\tau_{\mathrm{streak}} = \tau^{\mathrm{DI}}_{\mathrm{streak}} - \tau^{\mathrm{SI}}_{\mathrm{streak}}. \tag{5.13}$$

Note that the multiple peaks in the p_Z momentum distributions is due to the two-center interferences [64, 148–150] in the helium dimer, which may result in an inaccuracy in the obtained expectation value of the momentum.

As discussed above, this apparent time delay consists of two parts. The first part is the inherent (or intrinsic) time delay to the single and double ionization process, and the other part is the propagation time delay due to the Coulomb-laser-coupling effect because of the presence of the

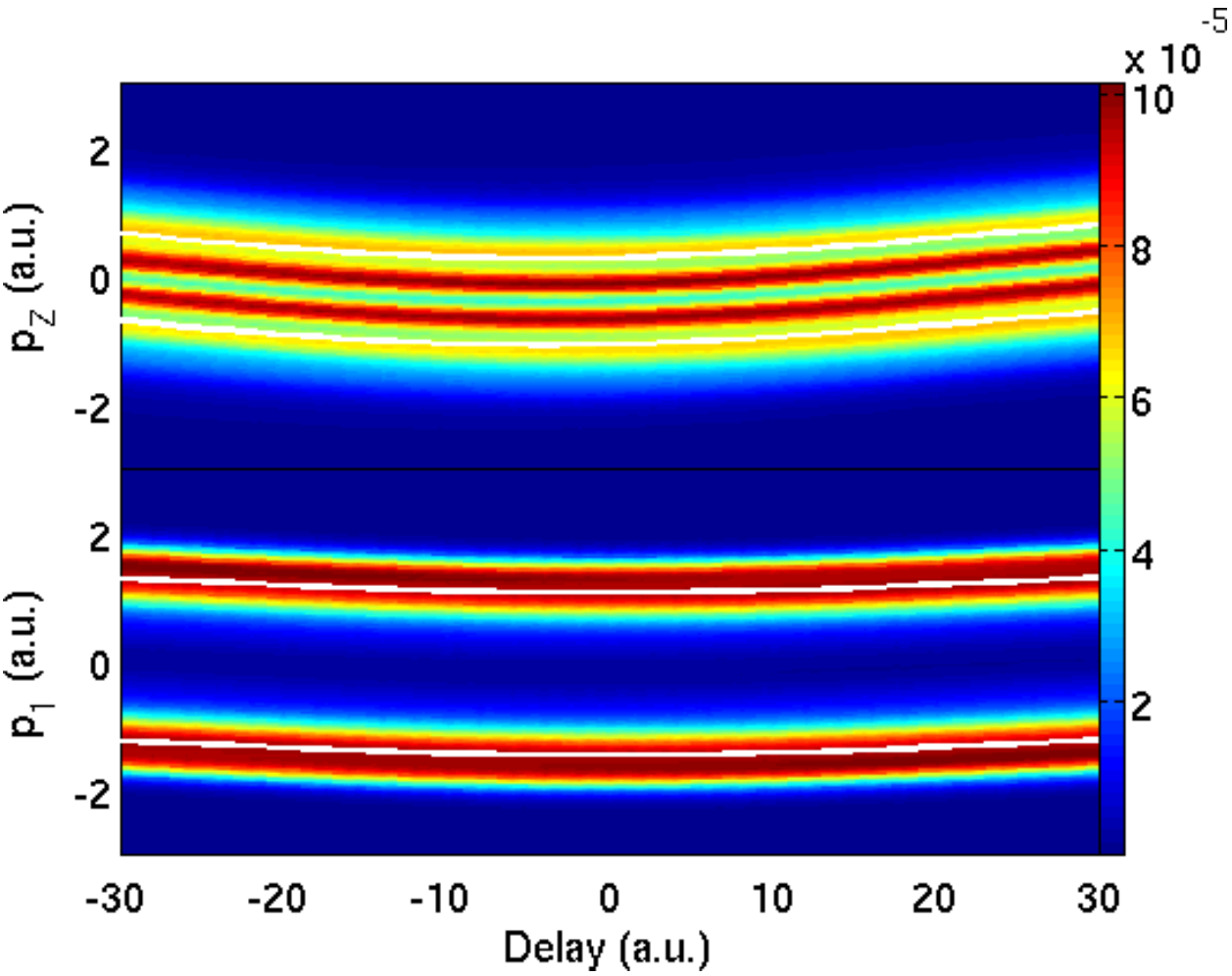

Figure 5.7. Central-cycle streaking signals for single and double ionization contributions of the parallel oriented helium dimer starting from the singlet ground state at $R = 5.6$ with a XUV laser pulse at a central wavelength of $\lambda_{\mathrm{XUV}} = 20$ nm and a peak intensity of 1×10^{14} W/cm^2.

Table 5.2. Correlation time delay for different R and λ_{XUV}

R (a.u.)	λ_{XUV} (nm)	$\tau_{\mathrm{classical}}$ (as)	$\tau_{\mathrm{evolution}}$ (as)	τ_{streak} (as)	$\tau_{\mathrm{extrapolate}}$ (as)
5.6	20	81.5	96.8	78.9	99.9
5.6	18	75.0	90.3	60.0	86.5
10.0	20	146	172	82.2	147

streaking laser field itself. This Coulomb-laser coupling effect is difficult to quantify in a two-center system and we may therefore, for now, assume that the coupling leads to similar propagation time delays for single and double ionization. Under this assumption, the effect would play a small role only in the difference

$$\begin{aligned}\tau_{\mathrm{correlation}} &= \tau^{\mathrm{DI}}_{\mathrm{correlation}} - \tau^{\mathrm{SI}}_{\mathrm{correlation}} = (\tau^{\mathrm{DI}}_{\mathrm{streak}} - \tau^{\mathrm{DI}}_{\mathrm{coupling}}) - (\tau^{\mathrm{SI}}_{\mathrm{streak}} - \tau^{\mathrm{SI}}_{\mathrm{coupling}}) \\ &= \tau_{\mathrm{streak}} - (\tau^{\mathrm{DI}}_{\mathrm{coupling}} - \tau^{\mathrm{SI}}_{\mathrm{coupling}}),\end{aligned} \tag{5.14}$$

and we get

$$\tau_{\mathrm{correlation}} \approx \tau_{\mathrm{streak}}. \tag{5.15}$$

Shown in Tab. 5.2 is the correlation time delay as a function of the wavelength of the XUV laser pulse and the internuclear distance of the dimer as compared to the classical time delay estimated by

$$\tau_{\mathrm{classical}} \approx \frac{R}{\sqrt{2(\omega_{\mathrm{XUV}} - I_p^+)}}, \tag{5.16}$$

where the denominator is just the classical velocity of the primary electron after its ionization, and another estimation $\tau_{\mathrm{evolution}}$ of the correlation time delay by observing the temporal evolution of the two-electron wave function as shown in Fig. 3.7. In this table, the streaking results are obtained by collecting the electrons emitted in every direction in space since the primary electron may get scattered to different directions from the neighboring atom and the center-of-mass momenta of the two electrons in the double ionization contribution can also be in different directions. The streaking results are averaged over the emission in $+z$ and $-z$ directions and we have also taken into account contributions from the singlet and triplet states by averaging according to their respective multiplicities.

As it is obvious from the table, the result for the configuration with $R = 10$ has a quite large discrepancy with the estimates, in part due to the difficulty in obtaining an accurate expectation values of p_Z and in part due to the difficulty in accounting for the Coulomb-laser-coupling induced propagation time delay in the continuum for this two-center system.

5.3.2.2 Correlation time delay using the variable space-partitioning method

Since it has been difficult to obtain the intrinsic correlation time delay from the attosecond streaking technique, here we instead use a more direct method to obtain the correlation time delay that we denote as the variable space-partitioning method, which is similar to the space-partitioning method that is used to obtain the single and double ionization contributions to the full wave function.

In this method the configuration space is partitioned into different regions like for the space-partitioning method in Sec. 2.7, and the probability entering the single ionization region is immediately regarded as single ionization, and the probability entering the double ionization region is immediately regarded as double ionization, as discussed in the second method in Sec. 2.8. With a pair of bounds d_{small} and d_{big} to partition the different regions, the single and double ionization yields are obtained as a function of propagation time according to the second method in Sec. 2.8. The ionization yields are differentiated with respect to the propagation time which yields ionization rates. The single and double ionization times are then defined as the maxima of the respective ionization rates.

In order to account for the variation due to the choice of the boundaries, we vary the pair of bounds d_{small} and d_{big} and extrapolate the respective ionization times to $d_{\text{small}} = 0$ and $d_{\text{big}} = 0$. To this end, we start from the base pair of bounds $d_{\text{small}} = 4$ and $d_{\text{big}} = 7$, and either increase d_{big} when d_{small} is fixed or increase d_{small} when d_{big} is fixed. In the first case, we increase d_{big} from 7 to 12 with step 1 when d_{small} is fixed at 4. Then we plot the single ionization yield and the corresponding ionization rate for each pair of bounds. Shown in Fig. 5.8 are the (a) single ionization yield and (b) single ionization rate, as a function of propagation time for different d_{big},

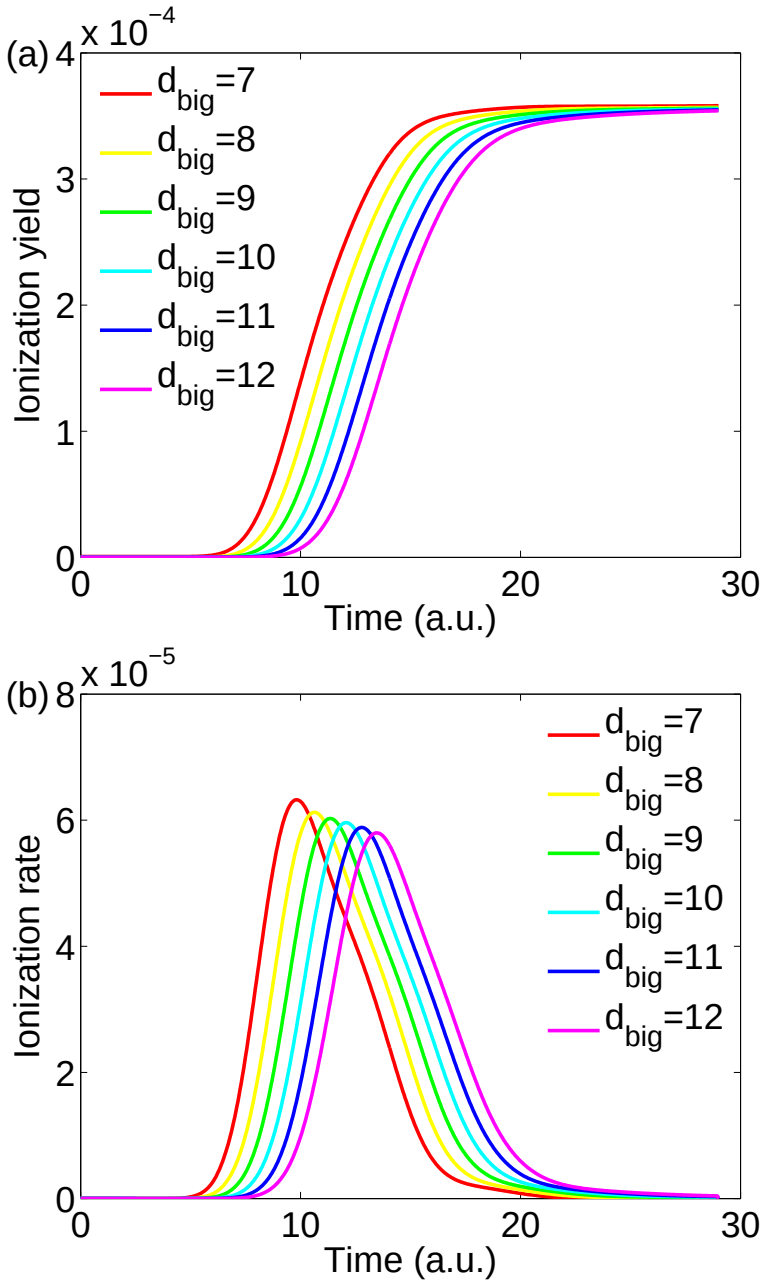

Figure 5.8. The (a) single ionization yield and (b) single ionization rate, as a function of propagation time for different d_{big}, of the parallel oriented singlet helium dimer at an internuclear distance of $R = 5.6$ when it is exposed to a linearly-polarized (in the direction of the dimer axis) 4-cycle XUV laser pulse with a central wavelength of 20 nm and a peak intensity of 1×10^{14} W/cm^2. Note that time 0 is defined as the beginning of the laser pulse here.

of the parallel oriented singlet helium dimer at an internuclear distance of $R = 5.6$ when it is exposed to a linearly-polarized (in the direction of the dimer axis) 4-cycle XUV laser pulse with a central wavelength of 20 nm and a peak intensity of 1×10^{14} W/cm^2. It can be clearly seen from the figure that, as d_{big} gets bigger, the ionization yield curve shifts to later times, and the corresponding peak of the ionization rate also shifts to later times. We can define the peak of the ionization rate as the respective ionization time and extrapolate to $d_{\text{big}} = 0$. Similarly, in the second case, we increase d_{small} from 4.5 to 7 with step 0.5 when d_{big} is fixed at 7, and the corresponding double ionization yield and rate can be obtained. Again, we identify the peak of the double ionization rate as the double ionization time and extrapolate to $d_{\text{small}} = 0$.

Shown in Fig. 5.9 is the single and double ionization time as a function of the partitioning bounds d_{big} and d_{small}. The values of t_{SI} and t_{DI} are obtained by using a linear fit to the data points and extrapolation to $d_{\text{big}} = 0$ and $d_{\text{small}} = 0$ respectively. In each panel, both singlet and triplet states are considered by obtaining the ionization time via averaging the ionization yield according to the multiplicities of the singlet and triplet states. The single ionization time as a function of d_{big} is shown in the left column and the double ionization time as a function of d_{small} is shown in the right column. Shown in the first row are the results for application of a 20 nm XUV laser pulse to a helium dimer at an internuclear distance of $R = 5.6$, shown in the second row are those for a 18 nm XUV laser pulse and a helium dimer at $R = 5.6$, and shown in the third row are those for a 20 nm XUV laser pulse and a helium dimer at $R = 10$. Other laser parameters are the same as in Fig. 5.8.

Note that no streaking laser field is used, and thus there is no Coulomb-laser-coupling-induced time delay here. Therefore, the values of t_{SI} and t_{DI} shown in the figure correspond to the intrinsic photoabsorption time. In Tab. 5.2 we list the correlation time delay, defined as the time delay between single and double ionization, obtained from extrapolation using the variable space-partitioning method $\tau_{\text{extrapolate}}$ and the time delay obtained from other methods. The results agree quite well, except those from the streaking method, in strong support of the knockout mechanism, for different internuclear distances R and XUV wavelengths λ_{XUV}. In particular, the time delay

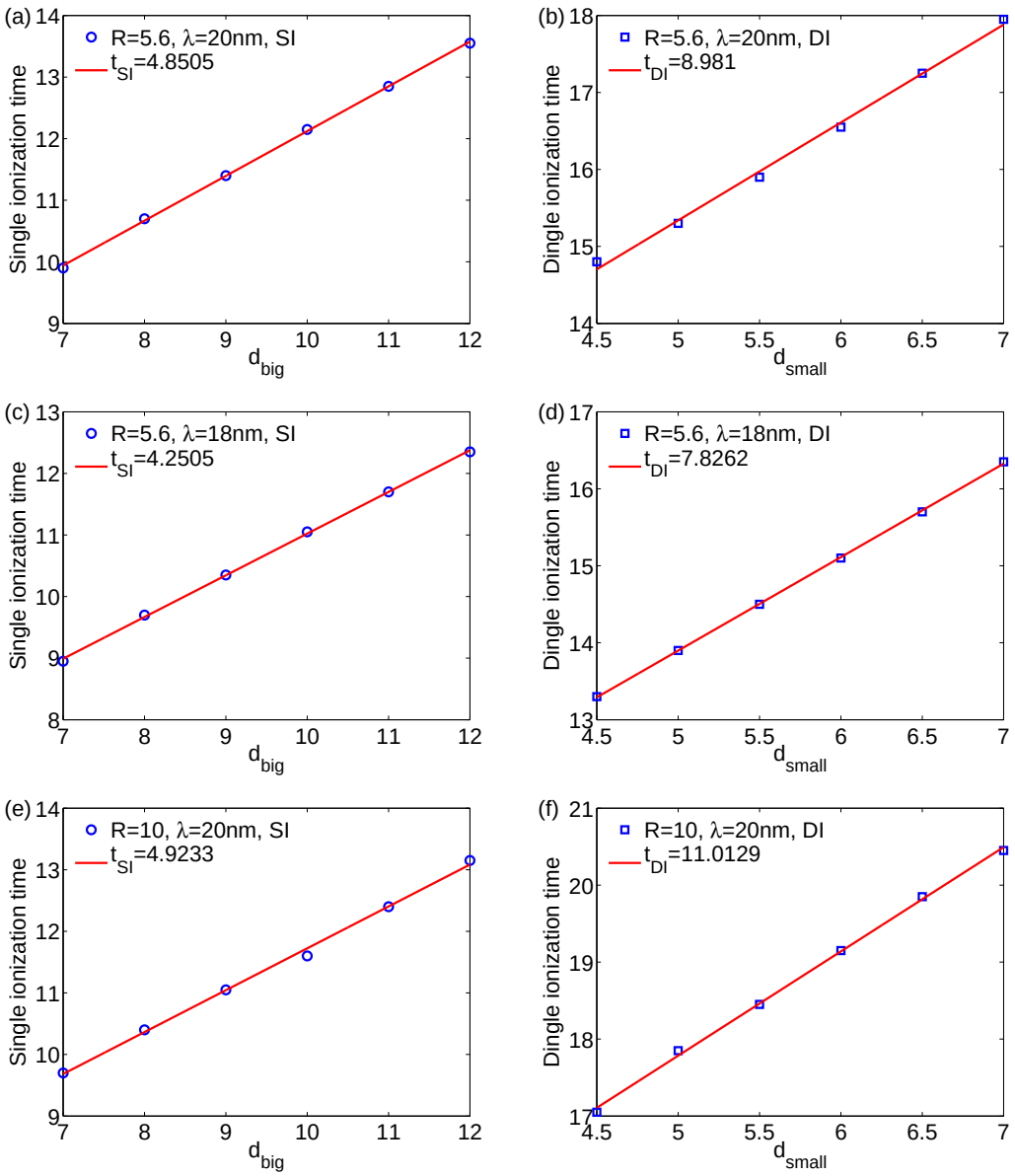

Figure 5.9. The single and double ionization time as a function of the partitioning bounds d_{big} and d_{small}. The values of t_{SI} and t_{DI} are obtained by using a linear fit to the data points and extrapolate to $d_{\text{big}} = 0$ and $d_{\text{small}} = 0$ respectively. In each panel, both singlet and triplet states are considered by obtaining the ionization time via averaging the ionization yield according to the multiplicities of the singlet and triplet states. The single ionization time as a function of d_{big} is shown in the left column and the double ionization time as a function of d_{small} is shown in the right column. Shown in the first row are the results for application of a 20 nm XUV laser pulse to a helium dimer at an internuclear distance of $R = 5.6$, shown in the second row are those for a 18 nm XUV laser pulse and a helium dimer at $R = 5.6$, and shown in the third row are those for a 20 nm XUV laser pulse and a helium dimer at $R = 10$. Other laser parameters are the same as in Fig. 5.8. Note that time 0 is defined as the beginning of the laser pulse here.

increases with either increase of the XUV wavelength or the internuclear distance R, consistent with the classical knockout mechanism.

5.4 Summary

As a summary, we propose a SCT method to account for the Coulomb-laser coupling effect and obtain the intrinsic photoionization time delay measured by the attosecond streak camera. This method is based on an iteration method. Convergence is reached when the time delay remains unchanged (within a given error bound) from one iteration to the next. We illustrated this method using a one dimensional numerical model for the hydrogen atom and the Li^{2+} ion. This SCT method features a rapid convergence, a robustness regarding initial guesses, and a better accuracy than the previous non-SCT method.

Furthermore, we studied the correlation time delay, which is the time delay for the two electrons to interact and exchange energy and is defined as the delay between the absorption of the photon (single ionization) and the emission of both electrons (double ionization), during single-photon double-ionization of the helium dimer using the attosecond streaking technique, which is extended to many-electron systems. The streaked variable for the single ionization is the momentum of the first electron, while the streaked variable for the double ionization is the center-of-mass momentum of both electrons. The correlation time delays obtained for different laser parameters are compared with classical estimates and the estimates from the temporal evolution of the two electrons. However, rather poor agreement between the results using the attosecond streak camera and the estimates was reached, due to the difficulty in accounting for the propagation time delay induced by the Coulomb-laser coupling effect in the two-center system. To circumvent this problem, we then used a more direct variable space-partitioning method to obtain the correlation time delay, from which a good agreement with the estimates was reached.

Chapter 6

Summary and perspective

This thesis is devoted to the theoretical studies and numerical simulations of ultrafast correlated electron dynamics in single and double photoionization of atoms and molecules. To this end, in Chapter 1, we gave a brief introduction to the background and some basic concepts of attosecond and strong-field physics, including the strong-field single and double ionization, HHG, and the attosecond streak camera technique. Next, in Chapter 2, we introduced the numerical methods used in this thesis to solve the TDSE in the grid representation. The numerical methods to obtain the ground state of a system and to propagate the initial state in a time-dependent potential, the absorbing boundaries, and the space-partitioning method that can be used to obtain single and double ionization contributions were presented. Strategies for parallel computation were also briefly discussed.

In Chapter 3, we studied the double photoionization of the helium dimer using the planar 4D model, in which the electron interacts and exchanges energy via their Coulomb correlation upon photon absorption over large distances. We first studied the different methods to obtain the photoelectron angular distribution and found that the theoretical results agree well with the experimental data if the momentum distribution is obtained by projection of the respective spatial wave function onto an approximate two-electron wave function that is a product of a Coulomb wave in their relative coordinates and a plane wave in their center-of-mass coordinates. We then studied the orientation and internuclear-distance dependence of the double-ionization probability and revealed that the mechanism of the low-photon-energy two-site double photoionization of the

helium dimer is the two-step knockout process. The knockout process was also evident from an analysis of the temporal evolution of the two-electron probability distribution.

We then introduced the Hamiltonian-reduction method to further study the effects of different interactions in the single and double photoionization of the helium dimer. First, we removed the interaction of the laser field with one electron. In this way, we were able to distinguish the primary and secondary electron in the knockout process. Next we studied the scattering of the primary electron by the neighboring atom by removing the interaction between the secondary electron and a nucleus and locating the two electrons at certain nuclei. We further found that the electron-nucleus interaction tends to focus the angular distribution to the direction of the dimer axis while the electron-electron interaction tends to diverge the distribution. Exchange ionization, in which the primary electron knocks out the other electron but gets captured itself, was also observed by removing the interaction of the laser field with one electron.

In Chapter 4, we analyzed the selection rules for the the emission of two electrons from the helium atom, the helium dimer, and general molecules following the absorption of a few photons in an intense laser field. We first examined the selection rules starting from the general studies of the two-electron continuum, the symmetry of the transition matrix, and the correlated KFR theory. Then, we introduced the restricted 3D model of the helium atom, and numerically studied the apparent nodes in the configuration and momentum space probability distributions and found that, in particular, the back-to-back emission of the two electrons for equal energy sharing is either suppressed or not depending on the number of photons absorbed from the laser field. In addition, we switched to a different planar 4D model of the helium atom and numerically studied part of the selection rules again and concluded that the presence of the selection rules do not depend on the specific numerical model used. Furthermore, we studied the selection rules in the helium dimer and revealed that the same selection rules applied to the helium dimer as well. As a step forward, we generalized the selection rules to general multicenter molecules and showed that the rules apply as long as the molecule has an central symmetry with respect to its center of mass.

In Chapter 5, we studied the photoabsorption time delay in the photoionization within a

model hydrogen atom and the correlation time delay in the double photoionization of the helium dimer. A SCT method was proposed to account for the Coulomb-laser coupling effect and obtain the intrinsic photoabsorption time delay measured by the attosecond streak camera. The SCT method started from an initial guess of the time delay, from which a streaking trace resulted, and a new iterated time delay can in turn be obtained. This process was continued until convergence was reached and the time delay intrinsic to the photoabsorption process was retrieved. The SCT method was demonstrated to be fast and robust in convergence. This method was also shown to work in the case of two-photon resonant photoionization process.

Finally, we attempted to resolve the correlation time delay in the double photoionization process of the helium dimer using a planar 4D model. The attosecond streaking technique was used for this purpose, which was extended to many-electron systems. However, the agreement of the time delay to classical estimates and the estimates from the temporal evolution of the two-electron wave function was insufficient due to the difficulty in accounting for the Coulomb-laser coupling effect and obtaining the intrinsic correlation time delay in this two-center system. As an alternative, we used a variable space-partitioning method, which directly monitors the ionizing wave packet, and were able to obtain a correlation time delay that was close to the estimates.

Bibliography

[1] P. F. Moulton, Journal of the Optical Society of America B **3**, 125 (1986).

[2] A. H. Zewail, Angewandte Chemie International Edition **39**, 2586 (2000).

[3] F. Krausz and M. Ivanov, Reviews of Modern Physics **81**, 163 (2009).

[4] L. V. Keldysh, Soviet Physics JETP **20**, 1307 (1965).

[5] R. Dörner, H. Schmidt-Böcking, T. Weber, T. Jahnke, M. Schöffler, A. Knapp, M. Hattass, A. Czasch, L. Ph. H. Schmidt, and O. Jagutzki, Radiation Physics and Chemistry **70**, 191 (2004).

[6] W. Becker, X. Liu, P. J. Ho, and J. H. Eberly, Reviews of Modern Physics **84**, 1011 (2012).

[7] J. A. R. Samson, Physical Review Letters **65**, 2861 (1990).

[8] A. Kheifets, Journal of Physics B: Atomic, Molecular and Optical Physics **34**, L247 (2001).

[9] D. N. Fittinghoff, P. R. Bolton, B. Chang, and K. C. Kulander, Physical Review Letters **69**, 2642 (1992).

[10] T. Schneider, P. L. Chocian, and J.-M. Rost, Physical Review Letters **89**, 073002 (2002).

[11] K. J. Schafer, B. Yang, L. F. DiMauro, and K. C. Kulander, Physical Review Letters **70**, 1599 (1993).

[12] P. B. Corkum, Physical Review Letters **71**, 1994 (1993).

[13] J. L. Krause, K. J. Schafer, and K. C. Kulander, Physical Review Letters **68**, 3535 (1992).

[14] J. J. Macklin, J. D. Kmetec, and C. L. Gordon, Physical Review Letters **70**, 766 (1993).

[15] T. Popmintchev, M.-C. Chen, P. Arpin, M. M. Murnane, and H. C. Kapteyn, Nature Photonics **4**, 822 (2010).

[16] M. F. Kling and M. J. Vrakking, Annual Review of Physical Chemistry **59**, 463 (2008).

[17] S. T. Cundiff, Nature Physics **3**, 16 (2007).

[18] M. Lewenstein, P. Balcou, M. Y. Ivanov, A. L'Huillier, and P. B. Corkum, Physical Review A **49**, 2117 (1994).

[19] I. P. Christov, M. M. Murnane, and H. C. Kapteyn, Physical Review Letters **78**, 1251 (1997).

[20] K. J. Schafer and K. C. Kulander, Physical Review Letters **78**, 638 (1997).

[21] M. Hentschel, R. Kienberger, C. Spielmann, G. A. Reider, N. Milosevic, T. Brabec, P. Corkum, U. Heinzmann, M. Drescher, and F. Krausz, Nature **414**, 509 (2001).

[22] M. Drescher, M. Hentschel, R. Kienberger, G. Tempea, C. Spielmann, G. A. Reider, P. B. Corkum, and F. Krausz, Science **291**, 1923 (2001).

[23] A. Baltuska, T. Udem, M. Uiberacker, M. Hentschel, E. Goulielmakis, C. Gohle, R. Holzwarth, V. S. Yakovlev, A. Scrinzi, T. W. Hansch, and F. Krausz, Nature **421**, 611 (2003).

[24] R. Kienberger, E. Goulielmakis, M. Uiberacker, A. Baltuska, V. Yakovlev, F. Bammer, A. Scrinzi, T. Westerwalbesloh, U. Kleineberg, U. Heinzmann, M. Drescher, and F. Krausz, Nature **427**, 817 (2004).

[25] H. C. Kapteyn, M. M. Murnane, and I. P. Christov, Physics Today **58**, 39 (2005).

[26] J.-F. Hergott, M. Kovacev, H. Merdji, C. Hubert, Y. Mairesse, E. Jean, P. Breger, P. Agostini, B. Carré, and P. Salières, Physical Review A **66**, 021801 (2002).

[27] P. B. Corkum, N. H. Burnett, and M. Y. Ivanov, Optics Letters **19**, 1870 (1994).

[28] M. Kovacev, Y. Mairesse, E. Priori, H. Merdji, O. Tcherbakoff, P. Monchicourt, P. Breger, E. Mével, E. Constant, P. Saliéres, B. Carré, and P. Agostini, The European Physical Journal D - Atomic, Molecular, Optical and Plasma Physics **26**, 79 (2003).

[29] I. J. Sola, E. Mevel, L. Elouga, E. Constant, V. Strelkov, L. Poletto, P. Villoresi, E. Benedetti, J.-P. Caumes, S. Stagira, C. Vozzi, G. Sansone, and M. Nisoli, Nature Physics **2**, 319 (2006).

[30] G. Sansone, E. Benedetti, F. Calegari, C. Vozzi, L. Avaldi, R. Flammini, L. Poletto, P. Villoresi, C. Altucci, R. Velotta, S. Stagira, S. De Silvestri, and M. Nisoli, Science **314**, 443 (2006).

[31] P. Tzallas, E. Skantzakis, C. Kalpouzos, E. P. Benis, G. D. Tsakiris, and D. Charalambidis, Nature Physics **3**, 846 (2007).

[32] C. Siedschlag, H. G. Muller, and M. Vrakking, Laser Physics **15**, 916 (2005).

[33] G. D. Tsakiris, K. Eidmann, J. Meyer-ter Vehn, and F. Krausz, New Journal of Physics **8**, 19 (2006).

[34] F. Quéré, C. Thaury, P. Monot, S. Dobosz, P. Martin, J.-P. Geindre, and P. Audebert, Physical Review Letters **96**, 125004 (2006).

[35] B. Dromey, M. Zepf, A. Gopal, K. Lancaster, M. S. Wei, K. Krushelnick, M. Tatarakis, N. Vakakis, S. Moustaizis, R. Kodama, M. Tampo, C. Stoeckl, R. Clarke, H. Habara, D. Neely, S. Karsch, and P. Norreys, Nature Physics **2**, 456 (2006).

[36] C. A. Haworth, L. E. Chipperfield, J. S. Robinson, P. L. Knight, J. P. Marangos, and J. W. G. Tisch, Nature Physics **3**, 52 (2007).

[37] V. T. Platonenko, V. V. Strelkov, and F. V. Ignatovich, Quantum Electronics **29**, 601 (1999).

[38] I. Christov, H. Kapteyn, and M. Murnane, Optics Express **7**, 362 (2000).

[39] I. Thomann, A. Bahabad, X. Liu, R. Trebino, M. M. Murnane, and H. C. Kapteyn, Optics Express **17**, 4611 (2009).

[40] M.-C. Chen, C. Hernández-García, C. Mancuso, F. Dollar, B. Galloway, D. Popmintchev, P.-C. Huang, B. Walker, L. Plaja, A. Jaroń-Becker, A. Becker, T. Popmintchev, M. M. Murnane, and H. C. Kapteyn, arXiv:1401.0240 [physics] (2013).

[41] L. Gallmann, C. Cirelli, and U. Keller, Annual Review of Physical Chemistry **63**, 447 (2012).

[42] J. Itatani, F. Quéré, G. L. Yudin, M. Y. Ivanov, F. Krausz, and P. B. Corkum, Physical Review Letters **88**, 173903 (2002).

[43] P. Eckle, A. N. Pfeiffer, C. Cirelli, A. Staudte, R. Dörner, H. G. Muller, M. Büttiker, and U. Keller, Science **322**, 1525 (2008).

[44] M. Uiberacker, T. Uphues, M. Schultze, A. J. Verhoef, V. Yakovlev, M. F. Kling, J. Rauschenberger, N. M. Kabachnik, H. Schröder, M. Lezius, K. L. Kompa, H.-G. Muller, M. J. J. Vrakking, S. Hendel, U. Kleineberg, U. Heinzmann, M. Drescher, and F. Krausz, Nature **446**, 627 (2007).

[45] A. L. Cavalieri, N. Müller, T. Uphues, V. S. Yakovlev, A. Baltuška, B. Horvath, B. Schmidt, L. Blümel, R. Holzwarth, S. Hendel, M. Drescher, U. Kleineberg, P. M. Echenique, R. Kienberger, F. Krausz, and U. Heinzmann, Nature **449**, 1029 (2007).

[46] E. Goulielmakis, Z.-H. Loh, A. Wirth, R. Santra, N. Rohringer, V. S. Yakovlev, S. Zherebtsov, T. Pfeifer, A. M. Azzeer, M. F. Kling, S. R. Leone, and F. Krausz, Nature **466**, 739 (2010).

[47] M. Odenweller, N. Takemoto, A. Vredenborg, K. Cole, K. Pahl, J. Titze, L. P. H. Schmidt, T. Jahnke, R. Dörner, and A. Becker, Physical Review Letters **107**, 143004 (2011).

[48] E. Goulielmakis, M. Uiberacker, R. Kienberger, A. Baltuska, V. Yakovlev, A. Scrinzi, T. Westerwalbesloh, U. Kleineberg, U. Heinzmann, M. Drescher, and F. Krausz, Science **305**, 1267 (2004).

[49] D. Bradley, B. Liddy, and W. Sleat, Optics Communications **2**, 391 (1971).

[50] M. Y. Schelev, M. C. Richardson, and A. J. Alcock, Applied Physics Letters **18**, 354 (1971).

[51] J. S. Briggs and V. Schmidt, Journal of Physics B: Atomic, Molecular and Optical Physics **33**, R1 (2000).

[52] W. Ackermann et al., Nature Photonics **1**, 336 (2007).

[53] T. Shintake, H. Tanaka, T. Hara, T. Tanaka, K. Togawa, M. Yabashi, Y. Otake, Y. Asano, T. Bizen, T. Fukui, S. Goto, A. Higashiya, T. Hirono, N. Hosoda, T. Inagaki, S. Inoue, M. Ishii, Y. Kim, H. Kimura, M. Kitamura, T. Kobayashi, H. Maesaka, T. Masuda, S. Matsui, T. Matsushita, X. Maréchal, M. Nagasono, H. Ohashi, T. Ohata, T. Ohshima, K. Onoe, K. Shirasawa, T. Takagi, S. Takahashi, M. Takeuchi, K. Tamasaku, R. Tanaka, Y. Tanaka, T. Tanikawa, T. Togashi, S. Wu, A. Yamashita, K. Yanagida, C. Zhang, H. Kitamura, and T. Ishikawa, Nature Photonics **2**, 555 (2008).

[54] P. Emma, R. Akre, J. Arthur, R. Bionta, C. Bostedt, J. Bozek, A. Brachmann, P. Bucksbaum, R. Coffee, F.-J. Decker, Y. Ding, D. Dowell, S. Edstrom, A. Fisher, J. Frisch, S. Gilevich, J. Hastings, G. Hays, P. Hering, Z. Huang, R. Iverson, H. Loos, M. Messerschmidt, A. Miahnahri, S. Moeller, H.-D. Nuhn, G. Pile, D. Ratner, J. Rzepiela, D. Schultz, T. Smith, P. Stefan, H. Tompkins, J. Turner, J. Welch, W. White, J. Wu, G. Yocky, and J. Galayda, Nature Photonics **4**, 641 (2010).

[55] R. Dörner, V. Mergel, O. Jagutzki, L. Spielberger, J. Ullrich, R. Moshammer, and H. Schmidt-Böcking, Physics Reports **330**, 95 (2000).

[56] J. Ullrich, R. Moshammer, A. Dorn, R. Dörner, L. P. H. Schmidt, and H. Schmidt-Böcking, Reports on Progress in Physics **66**, 1463 (2003).

[57] T. N. Rescigno, M. Baertschy, W. A. Isaacs, and C. W. McCurdy, Science **286**, 2474 (1999).

[58] H. Bachau, E. Cormier, P. Decleva, J. E. Hansen, and F. Martín, Reports on Progress in Physics **64**, 1815 (2001).

[59] R. Wehlitz, F. Heiser, O. Hemmers, B. Langer, A. Menzel, and U. Becker, Physical Review Letters **67**, 3764 (1991).

[60] O. Schwarzkopf, B. Krässig, J. Elmiger, and V. Schmidt, Physical Review Letters **70**, 3008 (1993).

[61] F. Maulbetsch and J. S. Briggs, Journal of Physics B: Atomic, Molecular and Optical Physics **26**, 1679 (1993).

[62] A. S. Kheifets and I. Bray, Journal of Physics B: Atomic, Molecular and Optical Physics **31**, L447 (1998).

[63] C. Ruiz, L. Plaja, L. Roso, and A. Becker, Physical Review Letters **96**, 053001 (2006).

[64] D. Akoury, K. Kreidi, T. Jahnke, T. Weber, A. Staudte, M. Schoffler, N. Neumann, J. Titze, L. P. H. Schmidt, A. Czasch, O. Jagutzki, R. A. C. Fraga, R. E. Grisenti, R. D. Muino, N. A. Cherepkov, S. K. Semenov, P. Ranitovic, C. L. Cocke, T. Osipov, H. Adaniya, J. C. Thompson, M. H. Prior, A. Belkacem, A. L. Landers, H. Schmidt-Bocking, and R. Dorner, Science **318**, 949 (2007).

[65] R. Dörner, H. Bräuning, O. Jagutzki, V. Mergel, M. Achler, R. Moshammer, J. M. Feagin, T. Osipov, A. Bräuning-Demian, L. Spielberger, J. H. McGuire, M. H. Prior, N. Berrah, J. D. Bozek, C. L. Cocke, and H. Schmidt-Böcking, Physical Review Letters **81**, 5776 (1998).

[66] C. Siedschlag and T. Pattard, Journal of Physics B: Atomic, Molecular and Optical Physics **38**, 2297 (2005).

[67] W. Vanroose, D. A. Horner, F. Martín, T. N. Rescigno, and C. W. McCurdy, Physical Review A **74**, 052702 (2006).

[68] S. Baier, C. Ruiz, L. Plaja, and A. Becker, Physical Review A **74**, 033405 (2006).

[69] J. Colgan, M. S. Pindzola, and F. Robicheaux, Physical Review Letters **98**, 153001 (2007).

[70] Y. Nabekawa, H. Hasegawa, E. J. Takahashi, and K. Midorikawa, Physical Review Letters **94**, 043001 (2005).

[71] M. Kurka, J. Feist, D. A. Horner, A. Rudenko, Y. H. Jiang, K. U. Kühnel, L. Foucar, T. N. Rescigno, C. W. McCurdy, R. Pazourek, S. Nagele, M. Schulz, O. Herrwerth, M. Lezius, M. F. Kling, M. Schöffler, A. Belkacem, S. Düsterer, R. Treusch, B. I. Schneider, L. A. Collins, J. Burgdörfer, C. D. Schröter, R. Moshammer, and J. Ullrich, New Journal of Physics **12**, 073035 (2010).

[72] A. Rudenko, Y. H. Jiang, M. Kurka, K. U. Kühnel, L. Foucar, O. Herrwerth, M. Lezius, M. F. Kling, C. D. Schröter, R. Moshammer, and J. Ullrich, Journal of Physics B: Atomic, Molecular and Optical Physics **43**, 194004 (2010).

[73] A. Becker, R. Dörner, and R. Moshammer, Journal of Physics B: Atomic, Molecular and Optical Physics **38**, S753 (2005).

[74] T. Hartman, P. N. Juranić, K. Collins, B. Reilly, N. Appathurai, and R. Wehlitz, Physical Review Letters **108**, 023001 (2012).

[75] J. Crank and P. Nicolson, Advances in Computational Mathematics **6**, 207 (1996).

[76] W. H. Press, S. A. Teukolsky, W. T. Vetterling, and B. P. Flannery, Numerical recipes, 3rd ed. (Cambridge University Press, 2007).

[77] R. Kosloff and H. Tal-Ezer, Chemical Physics Letters **127**, 223 (1986).

[78] M. D. Feit, J. A. Fleck Jr., and A. Steiger, Journal of Computational Physics **47**, 412 (1982).

[79] J. L. Krause, K. J. Schafer, and K. C. Kulander, Physical Review A **45**, 4998 (1992).

[80] C. W. McCurdy, M. Baertschy, and T. N. Rescigno, Journal of Physics B: Atomic, Molecular and Optical Physics **37**, R137 (2004).

[81] F. He, C. Ruiz, and A. Becker, Physical Review A **75**, 053407 (2007).

[82] U. V. Riss and H.-D. Meyer, Journal of Physics B: Atomic, Molecular and Optical Physics **26**, 4503 (1993).

[83] R. Santra and L. S. Cederbaum, Physics Reports **368**, 1 (2002).

[84] J. G. Muga, J. P. Palao, B. Navarro, and I. L. Egusquiza, Physics Reports **395**, 357 (2004).

[85] J. S. Parker, B. J. S. Doherty, K. J. Meharg, and K. T. Taylor, Journal of Physics B: Atomic, Molecular and Optical Physics **36**, L393 (2003).

[86] H. Ni, C. Ruiz, R. Dörner, and A. Becker, Physical Review A **88**, 013407 (2013).

[87] H. Ni and A. Becker, Physical Review A **89**, 033402 (2014).

[88] T. Havermeier, T. Jahnke, K. Kreidi, R. Wallauer, S. Voss, M. Schöffler, S. Schössler, L. Foucar, N. Neumann, J. Titze, H. Sann, M. Kühnel, J. Voigtsberger, J. H. Morilla, W. Schöllkopf, H. Schmidt-Böcking, R. E. Grisenti, and R. Dörner, Physical Review Letters **104**, 133401 (2010).

[89] T. Havermeier, T. Jahnke, K. Kreidi, R. Wallauer, S. Voss, M. Schöffler, S. Schössler, L. Foucar, N. Neumann, J. Titze, H. Sann, M. Kühnel, J. Voigtsberger, A. Malakzadeh, N. Sisourat, W. Schöllkopf, H. Schmidt-Böcking, R. E. Grisenti, and R. Dörner, Physical Review Letters **104**, 153401 (2010).

[90] X. M. Tong and C. D. Lin, Journal of Physics B: Atomic, Molecular and Optical Physics **38**, 2593 (2005).

[91] R. A. Aziz and M. J. Slaman, The Journal of Chemical Physics **94**, 8047 (1991).

[92] W. Cencek and K. Szalewicz, International Journal of Quantum Chemistry **108**, 2191 (2008).

[93] L. S. Davtyan, G. S. Pogosyan, A. N. Sisakyan, and V. M. Ter-Antonyan, Theoretical and Mathematical Physics **74**, 157 (1988).

[94] X. L. Yang, S. H. Guo, F. T. Chan, K. W. Wong, and W. Y. Ching, Physical Review A **43**, 1186 (1991).

[95] T. Jahnke, A. Czasch, M. Schöffler, S. Schössler, M. Käsz, J. Titze, K. Kreidi, R. E. Grisenti, A. Staudte, O. Jagutzki, L. P. H. Schmidt, S. K. Semenov, N. A. Cherepkov, H. Schmidt-Böcking, and R. Dörner, Journal of Physics B: Atomic, Molecular and Optical Physics **40**, 2597 (2007).

[96] L. S. Cederbaum, F. Tarantelli, A. Sgamellotti, and J. Schirmer, The Journal of Chemical Physics **85**, 6513 (1986).

[97] P. Lablanquie, T. P. Grozdanov, M. Žitnik, S. Carniato, P. Selles, L. Andric, J. Palaudoux, F. Penent, H. Iwayama, E. Shigemasa, Y. Hikosaka, K. Soejima, M. Nakano, I. H. Suzuki, and K. Ito, Physical Review Letters **107**, 193004 (2011).

[98] H. Ni, S. Chen, C. Ruiz, and A. Becker, Journal of Physics B: Atomic, Molecular and Optical Physics **44**, 175601 (2011).

[99] F. Maulbetsch and J. S. Briggs, Journal of Physics B: Atomic, Molecular and Optical Physics **28**, 551 (1995).

[100] M. Walter and J. S. Briggs, Physical Review Letters **85**, 1630 (2000).

[101] A. W. Malcherek and J. S. Briggs, Journal of Physics B: Atomic, Molecular and Optical Physics **30**, 4419 (1997).

[102] M. G. Makris, P. Lambropoulos, and A. Mihelič, Physical Review Letters **102**, 033002 (2009).

[103] A. Becker and F. H. M. Faisal, Physical Review A **50**, 3256 (1994).

[104] A. Becker and F. H. M. Faisal, Physical Review A **51**, 3390 (1995).

[105] F. H. M. Faisal, Journal of Physics B: Atomic and Molecular Physics **6**, L89 (1973).

[106] H. R. Reiss, Physical Review A **22**, 1786 (1980).

[107] A. Becker and F. H. M. Faisal, Journal of Physics B: Atomic, Molecular and Optical Physics **38**, R1 (2005).

[108] P. Agostini, F. Fabre, G. Mainfray, G. Petite, and N. K. Rahman, Physical Review Letters **42**, 1127 (1979).

[109] J. H. Eberly, J. Javanainen, and K. Rzażewski, Physics Reports **204**, 331 (1991).

[110] D. B. Milošević, G. G. Paulus, D. Bauer, and W. Becker, Journal of Physics B: Atomic, Molecular and Optical Physics **39**, R203 (2006).

[111] J. S. Parker, B. J. S. Doherty, K. T. Taylor, K. D. Schultz, C. I. Blaga, and L. F. DiMauro, Physical Review Letters **96**, 133001 (2006).

[112] H. Bachau, Physical Review A **83**, 033403 (2011).

[113] A. Palacios, D. A. Horner, T. N. Rescigno, and C. W. McCurdy, Journal of Physics B: Atomic, Molecular and Optical Physics **43**, 194003 (2010).

[114] L. Tao, C. W. McCurdy, and T. N. Rescigno, Physical Review A **82**, 023423 (2010).

[115] R. Nepstad, T. Birkeland, and M. Førre, Physical Review A **81**, 063402 (2010).

[116] D. A. Horner, T. N. Rescigno, and C. W. McCurdy, Physical Review A **81**, 023410 (2010).

[117] A. Rudenko, L. Foucar, M. Kurka, T. Ergler, K. U. Kühnel, Y. H. Jiang, A. Voitkiv, B. Najjari, A. Kheifets, S. Lüdemann, T. Havermeier, M. Smolarski, S. Schössler, K. Cole, M. Schöffler, R. Dörner, S. Düsterer, W. Li, B. Keitel, R. Treusch, M. Gensch, C. D. Schröter, R. Moshammer, and J. Ullrich, Physical Review Letters **101**, 073003 (2008).

[118] R. Moshammer, Y. H. Jiang, L. Foucar, A. Rudenko, T. Ergler, C. D. Schröter, S. Lüdemann, K. Zrost, D. Fischer, J. Titze, T. Jahnke, M. Schöffler, T. Weber, R. Dörner, T. J. M. Zouros, A. Dorn, T. Ferger, K. U. Kühnel, S. Düsterer, R. Treusch, P. Radcliffe, E. Plönjes, and J. Ullrich, Physical Review Letters **98**, 203001 (2007).

[119] S. X. Hu, J. Colgan, and L. A. Collins, Journal of Physics B: Atomic, Molecular and Optical Physics **38**, L35 (2005).

[120] M. Schultze, M. Fiess, N. Karpowicz, J. Gagnon, M. Korbman, M. Hofstetter, S. Neppl, A. L. Cavalieri, Y. Komninos, T. Mercouris, C. A. Nicolaides, R. Pazourek, S. Nagele, J. Feist, J. Burgdorfer, A. M. Azzeer, R. Ernstorfer, R. Kienberger, U. Kleineberg, E. Goulielmakis, F. Krausz, and V. S. Yakovlev, Science **328**, 1658 (2010).

[121] A. S. Kheifets and I. A. Ivanov, Physical Review Letters **105**, 233002 (2010).

[122] I. A. Ivanov, Physical Review A **83**, 023421 (2011).

[123] I. A. Ivanov, Physical Review A **86**, 023419 (2012).

[124] C.-H. Zhang and U. Thumm, Physical Review A **82**, 043405 (2010).

[125] C.-H. Zhang and U. Thumm, Physical Review A **84**, 033401 (2011).

[126] J. C. Baggesen and L. B. Madsen, Physical Review Letters **104**, 043602 (2010).

[127] M. D. Śpiewanowski and L. B. Madsen, Physical Review A **86**, 045401 (2012).

[128] S. Nagele, R. Pazourek, J. Feist, K. Doblhoff-Dier, C. Lemell, K. Tőkési, and J. Burgdörfer, Journal of Physics B: Atomic, Molecular and Optical Physics **44**, 081001 (2011).

[129] S. Nagele, R. Pazourek, J. Feist, and J. Burgdörfer, Physical Review A **85**, 033401 (2012).

[130] R. Pazourek, J. Feist, S. Nagele, and J. Burgdörfer, Physical Review Letters **108**, 163001 (2012).

[131] R. Pazourek, S. Nagele, and J. Burgdörfer, Faraday Discussions **163**, 353 (2013).

[132] M. Ivanov and O. Smirnova, Physical Review Letters **107**, 213605 (2011).

[133] L. R. Moore, M. A. Lysaght, J. S. Parker, H. W. van der Hart, and K. T. Taylor, Physical Review A **84**, 061404 (2011).

[134] J. M. Dahlström, A. L'Huillier, and A. Maquet, Journal of Physics B: Atomic, Molecular and Optical Physics **45**, 183001 (2012).

[135] J. M. Dahlström, D. Guénot, K. Klünder, M. Gisselbrecht, J. Mauritsson, A. L'Huillier, A. Maquet, and R. Taïeb, Chemical Physics **414**, 53 (2013).

[136] J. Su, H. Ni, A. Becker, and A. Jaroń-Becker, Physical Review A **87**, 033420 (2013).

[137] J. Su, H. Ni, A. Becker, and A. Jaroń-Becker, Journal of Modern Optics **60**, 1484 (2013).

[138] J. Su, H. Ni, A. Becker, and A. Jaroń-Becker, Physical Review A **88**, 023413 (2013).

[139] J. Su, H. Ni, A. Becker, and A. Jaroń-Becker, Chinese Journal of Physics **52**, 404 (2014).

[140] J. Su, H. Ni, A. Becker, and A. Jaroń-Becker, Physical Review A **89**, 013404 (2014).

[141] E. P. Wigner, Physical Review **98**, 145 (1955).

[142] F. T. Smith, Physical Review **118**, 349 (1960).

[143] J. Su, H. Ni, A. Jaroń-Becker, and A. Becker, *Time delays in two-photon ionization*, *submitted* (2014).

[144] A. Emmanouilidou, A. Staudte, and P. B. Corkum, New Journal of Physics **12**, 103024 (2010).

[145] C. Ruiz and A. Becker, New Journal of Physics **10**, 025020 (2008).

[146] A. S. Kheifets, I. A. Ivanov, and I. Bray, Journal of Physics B: Atomic, Molecular and Optical Physics **44**, 101003 (2011).

[147] C. Ruiz and A. Becker, *unpublished* .

[148] K. Kreidi, D. Akoury, T. Jahnke, T. Weber, A. Staudte, M. Schöffler, N. Neumann, J. Titze, L. P. H. Schmidt, A. Czasch, O. Jagutzki, R. A. Costa Fraga, R. E. Grisenti, M. Smolarski, P. Ranitovic, C. L. Cocke, T. Osipov, H. Adaniya, J. C. Thompson, M. H. Prior, A. Belkacem, A. L. Landers, H. Schmidt-Böcking, and R. Dörner, Physical Review Letters **100**, 133005 (2008).

[149] M. S. Schöffler, K. Kreidi, D. Akoury, T. Jahnke, A. Staudte, N. Neumann, J. Titze, L. P. H. Schmidt, A. Czasch, O. Jagutzki, R. A. Costa Fraga, R. E. Grisenti, M. Smolarski, P. Ranitovic, C. L. Cocke, T. Osipov, H. Adaniya, S. Lee, J. C. Thompson, M. H. Prior, A. Belkacem, T. Weber, A. Landers, H. Schmidt-Böcking, and R. Dörner, Physical Review A **78**, 013414 (2008).

[150] K. Kreidi, D. Akoury, T. Jahnke, T. Weber, A. Staudte, M. Schöffler, N. Neumann, J. Titze, L. P. H. Schmidt, A. Czasch, O. Jagutzki, R. A. C. Fraga, R. E. Grisenti, R. D. Muiño, N. A. Cherepkov, S. K. Semenov, P. Ranitovic, C. L. Cocke, T. Osipov, H. Adaniya, J. C. Thompson, M. H. Prior, A. Belkacem, A. Landers, H. Schmidt-Böcking, and R. Dörner, The European Physical Journal Special Topics **169**, 109 (2009)